

ARMY RESEARCH LABORATORY



**Numerical Investigation of Aerodynamics of
Canard-Controlled Missile Using Planar and Grid Tail Fins,
Part I: Supersonic Flow**

**by James DeSpirito, Milton E. Vaughn, Jr.,
and W. David Washington**

ARL-TR-2848

September 2002

Approved for public release; distribution is unlimited.

20021126 078

NOTICES

Disclaimers

The findings in this report are not to be construed as an official Department of the Army position unless so designated by other authorized documents.

Citation of manufacturer's or trade names does not constitute an official endorsement or approval of the use thereof.

DESTRUCTION NOTICE—For classified documents, follow the procedures in DOD 5200.22-M, Industrial Security Manual, Section II-19 or DOD 5200.1-R, Information Security Program Regulation, Chapter IX. For unclassified, limited documents, destroy by any method that will prevent disclosure of contents or reconstruction of the document.

Army Research Laboratory

Aberdeen Proving Ground, MD 21005-5066

ARL-TR-2848

September 2002

Numerical Investigation of Aerodynamics of Canard-Controlled Missile Using Planar and Grid Tail Fins, Part I: Supersonic Flow

**James DeSpirito
Weapons and Materials Research Directorate, ARL**

**Milton E. Vaughn, Jr. and W. David Washington
U.S. Army Aviation and Missile Command**

Acknowledgments

The authors thank Richard Angelini, U.S. Army Research Laboratory (ARL), for providing scientific visualizations of the flowfields, and Eric Fournier, Defence Research and Development Canada–Valcartier, for providing discussions on the wind tunnel data. This work was supported in part by a grant of high-performance computing time from the U.S. Department of Defense High Performance Computing Modernization program at the ARL Major Shared Resource Center, Aberdeen Proving Ground, MD.

Contents

Acknowledgments	i
List of Figures	iv
List of Tables	viii
1. Introduction	1
2. Computational Approach	1
2.1 Geometry and Simulation Parameters.....	1
2.2 Solver.....	4
2.3 Computational Mesh and Boundary Conditions	5
2.4 Solution Methodology.....	5
3. Results and Discussion	8
3.1 Aerodynamic Coefficients – CFD Validation.....	8
3.2 Flowfield Visualizations.....	13
3.3 Control Surface Forces.....	21
4. Summary and Conclusions	24
5. References	27
Appendix A. Aerodynamic Coefficients for Planar Fin Case	29
Appendix B. Aerodynamic Coefficients for Grid Fin Case	37
Appendix C. Force Coefficients on Canards	45
Appendix D. Force Coefficients on Planar Fins	53
Appendix E. Force Coefficients on Grid Fins	61
Appendix F. Components of Aerodynamic Coefficients	69

List of Abbreviations and Symbols **79**

Report Documentation Page **80**

List of Figures

Figure 1. Generic canard-controlled missile with planar fins.....	2
Figure 2. Generic canard-controlled missile with grid fins.	3
Figure 3. (a) Missile nose with canards at $\delta = 0^\circ$ and (b) front view of missile.....	3
Figure 4. Views of computational mesh: (a) tail region of planar fin case and (b) ogive region.	6
Figure 5. Views of computational mesh: (a) tail region of grid fin case and (b) close-up of grid fin base.....	7
Figure 6. Normal force coefficient, planar fin case, (a) $M = 1.5$ and (b) $M = 3.0$	9
Figure 7. Pitching moment coefficient about nose, planar fin case, (a) $M = 1.5$ and (b) $M = 3.0$	10
Figure 8. Axial force coefficient, planar fin case, $M = 1.5$	11
Figure 9. Axial force coefficient, grid fin case, $M = 1.5$	11
Figure 10. Rolling moment coefficient for (a) planar fin and (b) grid fin cases.....	12
Figure 11. Side force coefficient for (a) planar fin and (b) grid fin cases.	14
Figure 12. Port (left image) and starboard (right image) views of C_p contours at $M = 1.5$ for planar fin case with $\delta = 10^\circ$ and (a, b) $\alpha = 4^\circ$ and (c, d) $\alpha = 10^\circ$	15
Figure 13. C_p contours on missile surface and axial plane behind canards for $\delta = 10^\circ$ and $\alpha = 0^\circ$, 4° , and 10° at (a–c) $M = 1.5$ and (d–f) $M = 3.0$	16
Figure 14. C_p contours on planar fins at $M = 1.5$ and at (a) $\alpha = 4^\circ$ and (b) $\alpha = 10^\circ$	17
Figure 15. C_p contours on grid fins at $M = 1.5$ and at (a) $\alpha = 4^\circ$ and (b) $\alpha = 10^\circ$	18
Figure 16. C_p contours (range: -0.1–0.3) on missile surfaces and vorticity magnitude contours (range: 0–50000) on axial cross-planes at 2, 4, 6, 8, 10, 12, 14, and 16 cal. for planar fin case with $\delta = 10^\circ$ at $M = 1.5$ and (a) $\alpha = 0^\circ$, (b) $\alpha = 4^\circ$, and (c) $\alpha = 10^\circ$	19
Figure 17. C_p contours (range: -0.1–0.3) on missile surfaces and vorticity magnitude contours (range: 0–50000) on axial cross-planes at 2, 4, 6, 8, 10, 12, 14, and 16 cal. for planar fin case with $\delta = 10^\circ$ at $M = 3.0$ and (a) $\alpha = 0^\circ$, (b) $\alpha = 4^\circ$, and (c) $\alpha = 10^\circ$	20
Figure 18. C_p contours (range: -0.1–0.3) on missile surfaces and vorticity magnitude contours (range: 0–50000) on axial cross-planes at 2, 4, 6, 8, 10, 12, 14, and 16 cal. for planar fin case with $\delta = 0^\circ$ at $M = 1.5$ and (a) $\alpha = 0^\circ$ and (b) $\alpha = 4^\circ$	21
Figure 19. C_p contours (range: -0.1–0.3) on missile surfaces and vorticity magnitude contours (range: 0–50000) on axial cross-planes at (a) 12, 14, and 16 cal. for the planar fin case and at (b) 12, 14, and 15 cal. for the grid fin case with $\delta = 10^\circ$ at $M = 1.5$ and $\alpha = 4^\circ$	22
Figure 20. Side force coefficient on tail fins for (a) planar fin and (b) grid fin case for $\delta = 10^\circ$ and $M = 1.5$	23

Figure 21. Normal force coefficient on tail fins for (a) planar fin and (b) grid fin case for $\delta = 10^\circ$ and $M = 1.5$	25
Figure 22. Normal force coefficient on tail fins for (a) planar fin and (b) grid fin case for $\delta = 10^\circ$ and $M = 3.0$	26
Figure A-1. Normal force for planar fin case at Mach 1.5.	29
Figure A-2. Normal force for planar fin case at Mach 3.0.	29
Figure A-3. Side force for planar fin case at Mach 1.5.....	30
Figure A-4. Side force for planar fin case at Mach 3.0.....	30
Figure A-5. Axial force for planar fin case at Mach 1.5.....	31
Figure A-6. Axial force for planar fin case at Mach 3.0.....	31
Figure A-7. Pitching moment about nose for planar fin case at Mach 1.5.	32
Figure A-8. Pitching moment about nose for planar fin case at Mach 3.0.	32
Figure A-9. Pitching moment about moment reference point (MRP) for planar fin case at Mach 1.5.	33
Figure A-10. Pitching moment about MRP for planar fin case at Mach 3.0.	33
Figure A-11. Rolling moment for planar fin case at Mach 1.5.....	34
Figure A-12. Rolling moment for planar fin case at Mach 3.0.....	34
Figure A-13. Yawing moment for planar fin case at Mach 1.5.	35
Figure A-14. Yawing moment for planar fin case at Mach 3.0.	35
Figure A-15. Center of pressure location from nose for planar fin case at Mach 1.5.	36
Figure A-16. Center of pressure location from nose for planar fin case at Mach 3.0.	36
Figure B-1. Normal force for grid fin case at Mach 1.5.	37
Figure B-2. Normal force for grid fin case at Mach 3.0.	37
Figure B-3. Side force for grid fin case at Mach 1.5.	38
Figure B-4. Side force for grid fin case at Mach 3.0.	38
Figure B-5. Axial force for grid fin case at Mach 1.5.....	39
Figure B-6. Axial force for grid fin case at Mach 3.0.....	39
Figure B-7. Pitching moment about nose for grid fin case at Mach 1.5.	40
Figure B-8. Pitching moment about nose for grid fin case at Mach 3.0.	40
Figure B-9. Pitching moment about moment reference point (MRP) for grid fin case at Mach 1.5.	41
Figure B-10. Pitching moment about MRP for grid fin case at Mach 3.0.	41
Figure B-11. Rolling moment for grid fin case at Mach 1.5.....	42
Figure B-12. Rolling moment for grid fin case at Mach 3.0.....	42
Figure B-13. Yawing moment for grid fin case at Mach 1.5.	43

Figure B-14. Yawing moment for grid fin case at Mach 3.0.....	43
Figure B-15. Center of pressure location from nose for grid fin case at Mach 1.5.....	44
Figure B-16. Center of pressure location from nose for grid fin case at Mach 3.0.....	44
Figure C-1. Canard normal force, $\delta = 0^\circ$, Mach 1.5.....	45
Figure C-2. Canard normal force, $\delta = 0^\circ$, Mach 3.0.....	45
Figure C-3. Canard normal force, $\delta = 10^\circ$, Mach 1.5.....	46
Figure C-4. Canard normal force, $\delta = 10^\circ$, Mach 3.0.....	46
Figure C-5. Canard side force, $\delta = 0^\circ$, Mach 1.5.....	47
Figure C-6. Canard side force, $\delta = 0^\circ$, Mach 3.0.....	47
Figure C-7. Canard side force, $\delta = 10^\circ$, Mach 1.5.....	48
Figure C-8. Canard side force, $\delta = 10^\circ$, Mach 3.0.....	48
Figure C-9. Canard axial force, $\delta = 0^\circ$, Mach 1.5.....	49
Figure C-10. Canard axial force, $\delta = 0^\circ$, Mach 3.0.....	49
Figure C-11. Canard axial force, $\delta = 10^\circ$, Mach 1.5.....	50
Figure C-12. Canard axial force, $\delta = 10^\circ$, Mach 3.0.....	50
Figure D-1. Planar fin normal force, $\delta = 0^\circ$, Mach 1.5.....	53
Figure D-2. Planar fin normal force, $\delta = 0^\circ$, Mach 3.0.....	53
Figure D-3. Planar fin normal force, $\delta = 10^\circ$, Mach 1.5.....	54
Figure D-4. Planar fin normal force, $\delta = 10^\circ$, Mach 3.0.....	54
Figure D-5. Planar fin side force, $\delta = 0^\circ$, Mach 1.5.....	55
Figure D-6. Planar fin side force, $\delta = 0^\circ$, Mach 3.0.....	55
Figure D-7. Planar fin side force, $\delta = 10^\circ$, Mach 1.5.....	56
Figure D-8. Planar fin side force, $\delta = 10^\circ$, Mach 3.0.....	56
Figure D-9. Planar fin axial force, $\delta = 0^\circ$, Mach 1.5.....	57
Figure D-10. Planar fin axial force, $\delta = 0^\circ$, Mach 3.0.....	57
Figure D-11. Planar fin axial force, $\delta = 10^\circ$, Mach 1.5.....	58
Figure D-12. Planar fin axial force, $\delta = 10^\circ$, Mach 3.0.....	58
Figure E-1. Grid fin normal force, $\delta = 0^\circ$, Mach 1.5.....	61
Figure E-2. Grid fin normal force, $\delta = 0^\circ$, Mach 3.0.....	61
Figure E-3. Grid fin normal force, $\delta = 10^\circ$, Mach 1.5.....	62
Figure E-4. Grid fin normal force, $\delta = 10^\circ$, Mach 3.0.....	62
Figure E-5. Grid fin side force, $\delta = 0^\circ$, Mach 1.5.....	63
Figure E-6. Grid fin side force, $\delta = 0^\circ$, Mach 3.0.....	63
Figure E-7. Grid fin side force, $\delta = 10^\circ$, Mach 1.5.....	64

Figure E-8. Grid fin side force, $\delta = 10^\circ$, Mach 3.0	64
Figure E-9. Grid fin axial force, $\delta = 0^\circ$, Mach 1.5.....	65
Figure E-10. Grid fin axial force, $\delta = 0^\circ$, Mach 3.0.....	65
Figure E-11. Grid fin axial force, $\delta = 10^\circ$, Mach 1.5.....	66
Figure E-12. Grid fin axial force, $\delta = 10^\circ$, Mach 3.0.....	66
Figure F-1. Components of normal force for planar fin case, $\delta = 10^\circ$, Mach 1.5.	69
Figure F-2. Components of normal force for planar fin case, $\delta = 10^\circ$, Mach 3.0.	69
Figure F-3. Components of normal force for grid fin case, $\delta = 10^\circ$, Mach 1.5.	70
Figure F-4. Components of normal force for grid fin case, $\delta = 10^\circ$, Mach 3.0.	70
Figure F-5. Components of side force for planar fin case, $\delta = 10^\circ$, Mach 1.5.	71
Figure F-6. Components of side force for planar fin case, $\delta = 10^\circ$, Mach 3.0.	71
Figure F-7. Components of side force for grid fin case, $\delta = 10^\circ$, Mach 1.5.	72
Figure F-8. Components of side force for grid fin case, $\delta = 10^\circ$, Mach 3.0.	72
Figure F-9. Components of axial force for planar fin case, $\delta = 10^\circ$, Mach 1.5.	73
Figure F-10. Components of axial force for planar fin case, $\delta = 10^\circ$, Mach 3.0.	73
Figure F-11. Components of axial force for grid fin case, $\delta = 10^\circ$, Mach 1.5.	74
Figure F-12. Components of axial force for grid fin case, $\delta = 10^\circ$, Mach 3.0.....	74

List of Tables

Table 1. Canard and fin characteristics.....	3
Table C-1. Aerodynamic coefficients on canards, planar fin case, $\delta = 0^\circ$, Mach 1.5.	51
Table C-2. Aerodynamic coefficients on canards, planar fin case, $\delta = 10^\circ$, Mach 1.5.	51
Table C-3. Aerodynamic coefficients on canards, planar fin case, $\delta = 0^\circ$, Mach 3.0.	52
Table C-4. Aerodynamic coefficients on canards, planar fin case, $\delta = 10^\circ$, Mach 3.0.	52
Table D-1. Aerodynamic coefficients on planar fins, $\delta = 0^\circ$, Mach 1.5.....	59
Table D-2. Aerodynamic coefficients on planar fins, $\delta = 10^\circ$, Mach 1.5.....	59
Table D-3. Aerodynamic coefficients on planar fins, $\delta = 0^\circ$, Mach 3.0.....	60
Table D-4. Aerodynamic coefficients on planar fins, $\delta = 10^\circ$, Mach 3.0.....	60
Table E-1. Aerodynamic coefficients on grid fins, $\delta = 0^\circ$, Mach 1.5.....	67
Table E-2. Aerodynamic coefficients on grid fins, $\delta = 10^\circ$, Mach 1.5.....	67
Table E-3. Aerodynamic coefficients on grid fins, $\delta = 0^\circ$, Mach 3.0.....	68
Table E-4. Aerodynamic coefficients on grid fins, $\delta = 10^\circ$, Mach 3.0.....	68
Table F-1. Components of aerodynamic coefficients, planar fin case, $\delta = 0^\circ$, Mach 1.5.....	75
Table F-2. Components of aerodynamic coefficients, planar fin case, $\delta = 10^\circ$, Mach 1.5.....	75
Table F-3. Components of aerodynamic coefficients, planar fin case, $\delta = 0^\circ$, Mach 3.0.....	76
Table F-4. Components of aerodynamic coefficients, planar fin case, $\delta = 10^\circ$, Mach 3.0.....	76
Table F-5. Components of aerodynamic coefficients, grid fin case, $\delta = 0^\circ$, Mach 1.5.	77
Table F-6. Components of aerodynamic coefficients, grid fin case, $\delta = 10^\circ$, Mach 1.5.	77
Table F-7. Components of aerodynamic coefficients, grid fin case, $\delta = 0^\circ$, Mach 3.0.	78
Table F-8. Components of aerodynamic coefficients, grid fin case, $\delta = 10^\circ$, Mach 3.0.	78

1. Introduction

Missile concepts with forward control fins, or canards, have been used for many years. However, previous studies have shown that concepts with canards can suffer from adverse induced rolling moments [1–4]. The use of grid fins, or “lattice controls,” for the tail control surfaces instead of conventional planar fins was recently proposed as a possible remedy for the roll control problems [5].

A grid fin, shown in section 2, is an unconventional lifting and control surface that consists of an outer frame supporting an inner grid of intersecting planar surfaces of small chord. The aerodynamics of grid fins has been investigated since 1985 by the U.S. Army Aviation and Missile Command (AMCOM), Redstone Arsenal, AL [6–8]. Studies have shown that when compared to conventional planar fins, grid fins have advantages such as effective aerodynamic control at high α and high Mach number, a small hinge moment, compact storage, improved yaw stability, attenuated body-vortex interference, and improved roll control of canard-controlled munitions [5–7, 9]. The primary disadvantage of the grid fin concept is a higher drag than conventional planar fins, which can be minimized with the proper design [8]. Computational fluid dynamic (CFD) techniques to calculate the viscous flow around grid fins were recently demonstrated [10, 11].

In this study, the CFD techniques demonstrated previously [10, 11] were applied to study the roll control effectiveness of both planar and grid fins on a generic canard-controlled missile shape. The numerical calculations were validated with wind tunnel data from an experimental study from AMCOM and the former Defence Research Establishment Valcartier (DREV), now the Defence Research and Development Canada–Valcartier (DRDC–V) [5]. The objectives of the CFD study were to provide insight into the fluid dynamic phenomena that cause roll reversal on canard-controlled missiles with planar tail fins and permit the retention of roll control when grid tail fins are used on canard-controlled missiles. The CFD simulations provide visualizations of the flowfield that aid the understanding of the flow physics responsible for the adverse forces and moments observed in the wind tunnel and calculated results.

2. Computational Approach

2.1 Geometry and Simulation Parameters

The investigation used CFD to determine the flowfield and aerodynamic coefficients on a 16-cal., four-finned, generic canard-controlled missile. This study followed the experimental wind tunnel investigation performed at DREV [5]. The DREV wind tunnel is an intermittent, in-draft wind tunnel with a $0.6 \times 0.6\text{-m}$ test section. In this type of tunnel, the air flows from an

atmospheric pressure tank to a vacuum tank, and the Reynolds number is lower than free-flight values at high Mach numbers. The wind tunnel Reynolds number ranges from about $1.56 \times 10^7 \text{ m}^{-1}$ at $M = 1.15$ to $4.7 \times 10^6 \text{ m}^{-1}$ at $M = 4.0$.

The wind tunnel model geometry was used in the CFD study. Four canards on the ogive were in line with the fins. Two fin types were investigated: conventional planar fins and grid fins. Figure 1 and Figure 2 show the geometry for the planar fin and grid fin cases, respectively. The missile was 16 cal. long with a hemispherical nose on a 3.7-cal. truncated tangent ogive. The canard midchord was located 0.96 cal. from the missile nose, and the fin midchord was located 1.5 cal. from the missile base. The canards (Figure 3a) had a double-wedge, trapezoidal planform with a span of 0.37 cal., a root chord of 0.36 cal., a tip chord of 0.13 cal., a midchord root thickness of 0.03 cal., and a taper ratio of 1.48. The planar fins had a double-wedge, rectangular planform with a span of 0.78 cal., a chord of 0.65 cal., and a midchord thickness of 0.03 cal. The grid fin structure (Figure 3b) consisted of 23 cubic and 12 prismatic cells with a span of 0.74 cal., a chord of 0.10 cal., and a thickness of 0.46 cal. The web thickness between the grid fin cells was 0.003 cal. The canard and fin characteristics are summarized in Table 1.

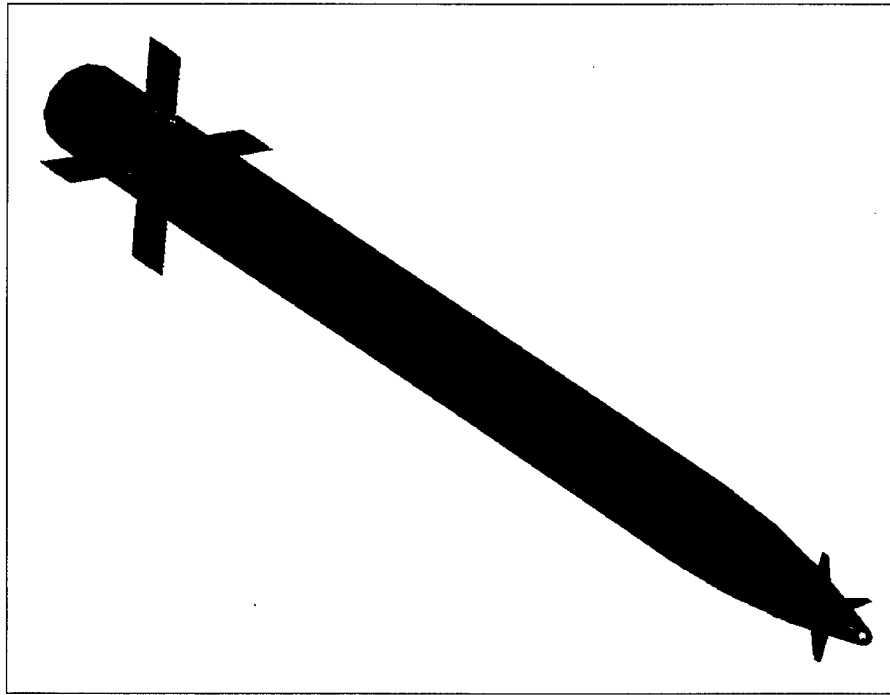


Figure 1. Generic canard-controlled missile with planar fins.

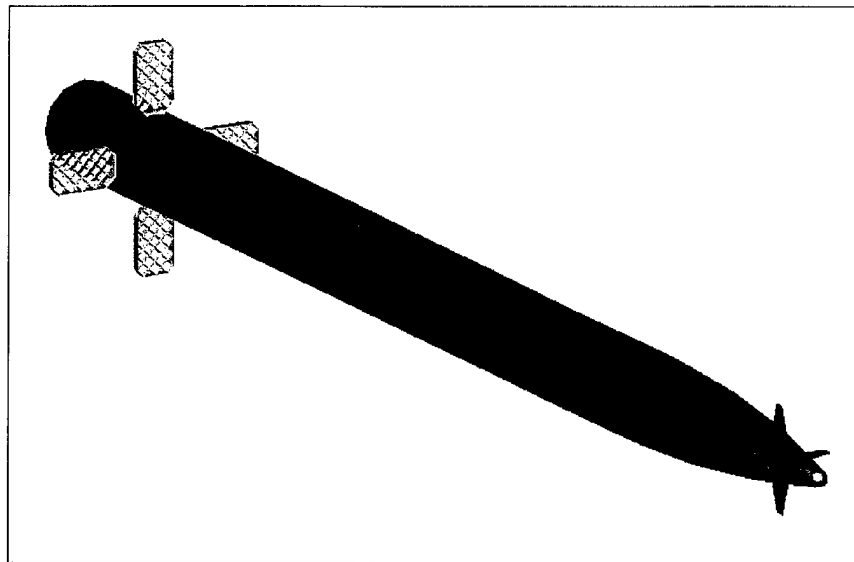


Figure 2. Generic canard-controlled missile with grid fins.

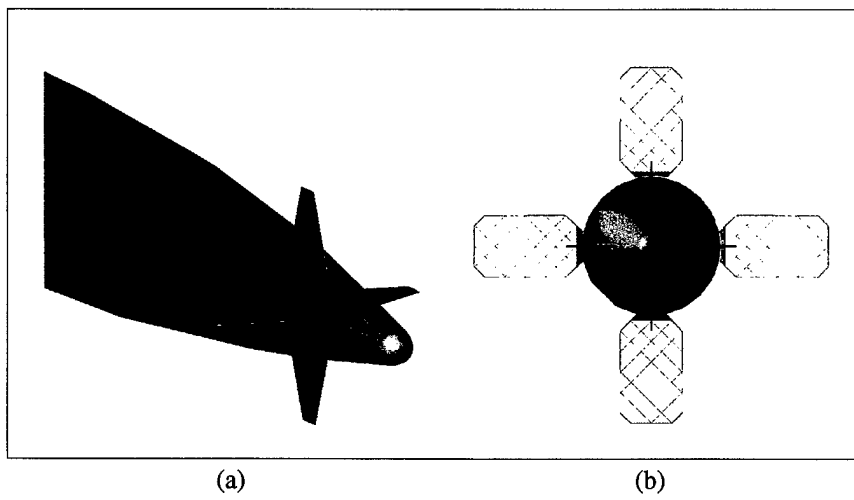


Figure 3. (a) Missile nose with canards at $\delta = 0^\circ$ and (b) front view of missile.

Table 1. Canard and fin characteristics.

Control Type	Span (cal.)	Root Chord (cal.)	Tip Chord (cal.)	Root Thickness (cal.)	Taper Ratio	Web (cal.)
Canard	0.37	0.36	0.13	0.03	1.48	—
Planar fin	0.78	0.65	0.65	0.03	1.0	—
Grid fin	0.74	0.10	0.10	0.46	1.0	0.003

The analyses were performed at two Mach numbers: $M = 1.5$ and 3.0 ; two canard deflections: $\delta = 0^\circ$ and 10° ; and six angles of attack: $\alpha = 0^\circ, 2^\circ, 4^\circ, 6^\circ, 8^\circ$, and 10° . The DREV wind tunnel conditions were used in this study. For $M = 1.5$, the freestream conditions were a Reynolds

number of $1.4 \times 10^7 \text{ m}^{-1}$, a static temperature of 206 K, and a static pressure of $2.6 \times 10^4 \text{ Pa}$. For $M = 3$, the freestream Reynolds number was $7.6 \times 10^6 \text{ m}^{-1}$, the static temperature was 107 K, and the static pressure was $2.77 \times 10^3 \text{ Pa}$. The model reference diameter was 30 mm, and the moment reference point was 10.63 cal. aft of the missile nose. The simulations were performed with the missile in the cruciform (+) configuration. The DREV wind tunnel data ranged from $-4^\circ < \alpha < +15^\circ$. In the $\delta = 10^\circ$ case, all four canards were deflected in the same direction, intended to give a positive roll, which, by convention, was clockwise when viewed from the rear of the missile.

2.2 Solver

Steady-state calculations were used to compute the flowfield using the commercial CFD code, FLUENT version 5.5 [12]. The implicit, compressible, unstructured-mesh solver was used. The three-dimensional (3-D), time-dependent, Reynolds-Averaged Navier-Stokes (RANS) equations are solved using the finite volume method:

$$\frac{\partial}{\partial \nu} \int_{\nu} \mathbf{W} dV + \oint [\mathbf{F} - \mathbf{G}] \cdot dA = \int_{\nu} \mathbf{H} dV, \quad (1)$$

where

$$\mathbf{W} = \begin{Bmatrix} \rho \\ \rho u \\ \rho v \\ \rho w \\ \rho E \end{Bmatrix}, \quad \mathbf{F} = \begin{Bmatrix} \rho v \\ \rho vu + pi \\ \rho vv + pj \\ \rho vw + pk \\ \rho vE + pv \end{Bmatrix}, \quad \mathbf{G} = \begin{Bmatrix} 0 \\ \tau_{xi} \\ \tau_{yi} \\ \tau_{zi} \\ \tau_{ij}v_j + q \end{Bmatrix}. \quad (2)$$

The inviscid flux vector \mathbf{F} is evaluated by a standard upwind flux-difference splitting. In the implicit solver, each equation in the coupled set of governing equations is linearized implicitly with respect to all dependent variables in the set, resulting in a block system of equations. A block Gauss-Seidel, point implicit linear equation solver is used with an algebraic multigrid method to solve the resultant block system of equations. The coupled set of governing equations is discretized in time and time marching proceeds until a steady-state solution is reached. In the implicit scheme, which was used in this study, an Euler implicit discretization in time is combined with a Newton-type linearization of the fluxes.

A modified form of the $k-\epsilon$ two-equation turbulence model was used in this study. Called the “realizable” $k-\epsilon$ model in FLUENT, it differs from the standard $k-\epsilon$ model in that it contains a new formulation for the turbulent viscosity and a new transport equation for the dissipation rate, which was derived from an exact equation for the transport of the mean-square vorticity fluctuation [12]. The term “realizable” means that the model satisfies certain mathematical constraints on the Reynolds stresses consistent with turbulent flow physics. The realizable $k-\epsilon$ model has shown substantial improvements over the standard $k-\epsilon$ model where flow features include strong streamline curvature, vortices, and rotation [12].

2.3 Computational Mesh and Boundary Conditions

The geometry and unstructured mesh were generated using the preprocessor, GAMBIT, supplied in the FLUENT software suite. Canard deflection and angle of attack precluded the use of symmetry or periodicity, so a full 3-D mesh was required. In generating the meshes, boundary layer mesh spacing was used near the missile body and fin surfaces. The two-layer zonal model was used for the near-wall equations and the first point off the surface (cell center) was about 7.0×10^{-5} cal. from the surface, chosen to give a y^+ value of about 1.0. All mesh stretching was kept at or below 1.25. About 144 cells were used on the missile body in the circumferential direction, with this value increased in the grid fin region.

An all-hexahedral (hex) mesh was used for the planar fin case, with the total number of cells about 4.9 M. O-grid type meshes were generated around the canards and planar fins. Figure 4a and Figure 4b show the surface mesh in the tail region and ogive region, respectively. A hybrid hex and tetrahedral (tet) mesh was used for the grid fin case, with the total number of cells about 15.7 M. The first 13 cal. of the missile was meshed with the same hex mesh as in the planar fin case. A tet mesh was used in the tail region (Figure 5a) in order to mesh the complicated grid fin structure. Layers of triangular prisms were used on the body to capture the boundary layer (Figure 5b). The tet mesh in the tail is matched to the forward hex mesh via a layer of pyramidal cells. Due to meshing constraints, prism layers were not used around the grid fins, so the spacing of the first point off the grid fin surfaces was larger than optimum. Postprocessing of the runs showed that the y^+ values on the missile body, canards, and planar fins were less than 1.0. The y^+ value on the grid fins ranged from about 2–15, with most of the grid fin surface near the higher value. Although these values are not optimum for calculating the boundary layer properties on the grid fins, there was little apparent effect on the missile aerodynamic coefficients.

The base flow was not simulated in these calculations, so the mesh ended at the base of the missile. For supersonic flow, this has been found to be reasonable methodology if any tail fin surfaces are not located too close to the base of the missile. The computational domain extended about 4 cal. from the missile body. An outflow boundary condition was used downstream, a pressure inflow (with freestream conditions) boundary condition was used upstream, and a far-field pressure (nonreflecting) boundary condition was used for the outer boundary. A no-slip wall boundary condition was used for all solid surfaces.

2.4 Solution Methodology

The simulations were performed in parallel on Silicon Graphics, Inc. (SGI) Origin 2000 and 3800 machines. The simulations were run with a maximum Courant-Friedrich-Lowy (CFL) number of 10 for the planar fin cases and 5 for the grid fin cases. Each case was started with a lower CFL value (usually about 1.0) and ramped up to the maximum during the first few hundred iterations of the simulation. The calculations took ~300–600 μ s/cell/iteration, using 28 processors for the planar case and 64 or 96 processors for the grid fin case. Convergence was determined by tracking the change in the flow residuals and the aerodynamic

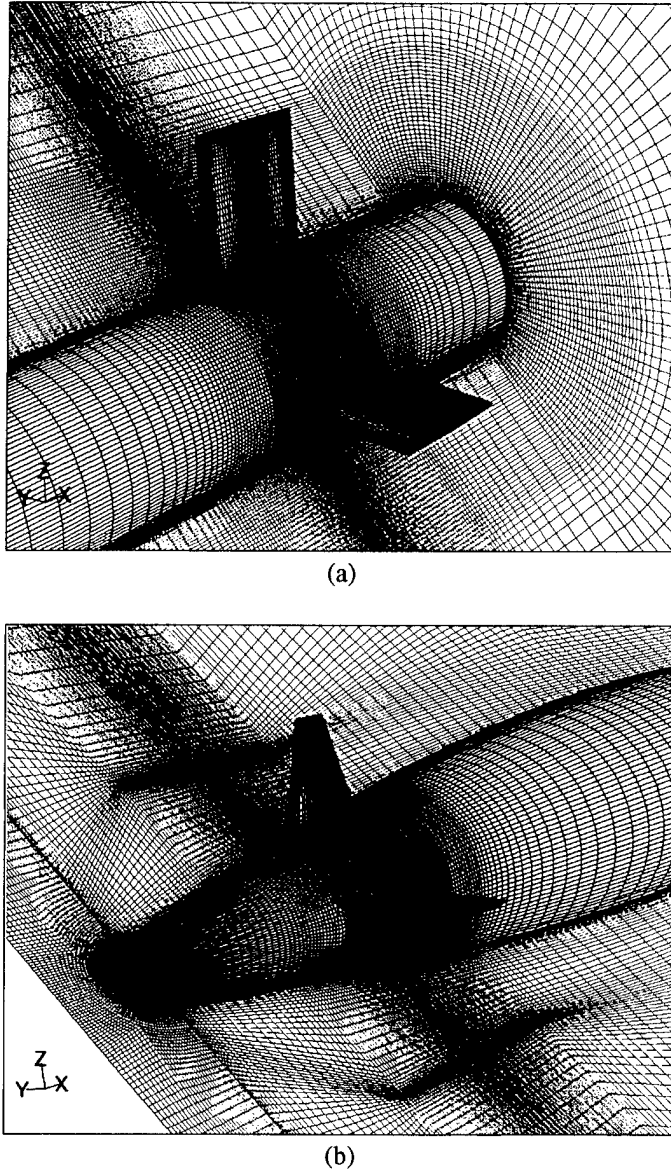


Figure 4. Views of computational mesh: (a) tail region of planar fin case and (b) ogive region.

coefficients during the solution. The solution was deemed converged when the flow residuals had stabilized and the aerodynamic coefficients were changing less than 0.5% after the last 100 iterations. The aerodynamic coefficients converged in about 1000–1500 iterations.

The planar fin cases were run with the double precision solver. To reduce the computer memory required, the grid fin cases were run with the single precision solver. A planar fin case ($\alpha = 4^\circ$, $\delta = 10^\circ$) was repeated with the single precision solver to determine if there was an effect on the calculated solution. The six aerodynamic coefficients calculated with the single precision solver were within 0.5% of those calculated with the double precision solver. Four of the coefficients were within 0.1%. Therefore, the single precision solver was adequate for these computations.

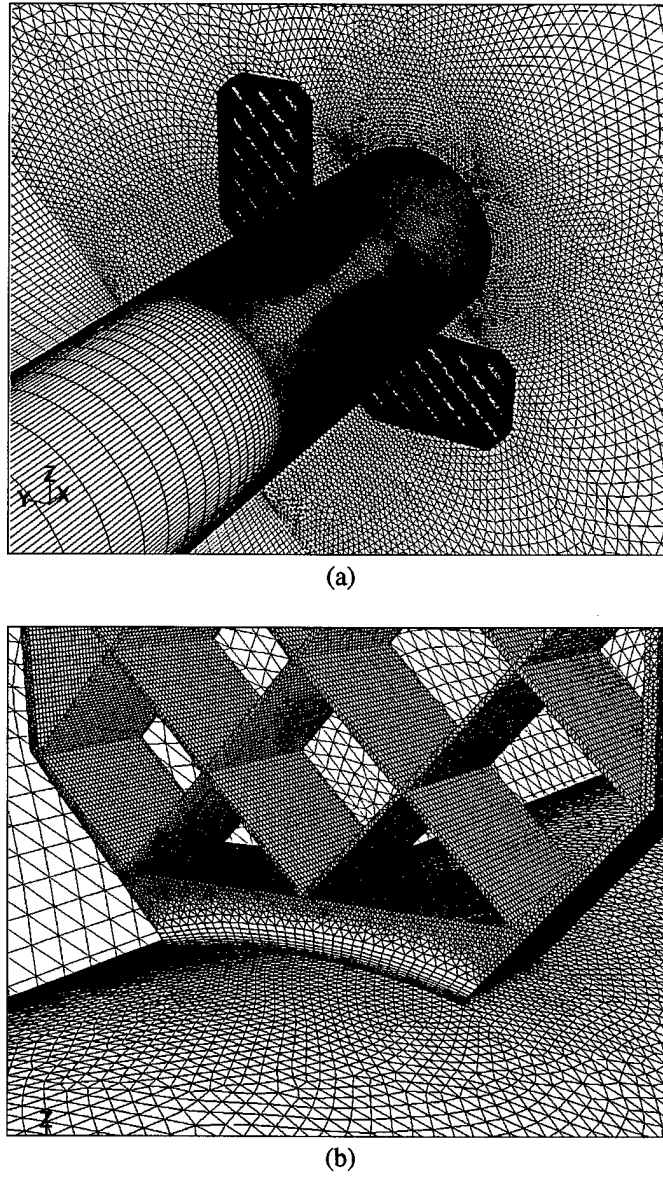


Figure 5. Views of computational mesh: (a) tail region of grid fin case and (b) close-up of grid fin base.

Mesh adaption was used to determine mesh independence. The meshes for two planar fin cases ($\alpha = 4^\circ$ and 10° ; both at $\delta = 10^\circ$) were adapted on the static pressure gradient using the adaption tools in the FLUENT software. After adaption, the solutions were again run until convergence was achieved. The maximum change in the aerodynamic coefficients was 0.9% for the $\alpha = 4^\circ$ case, with four of the six coefficients changing less than 0.5%. The coefficients changed less than 0.2% after mesh adaption in the $\alpha = 10^\circ$ case. These results show that the original mesh used for the planar fin case had high enough resolution for a mesh independent solution. For the grid fin case, the mesh on the first 13 cal. is the same as the planar fin case, so it is also adequate. In the tail region, the small cell sizes required for the grid fin surfaces resulted in a volume mesh that should have had more than adequate resolution, so no mesh adaption was performed.

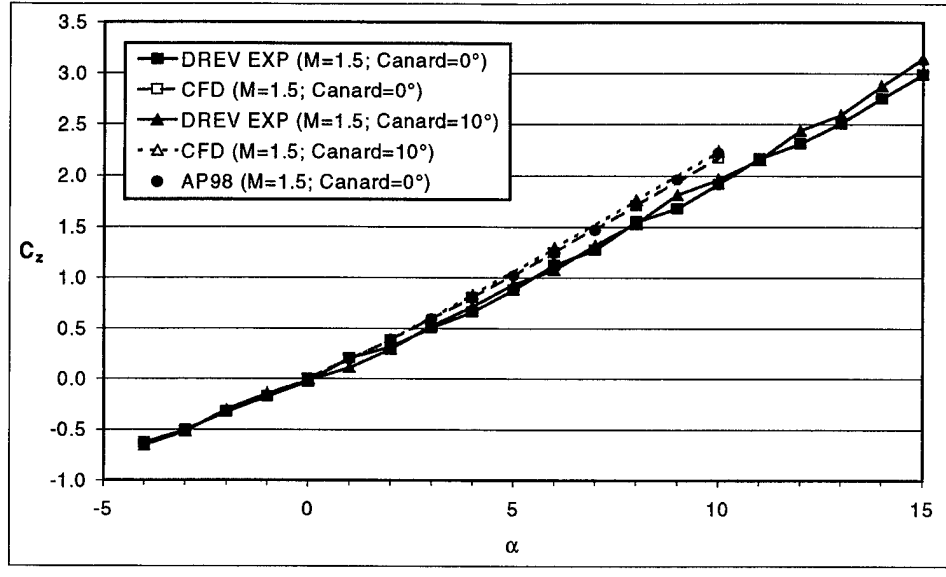
3. Results and Discussion

3.1 Aerodynamic Coefficients – CFD Validation

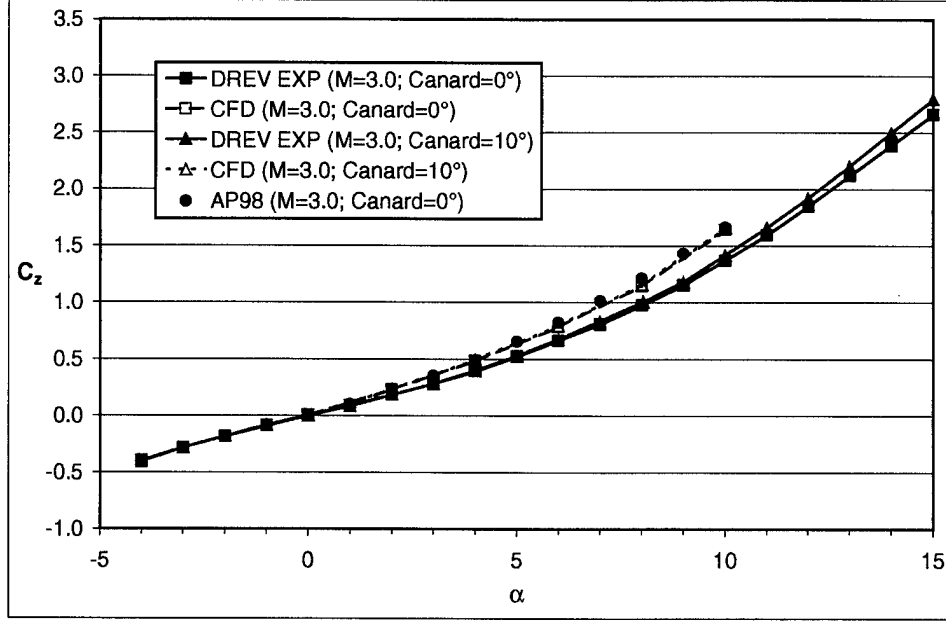
The viscous and pressure forces from the computed flowfields were integrated along the missile body, canard, and fin surfaces to calculate the aerodynamic coefficients. The axial force, normal force, side force, rolling moment, pitching moment, and yawing moment are presented in missile-based coordinates. This is a right-handed system with the x -axis coinciding with the missile axis and oriented to the rear, the y -axis oriented to the missile's starboard side, and the z -axis oriented upward. The forces are positive when coinciding with the positive coordinate axes. By convention, the moments are defined as follows: the rolling moment is positive when the roll is clockwise when looking forward from the aft end of the missile, the yawing moment is positive when the nose is moving right, and the pitching moment is positive when the nose is moving upward. The reference area is the cross-sectional area of the missile base, and the reference length is the diameter of the missile. The calculated coefficients are compared to wind-tunnel measurements performed at DREV [5]. Since the base flow was not calculated, only the “forebody” axial force is compared to the data. The forebody axial force from the experimental data was obtained by correcting the measured total axial force for the base drag component using measured pressures at the base of the wind tunnel model. Not including the base flow in the simulations can result in error of a few percent in the computed forebody axial force, while using localized base pressure measurements to obtain the experimental forebody axial force can also lead to errors of a few percent [10].

All the computed aerodynamic coefficients showed very good agreement with experimental values from the DREV wind tunnel (Appendices A and B). The computed and measured normal force and pitching moment coefficients are compared in Figure 6 and Figure 7, respectively, for the $M = 1.5$ and $M = 3.0$ planar fin cases. Also shown in Figures 6 and 7 are the predictions from the AP98 aeroprediction code [13]. AP98 is an engineering code based on empirical and theoretical methods. The comparison of the CFD and AP98 predictions is excellent. The difference between the predicted and measured values increases with α . In general, the slope of the linear portion of the curve is steeper in the predicted case. However, the predicted trend is the same as the measured trend, including the increased curvature at the higher Mach number. Similar results were obtained for the grid fin cases, which are presented in Appendix B.

The computed and measured axial force coefficients are compared in Figure 8 and Figure 9 for the $M = 1.5$ planar and grid fin cases, respectively. Again the CFD and AP98 predictions compare very well. The difference between the predicted and measured C_x values ranged from about 7.5%–15%. The forebody C_x for the grid fin case is about 1.7 times that observed in the planar fin case at $M = 1.5$. Note that the drag of the grid fins on this model is larger than that which could be achieved in an “optimum” design. First, the grid fin frame is not chamfered,



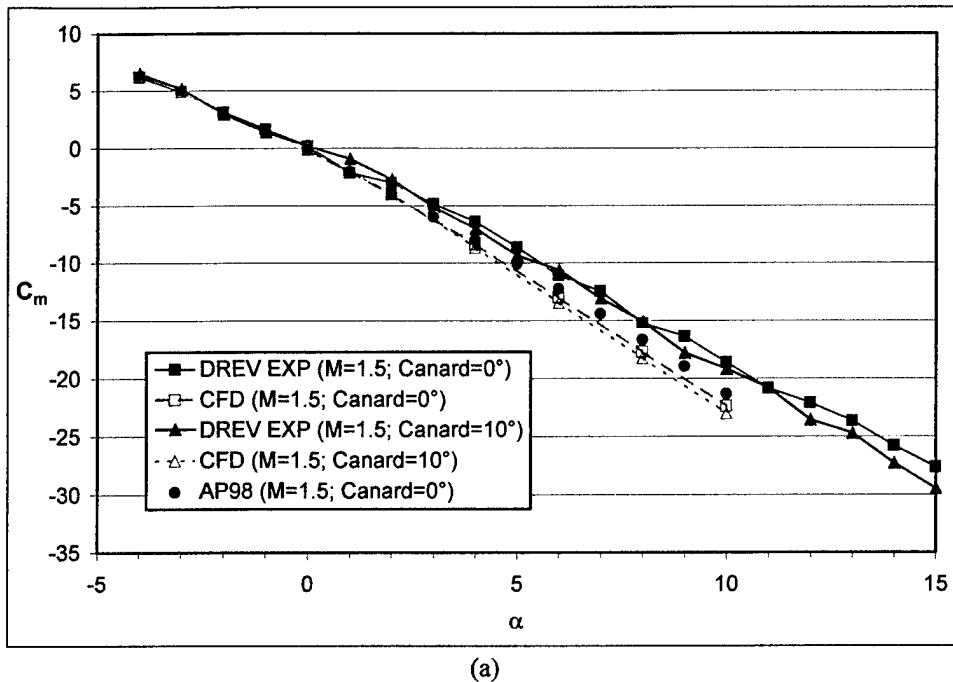
(a)



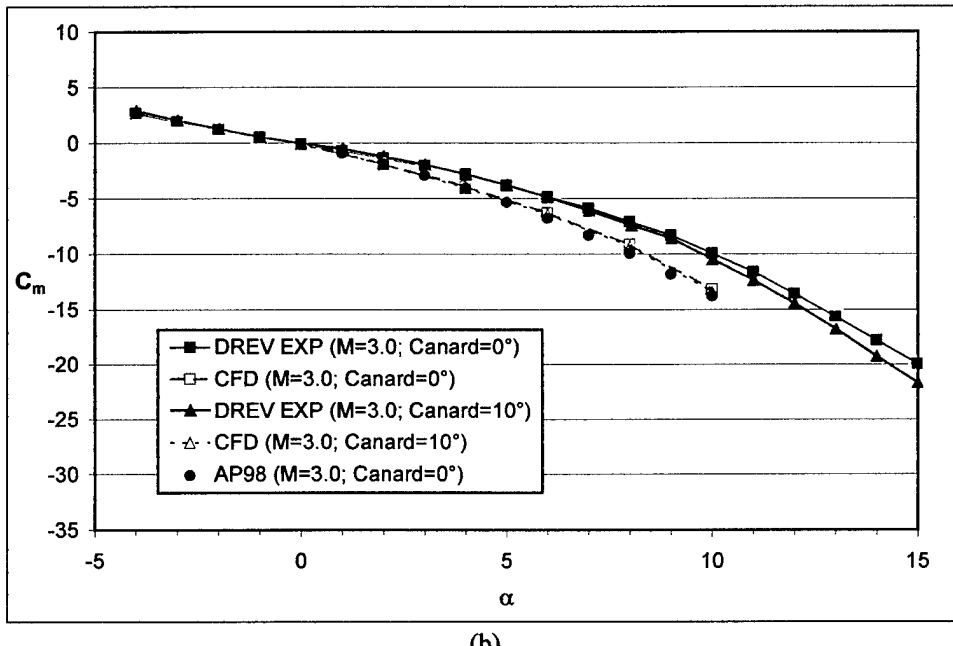
(b)

Figure 6. Normal force coefficient, planar fin case, (a) $M = 1.5$ and (b) $M = 3.0$.

which has been shown to dramatically reduce the fin drag [8]. Second, because of the small size of the wind tunnel model, the web thickness could not be scaled down to the proper design thickness due to machining limitations, and it is about 1.5 times larger than optimum. The fin drag was previously shown to be directly related to the thickness of the webs and the number of webs present [14]. Earlier studies [9, 10], with an optimum web thickness and chamfered grid fin frame, showed an increase in forebody C_x for a missile with grid fins of only 1.4 times that of a missile with planar fins.



(a)



(b)

Figure 7. Pitching moment coefficient about nose, planar fin case, (a) $M = 1.5$ and (b) $M = 3.0$.

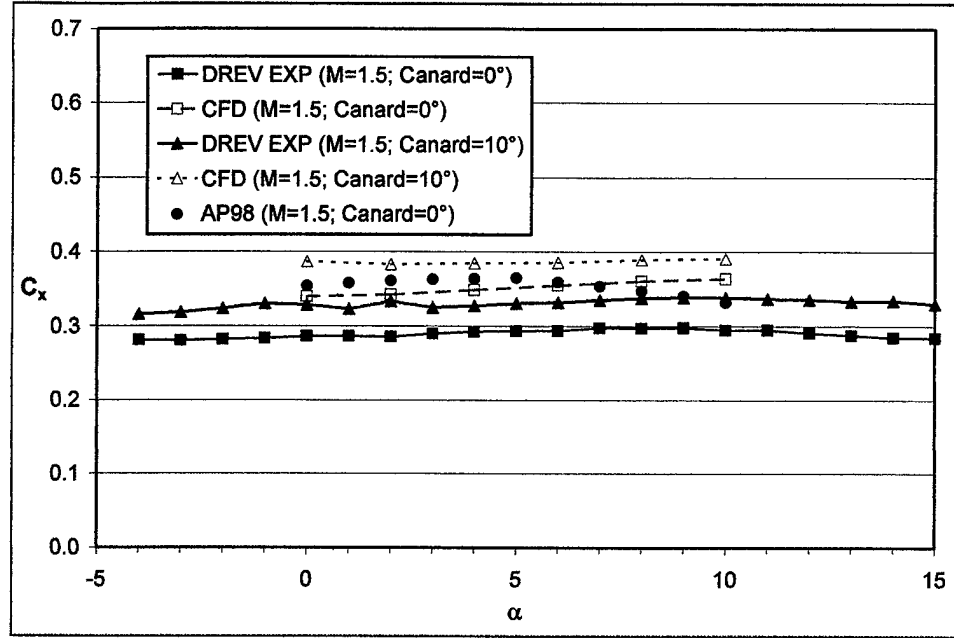


Figure 8. Axial force coefficient, planar fin case, $M = 1.5$.

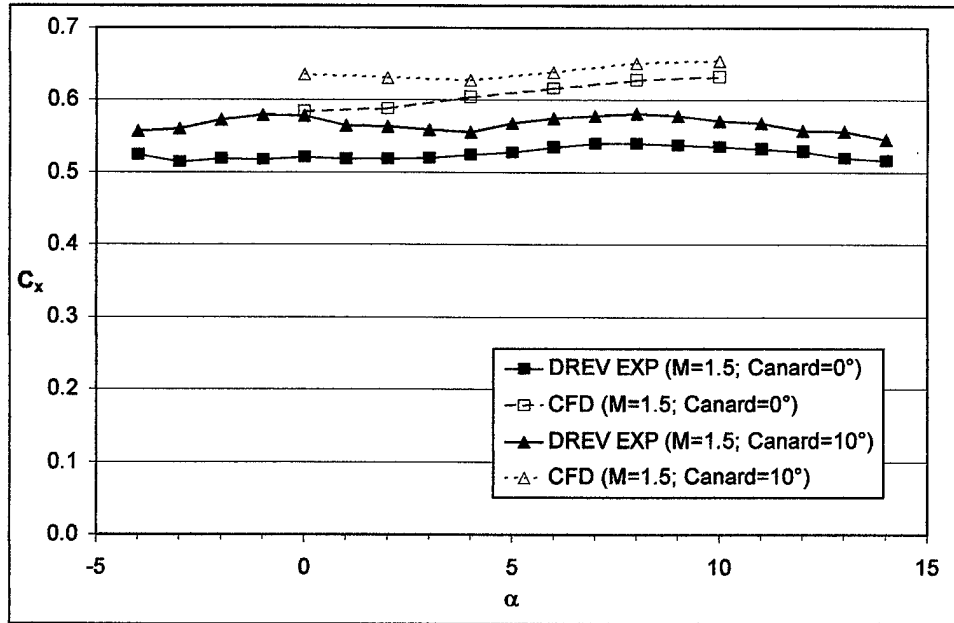
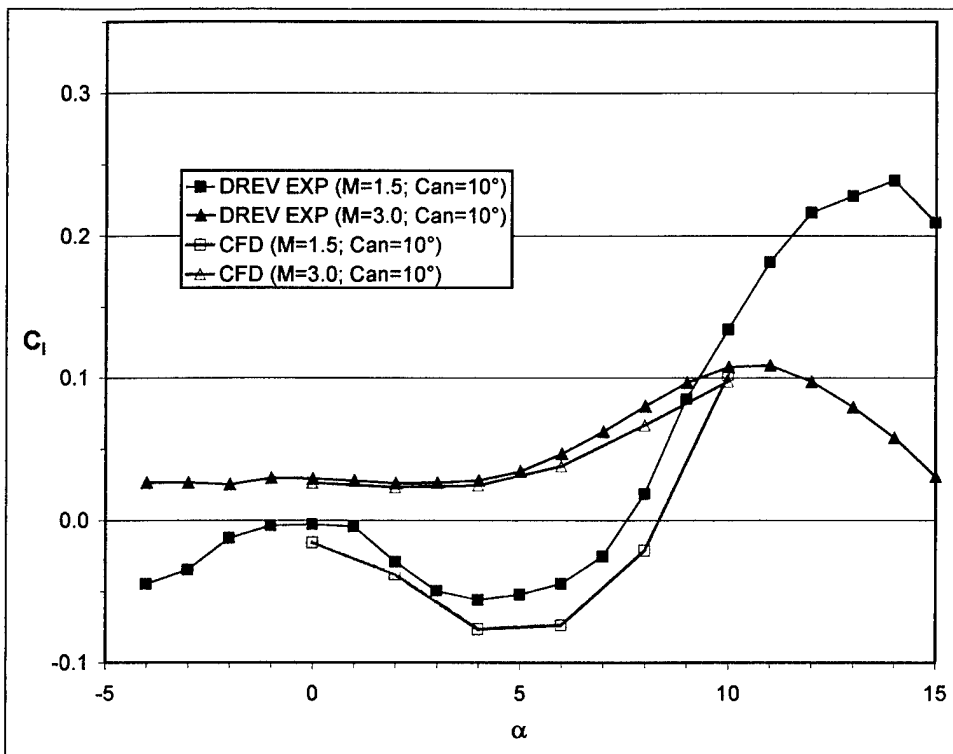
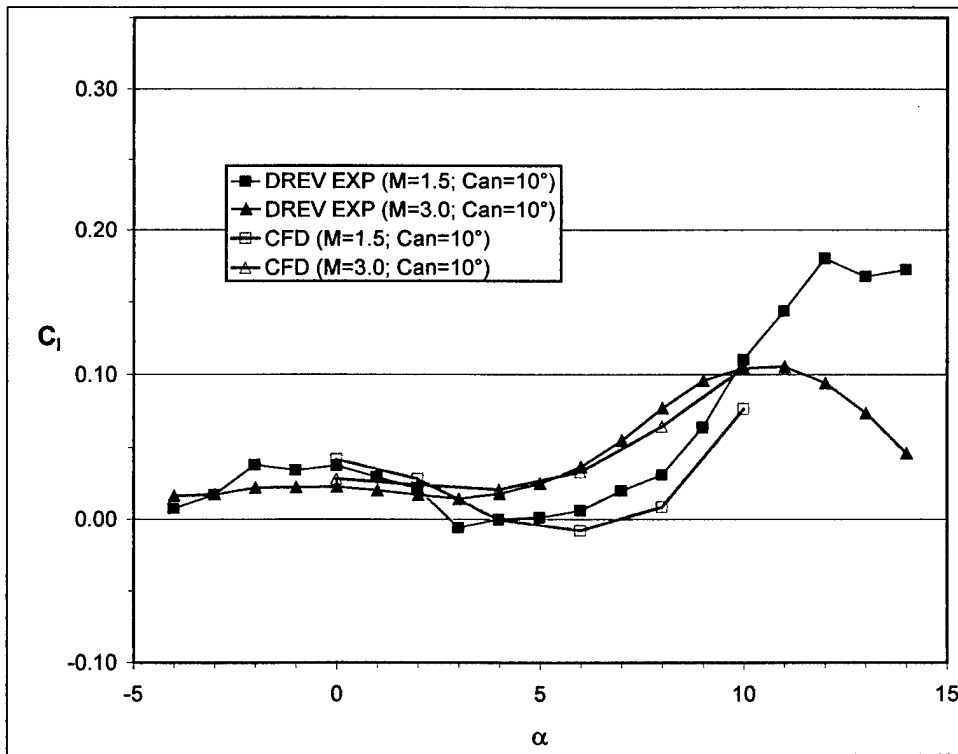


Figure 9. Axial force coefficient, grid fin case, $M = 1.5$.

An important objective of this study was to accurately predict the adverse induced rolling moment and side force observed in the wind tunnel experiments. Validation of these components gives confidence to the flow visualizations obtained from the CFD. As shown in Figure 10, very good agreement between the computed and experimental values of C_l was obtained. Figure 10 shows the comparison of the computed and measured C_l for the planar and



(a)



(b)

Figure 10. Rolling moment coefficient for (a) planar fin and (b) grid fin cases.

grid fin cases at both Mach numbers and $\delta = 10^\circ$. The experimental C_l had a large amount of bias. This bias was removed for the $\delta = 10^\circ$ case shown in Figure 10, using a method that DREV uses, which was as follows. The C_l for the $\delta = 0^\circ$ case, which should be zero at all α , is subtracted from the C_l for the $\delta = 10^\circ$ case. This assumes that the bias is constant between test runs. A small difference between the computed and experimental C_l remains; however, note that the absolute magnitude of the C_l is small (<0.1), so the agreement is still quite good. The CFD accurately captured the adverse roll phenomenon. The agreement in the shape of the curve, including reversal of the roll direction in the $M = 1.5$ planar fin case (Figure 10a), is excellent. Also note that the direction of roll in the $M = 1.5$ planar fin case is opposite that which should be induced by the deflected canards until α is above 8° . This effect, which appears to be due to the canard trailing vortices interacting with the planar fins, will be discussed further when the flowfield is presented. For the $M = 1.5$ grid fin case (Figure 10b), C_l is positive at $\alpha = 0^\circ$, decreasing to near zero between $4^\circ < \alpha < 7^\circ$ (some loss of roll control). At $M = 3.0$, C_l is always positive and is similar for both fin types.

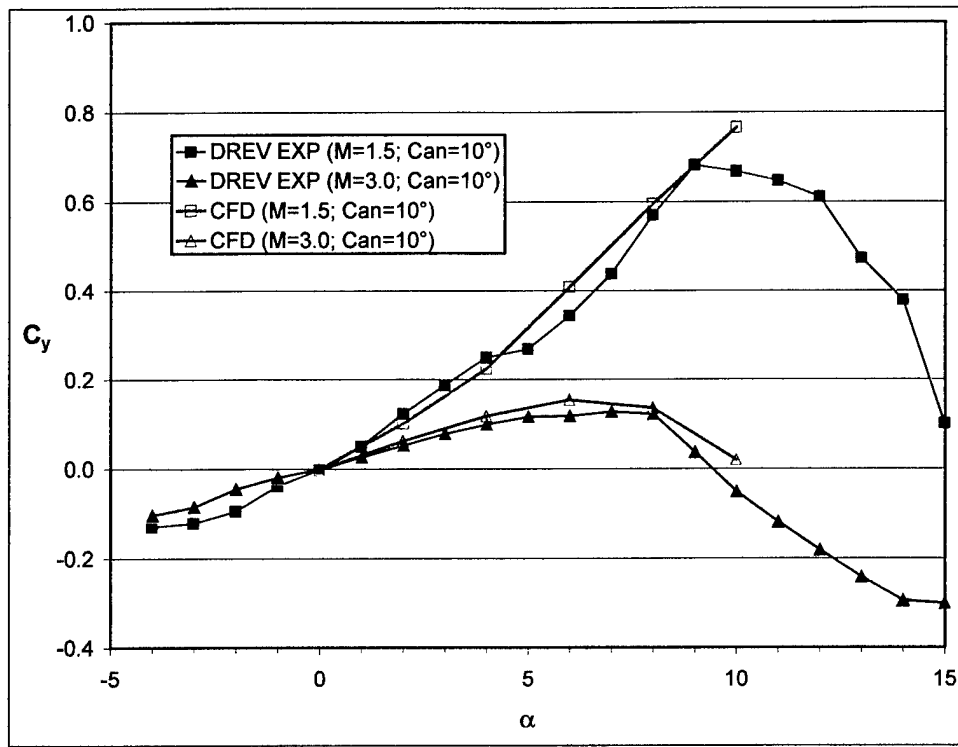
The CFD also accurately predicted the nonlinear induced side force characteristics observed in the canard deflected cases. Figure 11 shows the comparison of the computed and measured C_y for the planar and grid fin cases at both Mach numbers and $\delta = 10^\circ$. The flow is symmetric about the vertical plane for the $\delta = 0^\circ$ cases, so $C_y = 0$ and is not shown. There was little difference in C_y due to fin type at either Mach number. At $M = 3.0$, the maximum C_y was not too large. However, at $M = 1.5$, C_y was about 5 times larger than at $M = 3.0$. The calculations accurately predicted the change in slope of the C_y vs. α curve at $M = 3.0$ for both fin types. The predictions do not predict maximum C_y as well at $M = 1.5$. The simulations end near the maximum value but it appears that the beginning of the change in slope is correctly predicted in the grid fin case (Figure 11b).

The comparisons of the yawing moment were similar to the side force and are shown in Appendices A and B, where all coefficients for both fin types are presented.

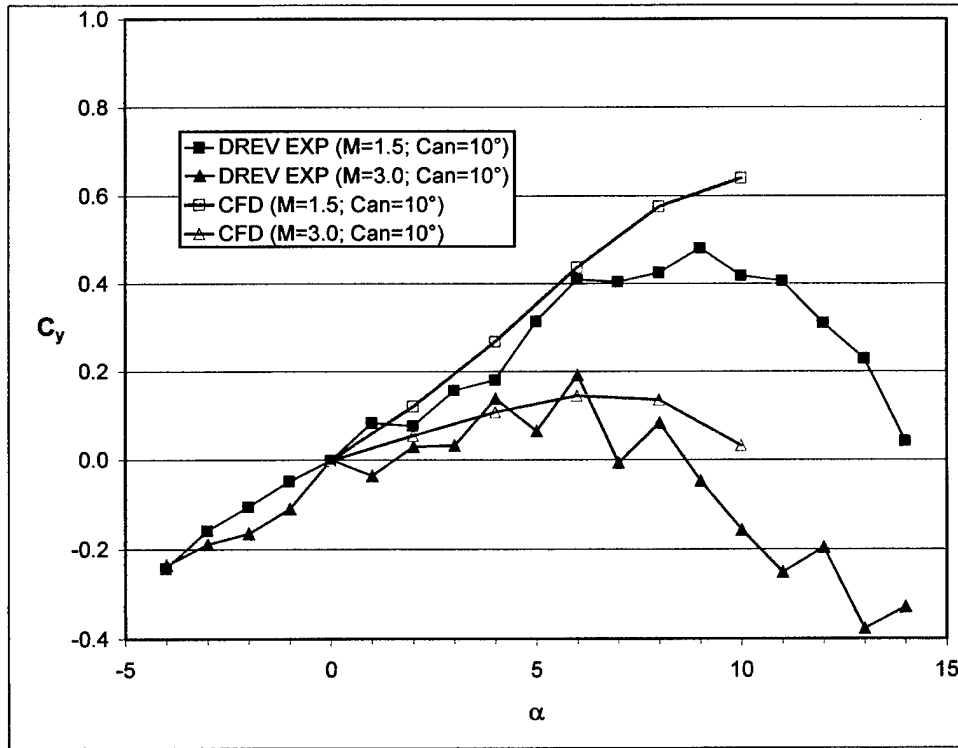
These results show that the CFD has accurately predicted the aerodynamic coefficients for a generic canard-controlled missile with both conventional planar fins and grid fins in supersonic flow. With the CFD results validated, the computed flowfield can now be used to investigate the physics responsible for roll-reversal or loss of roll control.

3.2 Flowfield Visualizations

Visualizations of the flowfield showed that the canard deflection had a strong effect on the forces on the missile body. Figure 12 shows the C_p distribution on the missile surfaces for the planar fin cases with $\delta = 10^\circ$ at $\alpha = 4^\circ$ and 10° . The $\delta = 0^\circ$ cases are not presented, but they showed a periodic C_p distribution on the missile with no contribution to C_y , C_b or C_r . For the $\delta = 10^\circ$ cases, the canard wake and trailing vortices interacted with the missile flowfield to change the pressure distribution both along the missile body and on the tail fins. The effect is most



(a)



(b)

Figure 11. Side force coefficient for (a) planar fin and (b) grid fin cases.

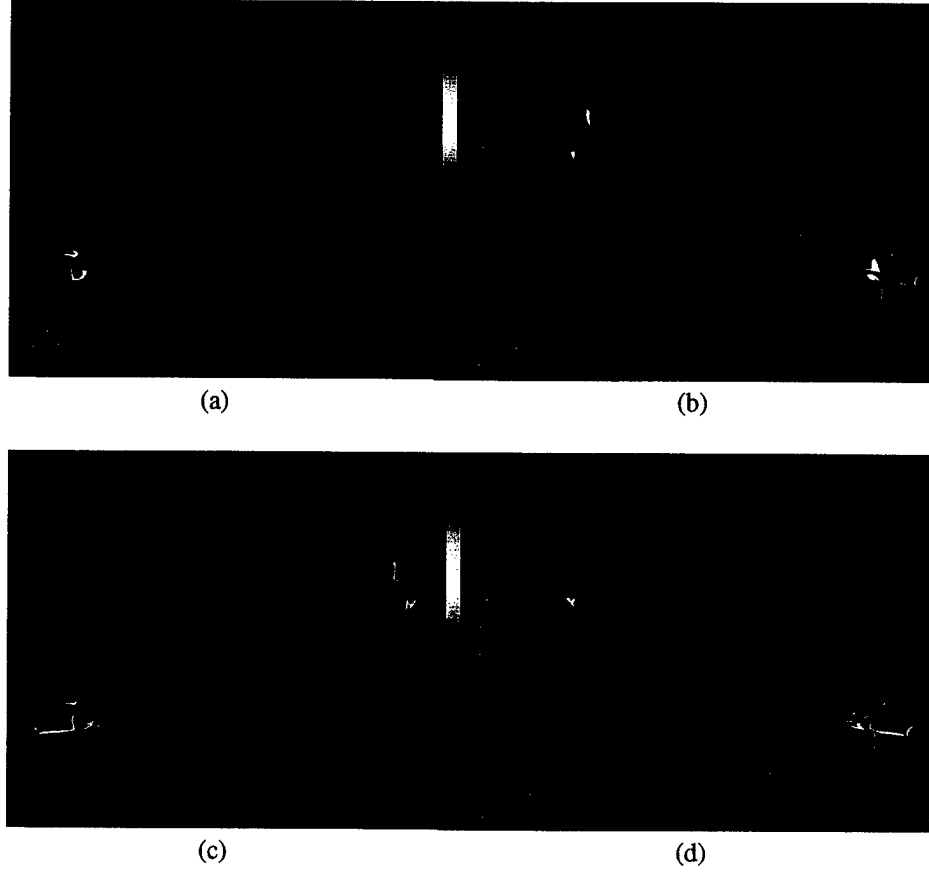


Figure 12. Port (left image) and starboard (right image) views of C_p contours at $M = 1.5$ for planar fin case with $\delta = 10^\circ$ and (a, b) $\alpha = 4^\circ$ and (c, d) $\alpha = 10^\circ$.

pronounced at $M = 1.5$, where a large low-pressure region is observed on the starboard side of the missile (Figure 12d). Although the effect was still present at $M = 3.0$, the effect was not as great, which correlates with the measured C_y .

The large side force at $M = 1.5$ and high α appears to be caused by the interaction of the wake flow from the deflected canards with the crossflow separation on the leeward side of the missile. This is best observed by viewing visualizations of the pressure distribution on an axial cut-plane being swept along the missile axis. The plots in Figure 13 are images from such a visualization and also illustrate the effect. As the angle of attack of the missile increases, the effective angle of attack of the starboard canard decreases while that of the port canard increases. The wake from the port canard appears to be primarily responsible for inducing a clockwise (viewed from rear of missile) flow around the missile behind the canards that both shifts the azimuthal location and increases the size of the low-pressure region that is due to the crossflow around the missile. The leeward canard also appears to contribute to this effect. The low-pressure wake behind both the port and leeward canards increase as α increases (Figure 13a–c).

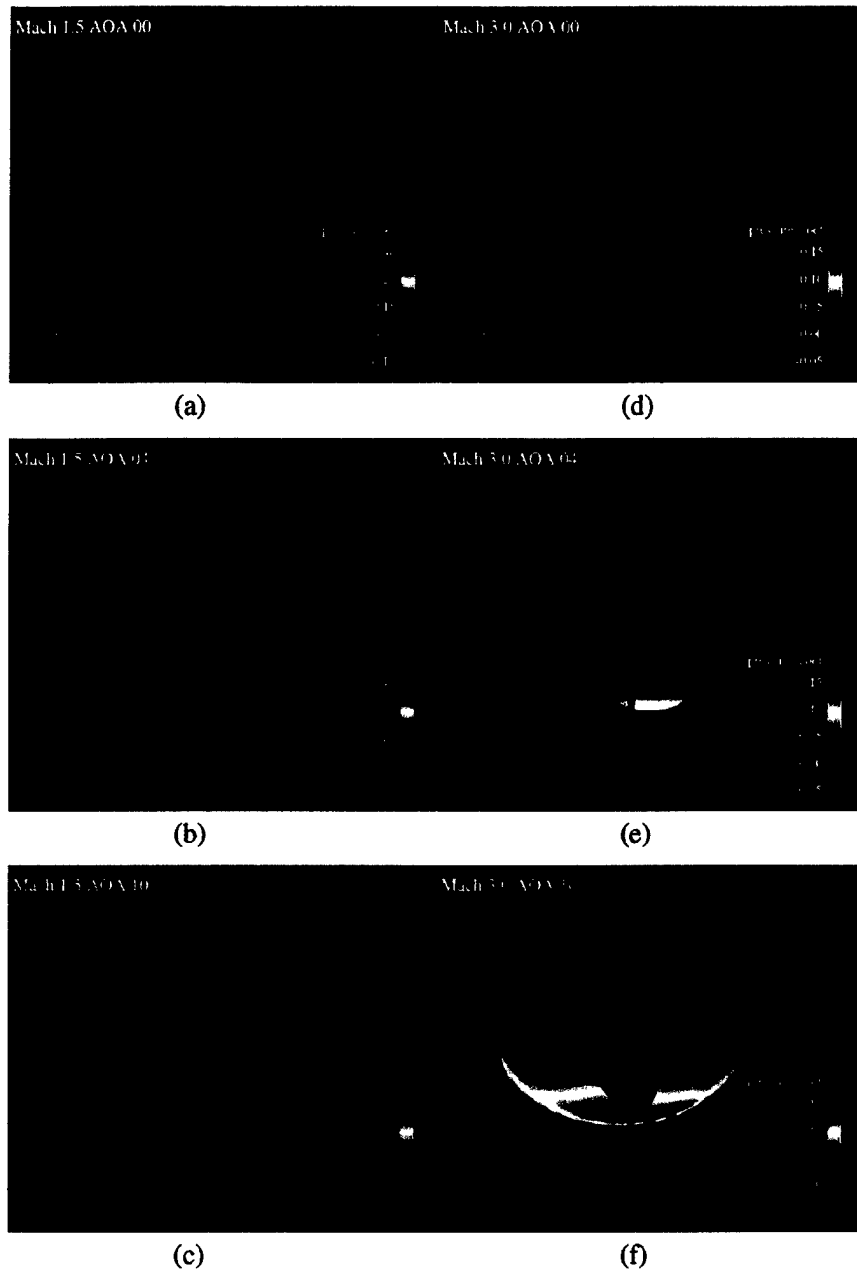
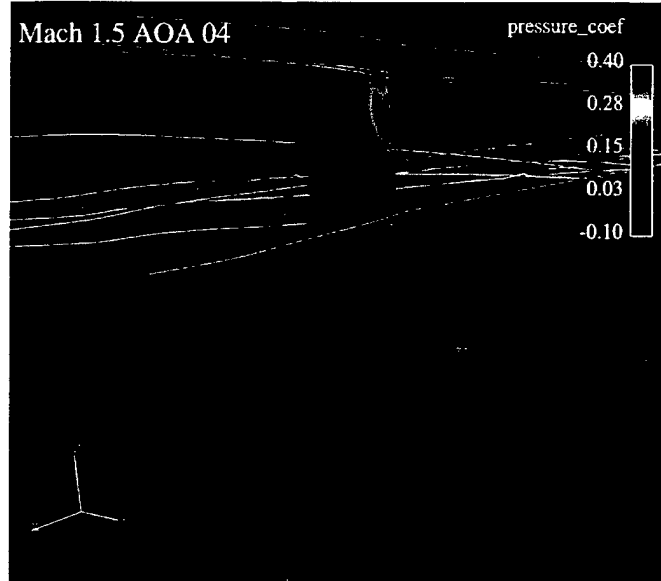
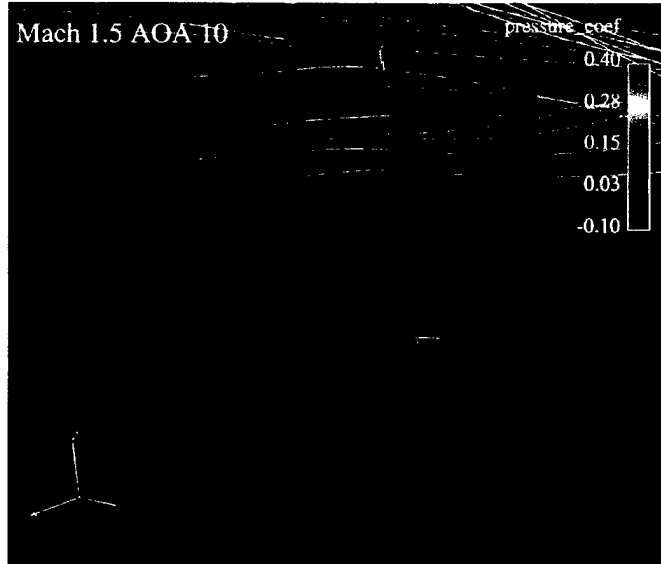


Figure 13. C_p contours on missile surface and axial plane behind canards for $\delta = 10^\circ$ and $\alpha = 0^\circ, 4^\circ$, and 10° at (a–c) $M = 1.5$ and (d–f) $M = 3.0$.

The canard deflection should give the missile a clockwise (when viewed from rear), or positive, rolling moment. At $M = 1.5$, the C_l is actually negative until $\alpha > 8^\circ$. This adverse roll can be explained by examining the pressure distribution and forces on the tail fins. A high-pressure region on the starboard side of the leeward fin at $\alpha = 4^\circ$ can be seen in Figure 14a (and Figure 12b). Although not shown in the figures, a similar high-pressure region was also on the windward side of the starboard fin. These unbalanced pressures on the tail fins are enough to



(a)

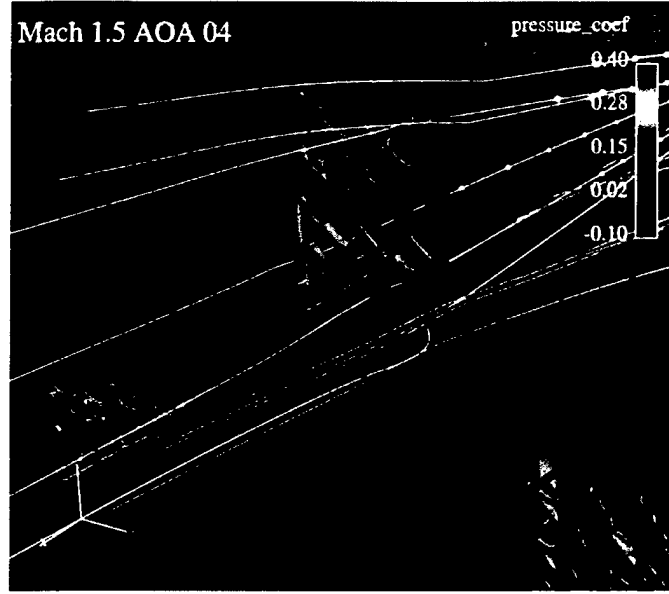


(b)

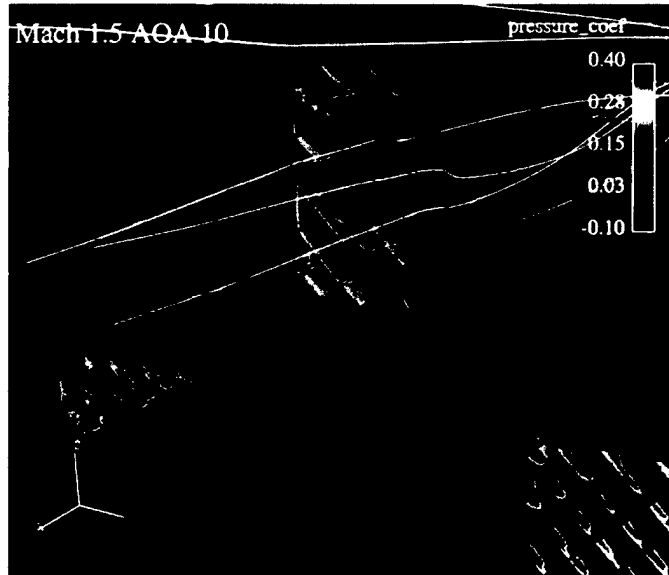
Figure 14. C_p contours on planar fins at $M = 1.5$ and at (a) $\alpha = 4^\circ$ and (b) $\alpha = 10^\circ$.

reverse the rolling moment. At $\alpha = 10^\circ$, the effect is much lower, which appears to be primarily due to the vortices trailing the port, starboard, and leeward canards missing the tail fins entirely. In fact, there are unbalanced forces (Figure 14b and Figure 12c) that act in addition to the canard forces to induce added positive roll.

Similar flowfield results were observed for the grid fin case (Figure 15). Although there was still a nonuniform pressure distribution on the fins, the characteristic geometry of the grid fins alleviated the unwanted rolling moment effect. At $\alpha = 0$, the unwanted rolling moment at



(a)



(b)

Figure 15. C_p contours on grid fins at $M = 1.5$ and at (a) $\alpha = 4^\circ$ and (b) $\alpha = 10^\circ$.

$M = 1.5$ observed in the planar fin case is eliminated (Figure 10). There is still a range between $4^\circ < \alpha < 7^\circ$ that the effectiveness of the canards is severely reduced, but there is still an improvement over the planar tail fins. These results are shown quantitatively in section 3.3, where the forces on the control surfaces are presented.

Scientific visualization movies indicated that the adverse forces on the missile and fins were due to a combination of the canard-trailing vortices interacting with both the tail fins and the crossflow separation region on the leeward side of the missile. The lack of adverse rolling

moment effects at $M = 3.0$ appears to be due directly to the canard-trailing vortices having a lower strength at the higher Mach number. Plots of vorticity magnitude at several axial planes are shown in Figure 16 for the $M = 1.5$ cases and Figure 17 for the $M = 3.0$ cases, both with $\delta = 10^\circ$. At $M = 1.5$ (Figure 16) the canard-trailing vortices have retained significant strength when they reach the tail fins. However, at $M = 3.0$ (Figure 17) the canard-trailing vortices have lost much of their strength by the time they reach halfway down the missile length ($x/D = 8$).

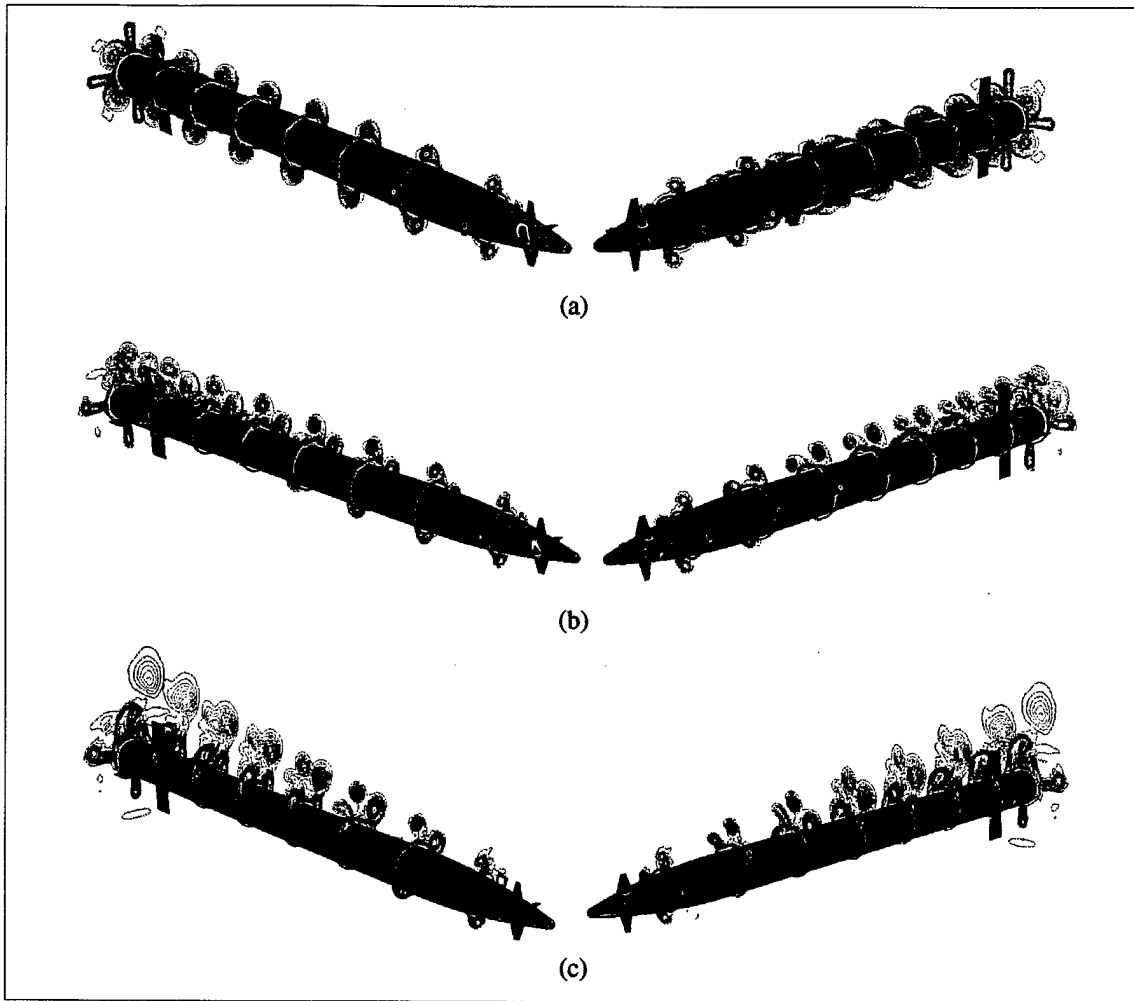


Figure 16. C_p contours (range: -0.1–0.3) on missile surfaces and vorticity magnitude contours (range: 0–50000) on axial cross-planes at 2, 4, 6, 8, 10, 12, 14, and 16 cal. for planar fin case with $\delta = 10^\circ$ at $M = 1.5$ and (a) $\alpha = 0^\circ$, (b) $\alpha = 4^\circ$, and (c) $\alpha = 10^\circ$.

Other than the lower vorticity magnitude at the higher Mach number, the general characteristics of the trailing vortices are similar at both Mach numbers. At $\alpha = 0^\circ$, the trailing vortices shift counterclockwise (when viewed from rear) and pass between the fins, but closer to the fin directly behind the respective canard. There also appears to be a small interaction with the

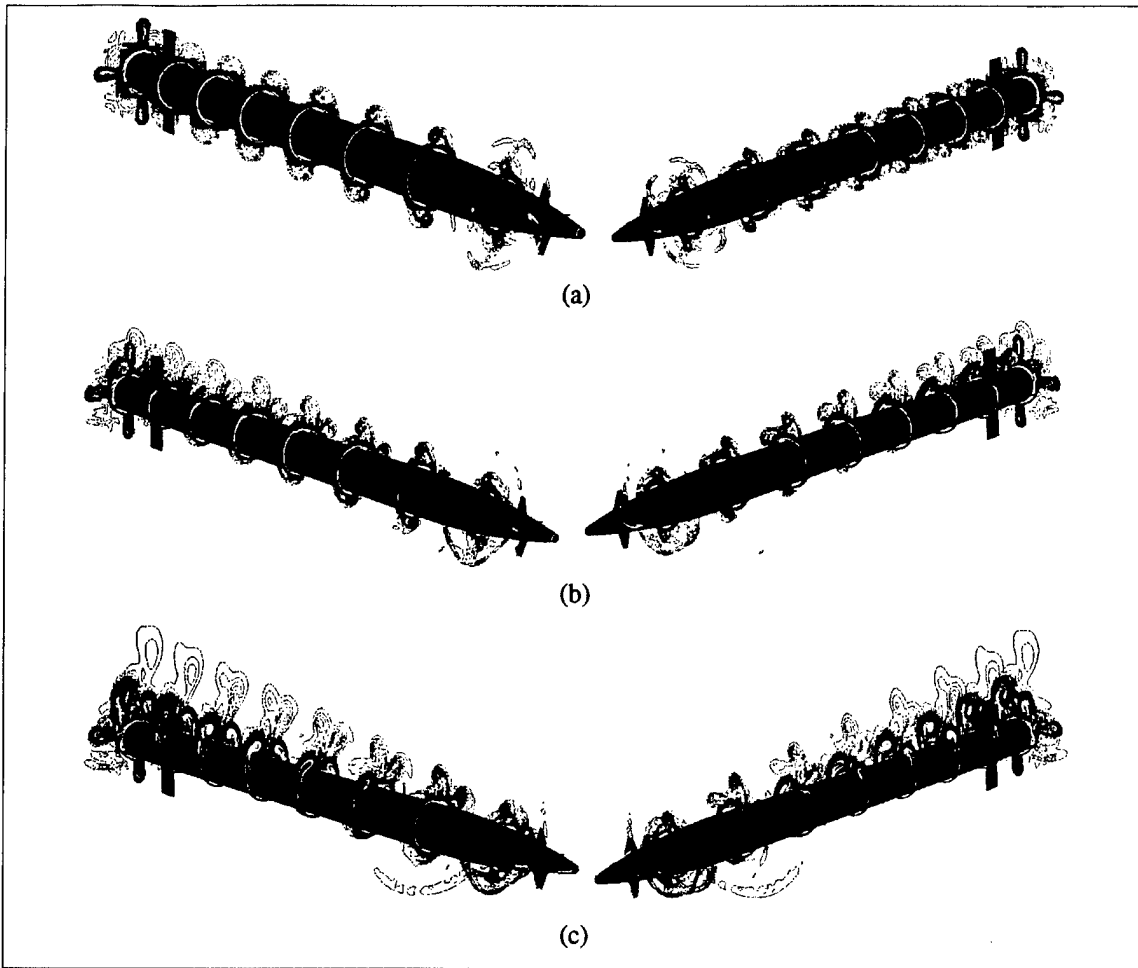


Figure 17. C_p contours (range: -0.1–0.3) on missile surfaces and vorticity magnitude contours (range: 0–50000) on axial cross-planes at 2, 4, 6, 8, 10, 12, 14, and 16 cal. for planar fin case with $\delta = 10^\circ$ at $M = 3.0$ and (a) $\alpha = 0^\circ$, (b) $\alpha = 4^\circ$, and (c) $\alpha = 10^\circ$.

missile boundary layer. At $\alpha = 4^\circ$, the windward canard-trailing vortex merges with the boundary layer vorticity at about $x/D = 8$. The leeward canard-trailing vortex passes near the tip of the leeward fin. The trailing vortices from the port and starboard canards move to the leeward side of the missile and begin to merge with the leeward canard-trailing vortex just behind the leeward fin. At $\alpha = 10^\circ$, the windward canard-trailing vortex merges with the boundary layer vorticity at about $x/D = 4$. The vortices from the other three canards merge on the leeward side of the missile at about $x/D = 10$ and pass over the tail fins. At $\alpha = 10^\circ$, the crossflow separation vortices primarily interact with the leeward tail fin. From these visualizations, it appears that the interaction of the trailing vortices with the tail fins is primarily responsible for the adverse forces on the tail fins that affect the rolling moment.

For the $\delta = 0^\circ$ cases (Figure 18) at $M = 1.5$, the strength of the canard-trailing vortices is less than that observed for the $\delta = 10^\circ$ cases. The strength of the port and starboard canard-trailing

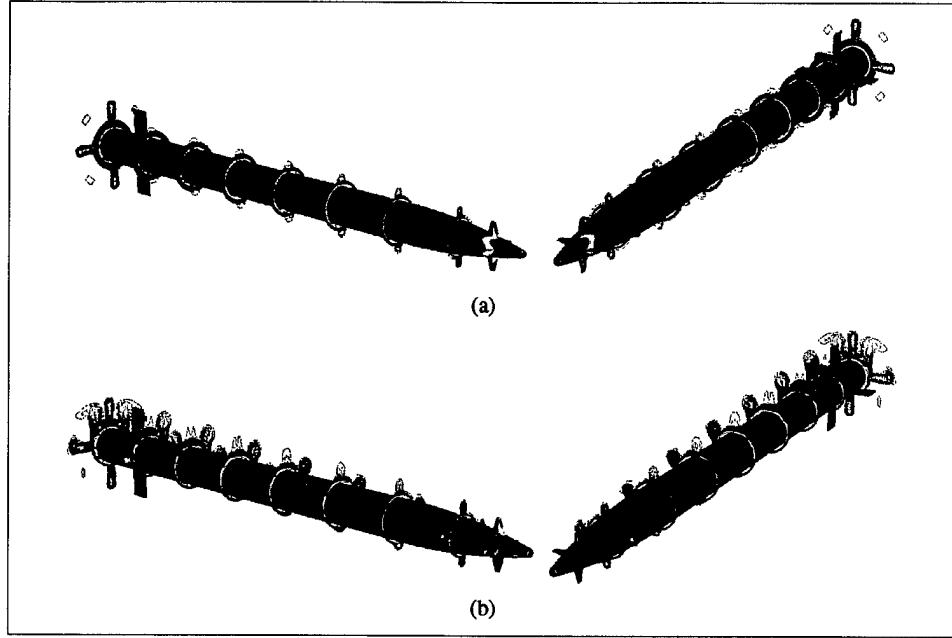


Figure 18. C_p contours (range: -0.1–0.3) on missile surfaces and vorticity magnitude contours (range: 0–50000) on axial cross-planes at 2, 4, 6, 8, 10, 12, 14, and 16 cal. for planar fin case with $\delta = 0^\circ$ at $M = 1.5$ and (a) $\alpha = 0^\circ$ and (b) $\alpha = 4^\circ$.

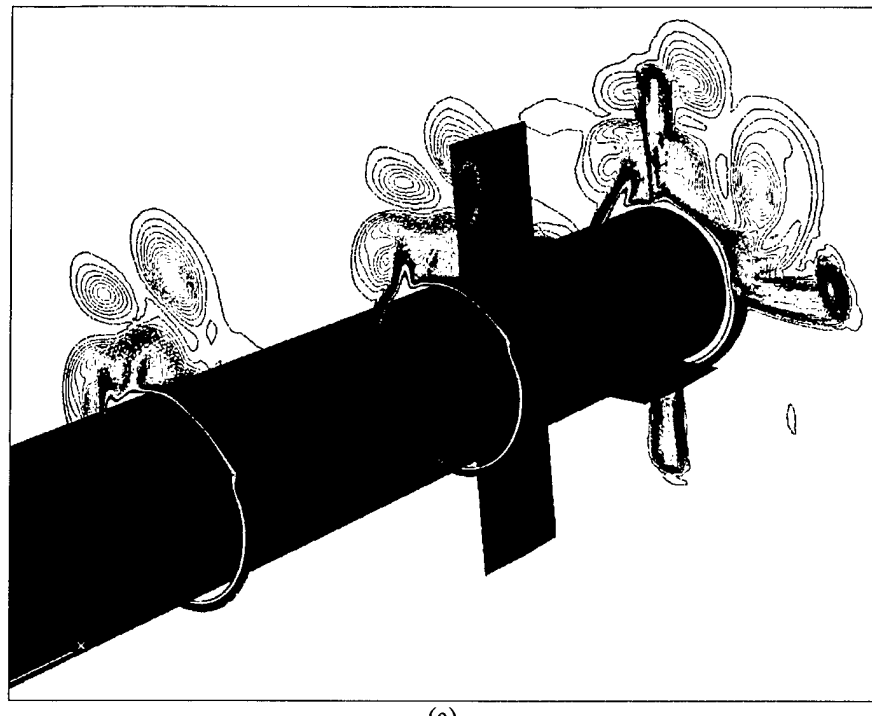
vortices increases as α increases; however, the flow is symmetric near the tail fins and no adverse rolling moment is produced.

The effect of the grid fins on the canard-trailing vortices is shown in Figure 19, which compares the vorticity magnitude on several cross-planes near the tail of the missile for the planar and grid fin cases at $M = 1.5$, $\alpha = 4^\circ$, and $\delta = 10^\circ$. In the planar fin case (Figure 19a) the trailing vortices from the port, starboard, and leeward fins are nearly unchanged after they pass by the leeward tail fin. However, in the grid fin case (Figure 19b), although the trailing vortex from the port fin passes between the port and leeward fin relatively unchanged, the other two vortices are dramatically changed from the interaction with the leeward grid fin. The force on the fin from this interaction does not favor any particular direction, so a large moment is not produced. However, in the planar fin case, the localized high pressure on the leeward fin does cause the adverse rolling moment.

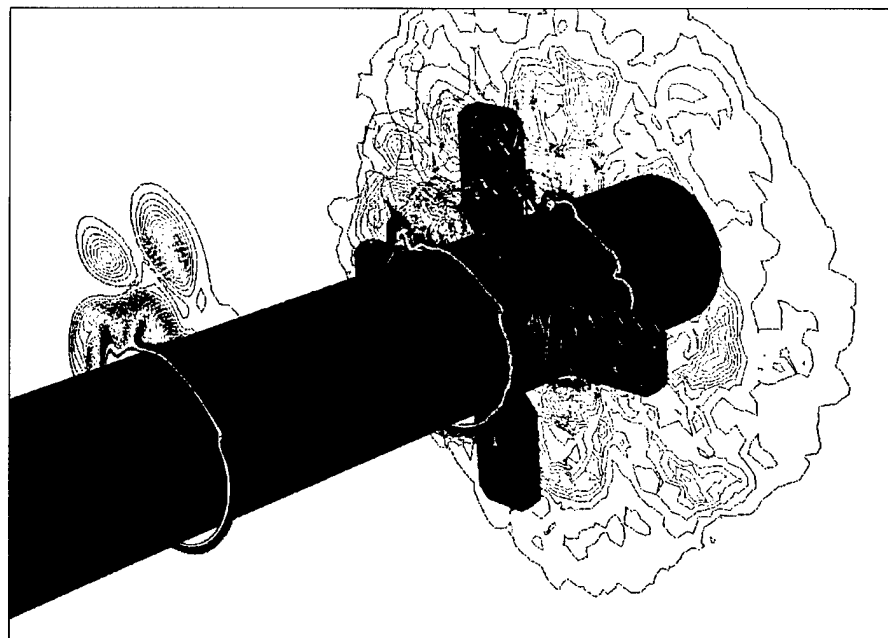
3.3 Control Surface Forces

The forces on the canards and fins are summarized in tabular and graphical form in Appendices C–F. Some results are presented in this section to quantify the trends observed in the flow visualizations.

The forces on the leeward and windward fins resulting in the adverse rolling moment are shown in Figure 20, which shows the side force coefficient on each fin for the planar and grid fin cases at $\delta = 10^\circ$. In the planar fin case, the windward fin (fin2) is at a nearly constant, small positive

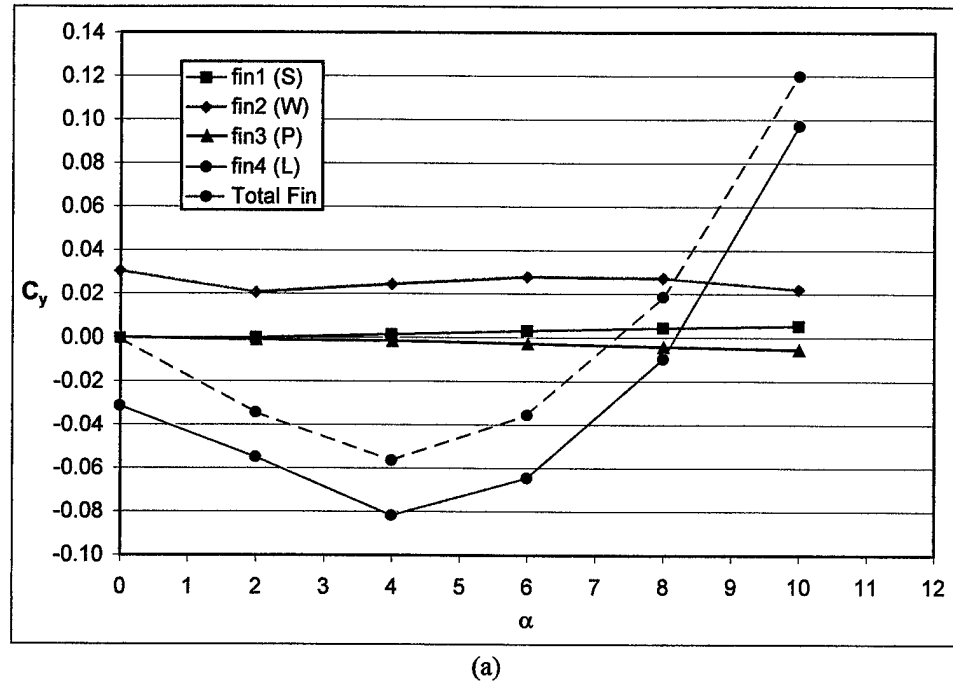


(a)

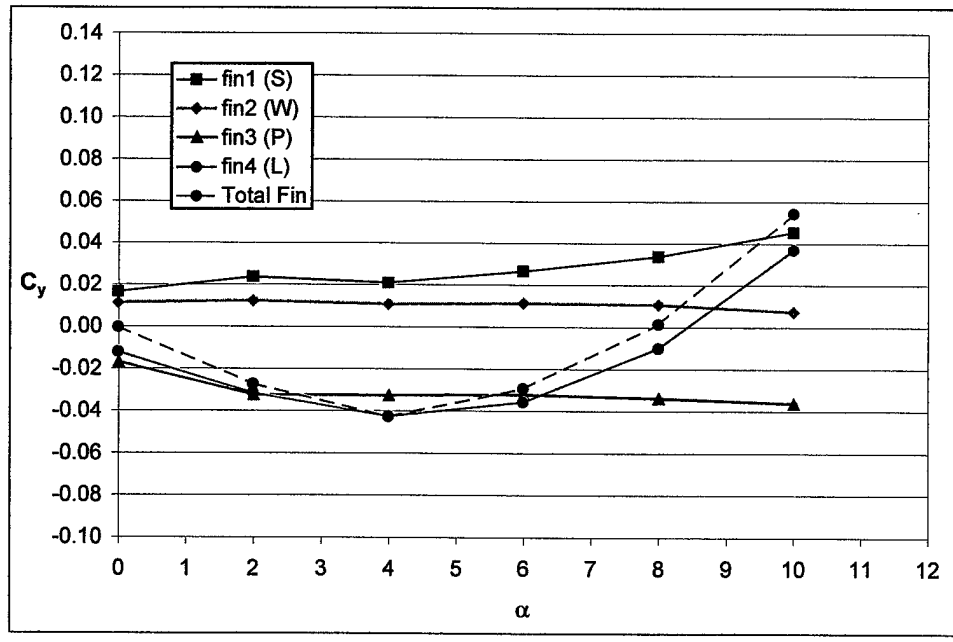


(b)

Figure 19. C_p contours (range: -0.1–0.3) on missile surfaces and vorticity magnitude contours (range: 0–50000) on axial cross-planes at (a) 12, 14, and 16 cal. for the planar fin case and at (b) 12, 14, and 15 cal. for the grid fin case with $\delta = 10^\circ$ at $M = 1.5$ and $\alpha = 4^\circ$.



(a)



(b)

Figure 20. Side force coefficient on tail fins for (a) planar fin and (b) grid fin case for $\delta = 10^\circ$ and $M = 1.5$.

value. The leeward fin (fin 4) is negative until $\alpha > 8^\circ$. This force imbalance clearly produces the adverse roll since the fin force coefficients are of the same order as those on the canards and the larger moment arm of the fins therefore produces moments larger than those produced by the canards. In the grid fin case (Figure 20b), there are still side forces on the windward and leeward fins that tend to induce a negative roll, but this time they are lower and do not reduce the roll effectiveness of the canards as much. Also, observe that the horizontal grid fins produce a side force, unlike the planar fins. This does not affect the roll moment and only adds a very small contribution to missile side force.

Similarly, but to a smaller extent, the normal force on the starboard and port planar fins contributes to the adverse rolling moment. This is illustrated in Figure 21, which shows that the difference in normal force between the port and starboard grid fins is less than that for the planar fins.

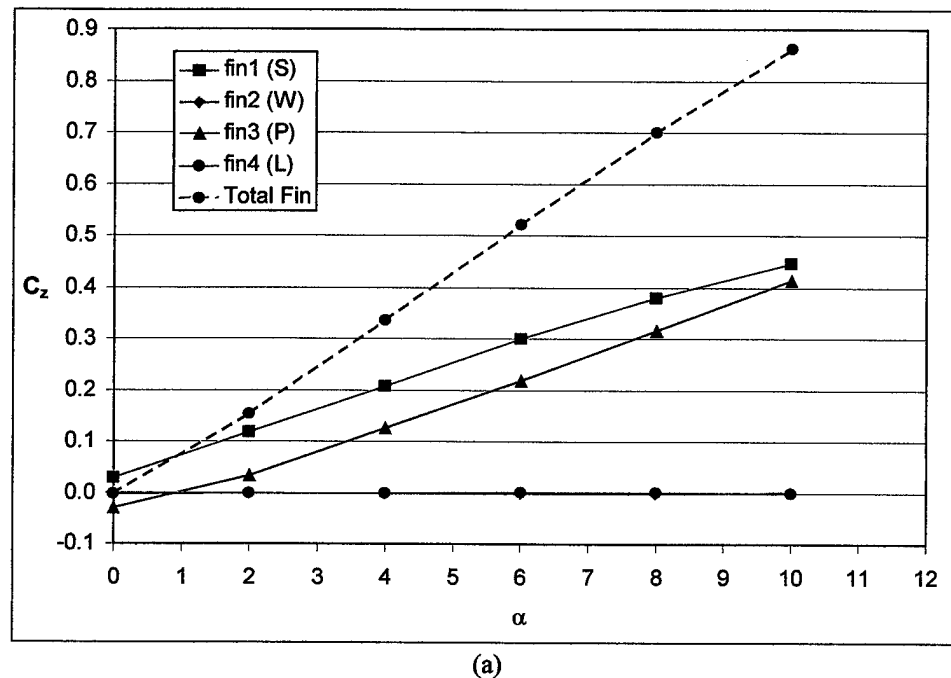
One advantage noted for grid fins over planar fins is that they maintain their effectiveness at high Mach number. This can be observed by comparing Figure 21 and Figure 22, which show the fin normal force for both fin types and both Mach numbers. For this particular grid fin design, at $\alpha = 10^\circ$ and $M = 1.5$, the total fin normal force in the grid fin case is about 65% that in the planar fin case. At $M = 3.0$, the total fin normal force in the planar fin case has decreased over 50%. However, the total fin normal force in the grid fin case has stayed nearly the same as that at $M = 1.5$. The small reduction is mainly due to the normal force on the leeward fin going negative at higher α .

4. Summary and Conclusions

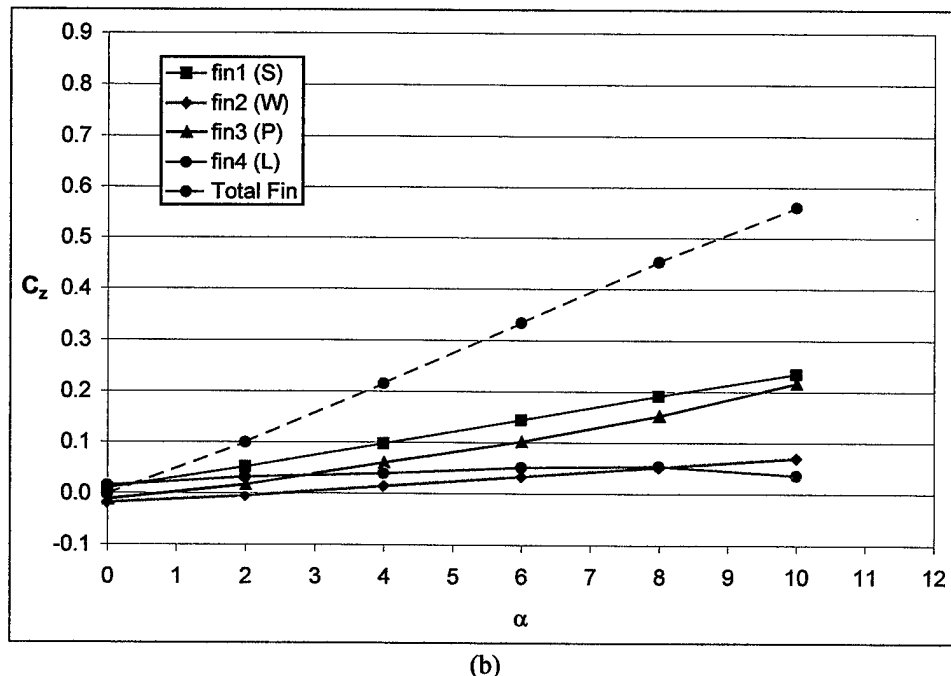
Viscous CFD calculations were used to predict the aerodynamic coefficients and flowfield around a generic canard-controlled missile configuration in supersonic flow. Validation of the computed results was demonstrated by the very good agreement between the computed aerodynamic coefficients and those obtained from wind tunnel measurements.

Visualizations of the flowfield at low supersonic speed showed that the canard downwash and trailing vortices produced a low-pressure region on the starboard side of the missile that, in turn, produced an adverse induced side force. The side force was much lower at the higher supersonic speed.

The visualizations also showed that the canard-trailing vortices interact with the tail fins until α is high enough so that the vortices miss the leeward fin. The pressure differential on the leeward fin produced by the interaction with the canard-trailing vortices is primarily responsible for the adverse induced roll effects observed when planar fins are used.

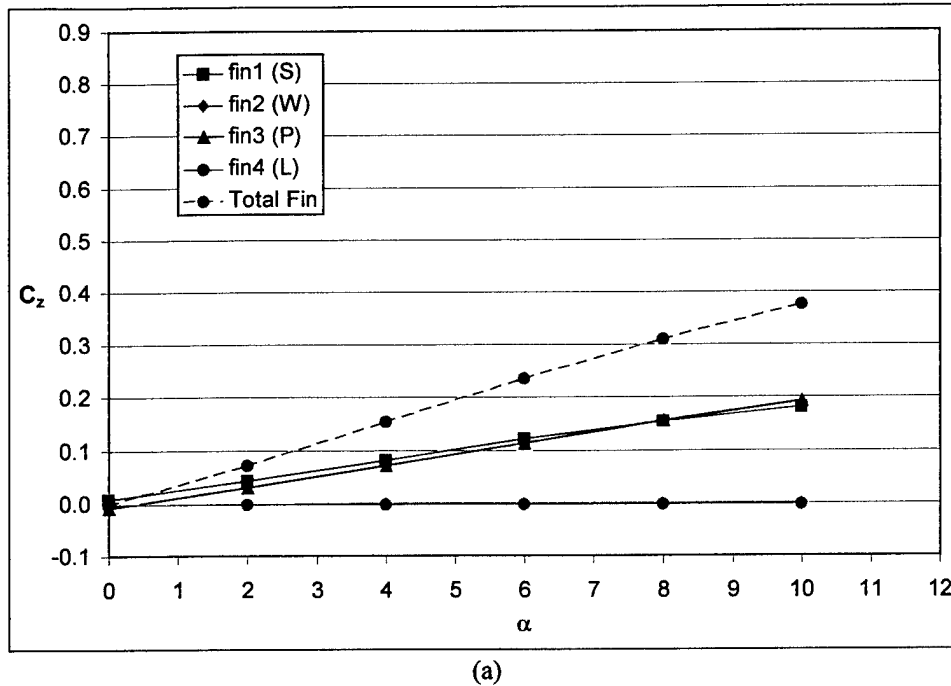


(a)

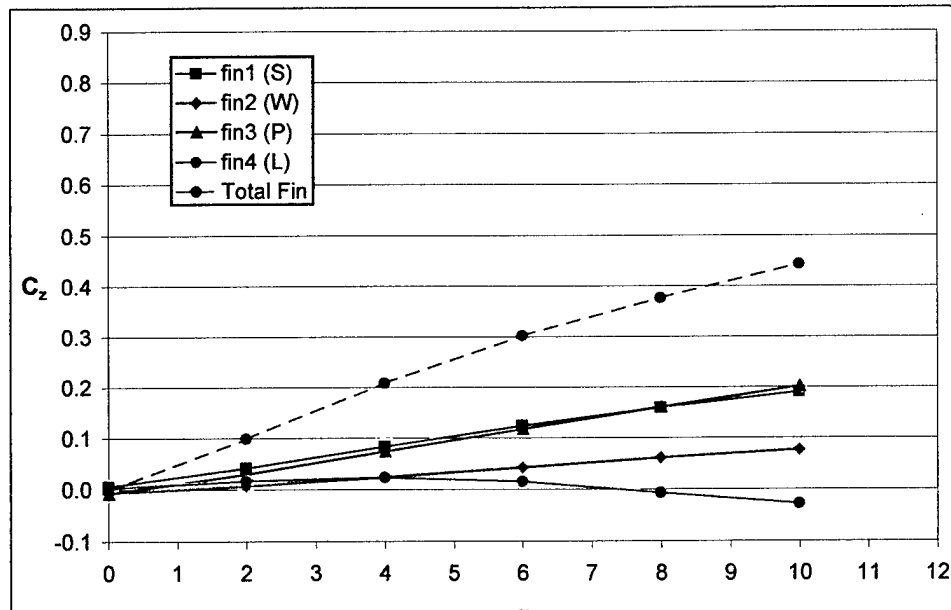


(b)

Figure 21. Normal force coefficient on tail fins for (a) planar fin and (b) grid fin case for $\delta = 10^\circ$ and $M = 1.5$.



(a)



(b)

Figure 22. Normal force coefficient on tail fins for (a) planar fin and (b) grid fin case for $\delta = 10^\circ$ and $M = 3.0$.

Grid tail fins improved the roll-control effectiveness of the canards at low supersonic speed. There was still an uneven pressure distribution on the grid tail fins, produced by the interaction with the canard-trailing vortices. However, the design of the grid fin distributes the pressure differently so that the side forces are lower and do not produce as large a roll moment as the planar fins do.

No adverse rolling moment was observed with no canard deflection or at the higher supersonic speed for either tail fin type. Flow visualizations showed that the intensity of the canard-trailing vortices was much lower in these two cases. Methods to reduce the intensity of the canard trailing vortices, or direct them away from the tail fins, may be two possible ways to alleviate the roll-control problems in munitions using canards for control.

The validated CFD results confirm that the use of grid tail fins dramatically improves the roll effectiveness of the canards at low supersonic speed. Visualizations of the flowfield from the simulations performed in this study help in the understanding of the flow physics and can lead to improved tail fin and canard designs.

5. References

1. Allen, J. M., and A. B. Blair, Jr. "Comparison of Analytical and Experimental Supersonic Aerodynamic Characteristics of a Forward Control Missile." *Journal of Spacecraft and Rockets*, vol. 19, no. 2, pp. 155–159, 1982.
2. Blair, A. B., J. L. Dillon, Jr., and C. B. Watson. "Experimental Study of Tail-Span Effects on a Canard-Controlled Missile." *Journal of Spacecraft and Rockets*, vol. 30, no. 5, pp. 635–640, 1993.
3. Blair, A. B., Jr. "Supersonic Aerodynamic Characteristics of a Maneuvering Canard-Controlled Missile With Fixed and Free-Rolling Tail Fins." SAE Paper 90-1993, Society of Automotive Engineers, Warrendale, PA, October 1990.
4. Burt, J. R., Jr. "The Effectiveness of Canards for Roll Control." Technical Report RD-77-8, U.S. Army Missile Command, Redstone Arsenal, AL, November 1976.
5. Miller, M. "Aerodynamic Investigation of a Canard Controlled Missile Using Planar and Grid Fin Tail." Dynetics, Inc., Huntsville, AL, to be published.
6. Washington, W. D., and M. S. Miller. "Grid Fins—A New Concept for Missile Stability and Control." AIAA Paper 93-0035, American Institute of Aeronautics and Astronautics, Reston, VA, January 1993.

7. Washington, W. D., and M. S. Miller. "Experimental Investigations of Grid Fin Aerodynamics: A Synopsis of Nine Wind Tunnel and Three Flight Tests." *Proceedings of the NATO RTO Applied Vehicle Technology Panel Symposium on Missile Aerodynamics*, RTO-MP-5, NATO Research and Technology Organization, Neuilly-Sur-Seine Cedex, France, pp. 10-1–10-14, 1998.
8. Miller, M. S., and W. D. Washington. "An Experimental Investigation of Grid Fin Drag Reduction Techniques." AIAA Paper 94-1914-CP, American Institute of Aeronautics and Astronautics, Reston, VA, June 1994.
9. Simpson, G. M., and A. J. Sadler. "Lattice Controls: A Comparison With Conventional, Planar Fins." *Proceedings of the NATO RTO Applied Vehicle Technology Panel Symposium on Missile Aerodynamics*, RTO-MP-5, NATO Research and Technology Organization, Neuilly-Sur-Seine Cedex, France, pp. 9-1–9-10, 1998.
10. DeSpirito, J., H. L. Edge, P. Weinacht, J. Sahu, and S. P. G. Dinavahi. "Computational Fluid Dynamics Analysis of a Missile With Grid Fins." *Journal of Spacecraft and Rockets*, vol. 38, no. 5, pp. 711–718, 2001.
11. DeSpirito, J., and J. Sahu. "Viscous CFD Calculations of Grid Fin Missile Aerodynamics in the Supersonic Flow Regime." AIAA Paper 2001-2057, American Institute of Aeronautics and Astronautics, Reston, VA, January 2001.
12. Fluent, Inc. "Fluent 5.0 User's Guide." Vol. 2, Lebanon, NH, 1998.
13. Moore, F. G., R. M. McInville, and T. C. Hymer. "Application of the 1998 Version of the Aeroprediction Code." *Journal of Spacecraft and Rockets*, vol. 36, no. 5, pp. 633–645, 1999.
14. Abate, G., G. Winchenbach, and W. Hathaway. "Transonic Aerodynamic and Scaling Issues for Lattice Fin Projectiles Tested in a Ballistic Range." *Proceedings of the 19th International Symposium on Ballistics*, National Defense Industrial Association, Arlington, VA, 2001.

Appendix A. Aerodynamic Coefficients for Planar Fin Case

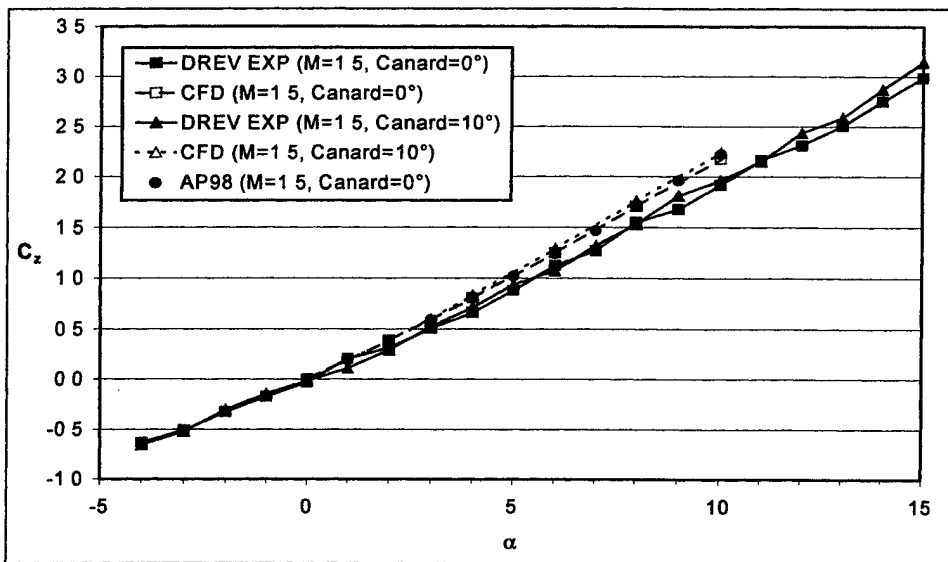


Figure A-1. Normal force for planar fin case at Mach 1.5.

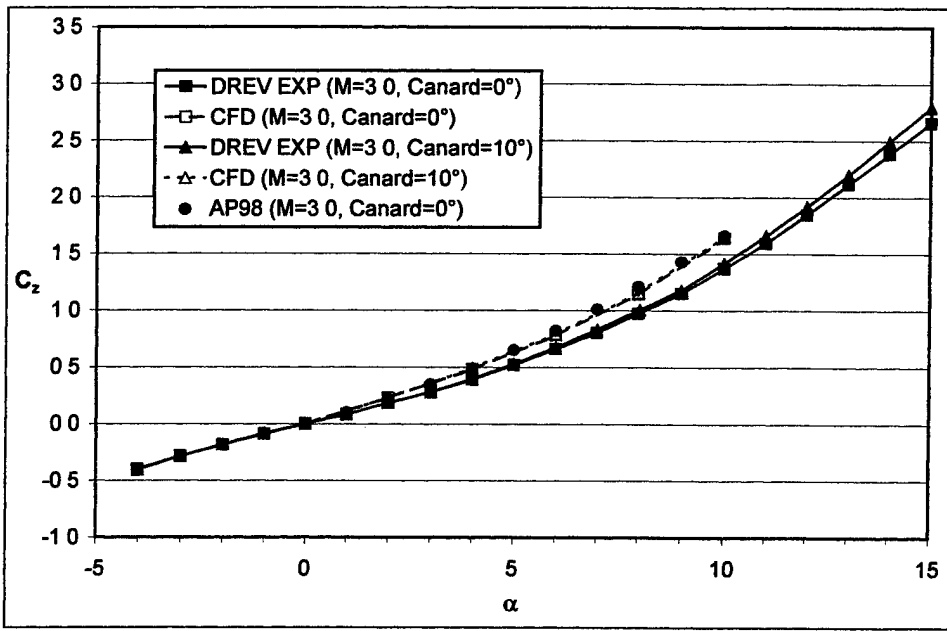


Figure A-2. Normal force for planar fin case at Mach 3.0.

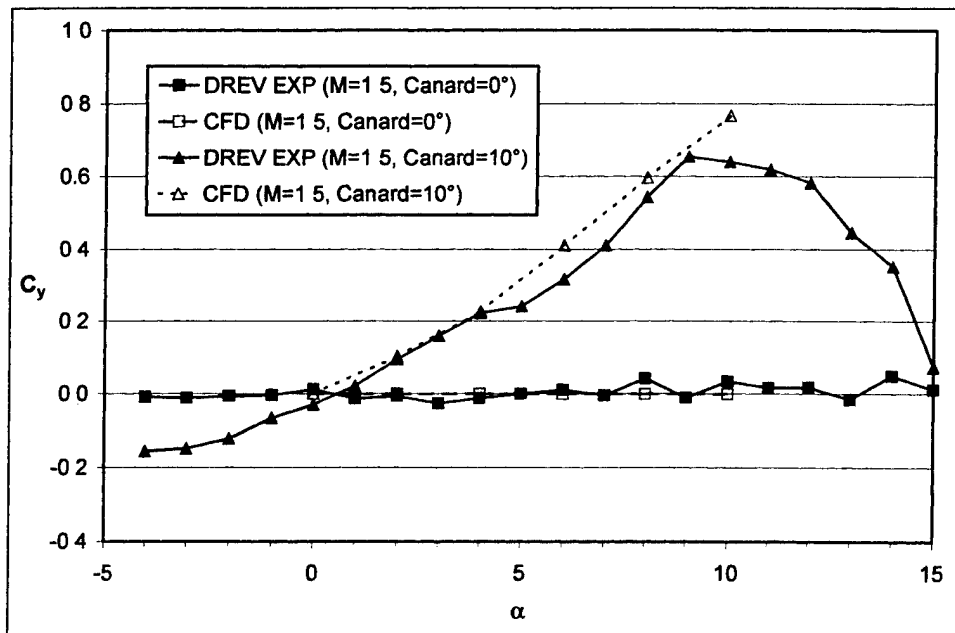


Figure A-3. Side force for planar fin case at Mach 1.5.

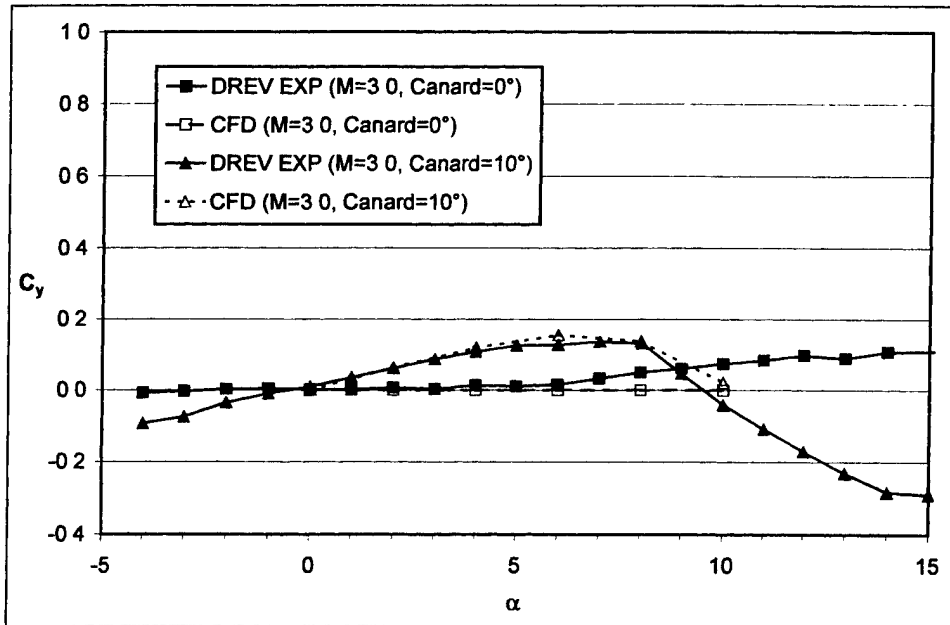


Figure A-4. Side force for planar fin case at Mach 3.0.

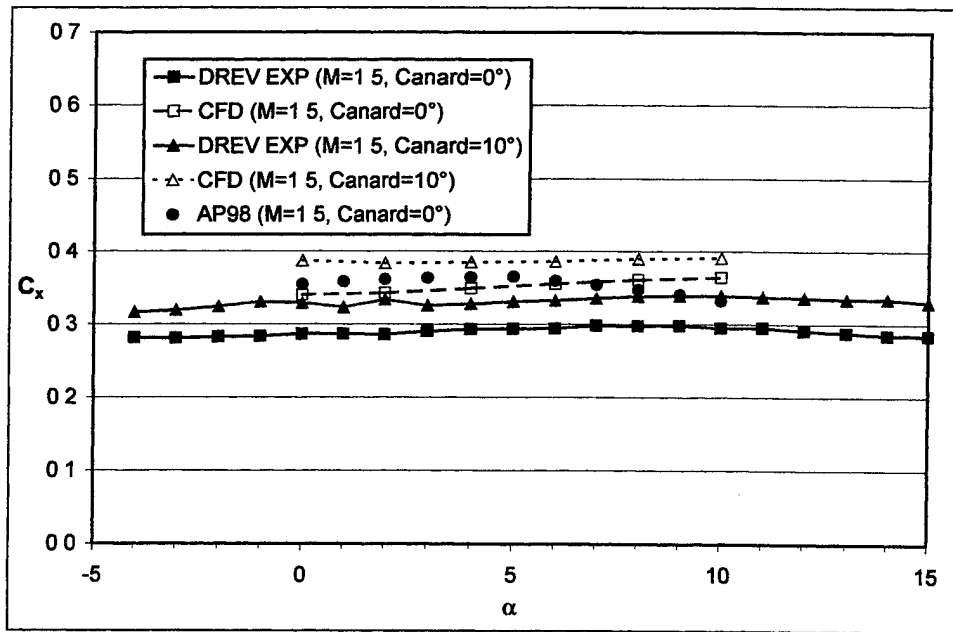


Figure A-5. Axial force for planar fin case at Mach 1.5.

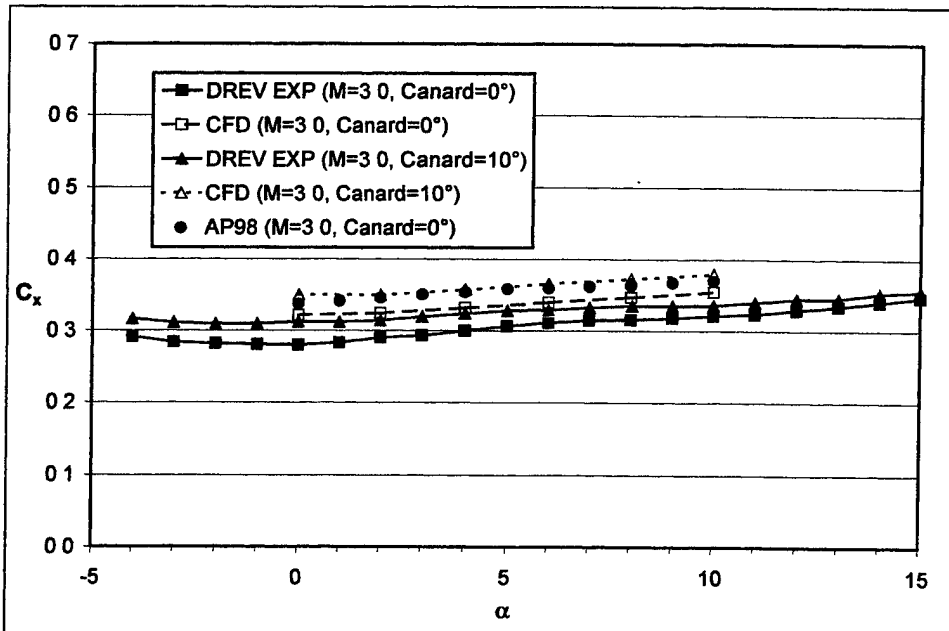


Figure A-6. Axial force for planar fin case at Mach 3.0.

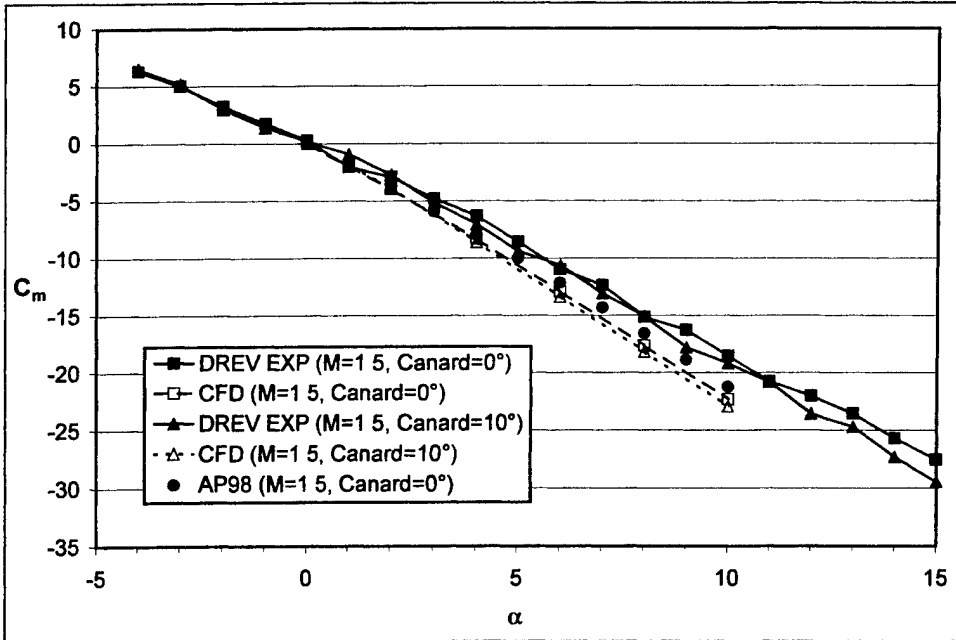


Figure A-7. Pitching moment about nose for planar fin case at Mach 1.5.

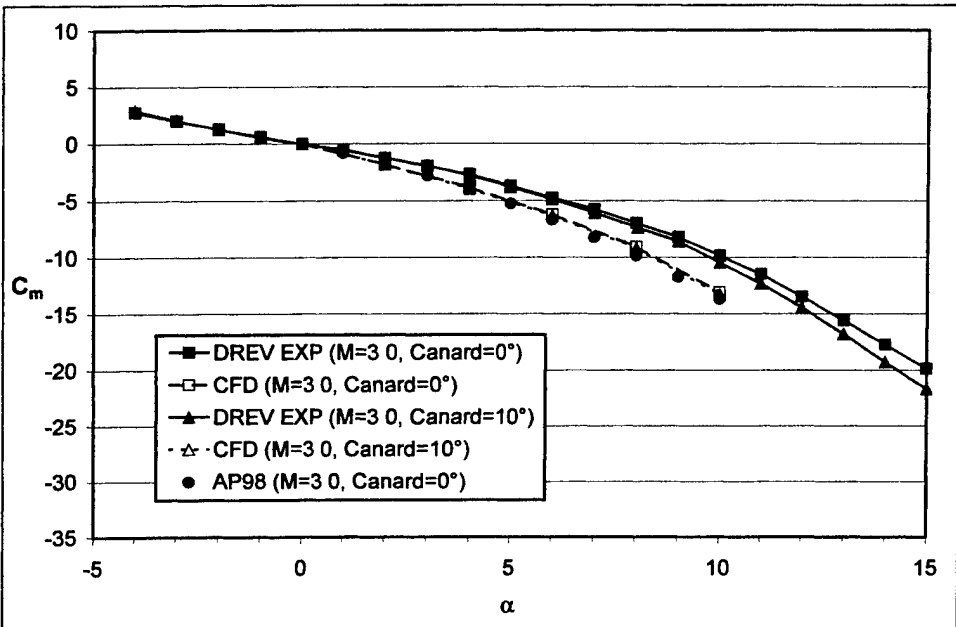


Figure A-8. Pitching moment about nose for planar fin case at Mach 3.0.

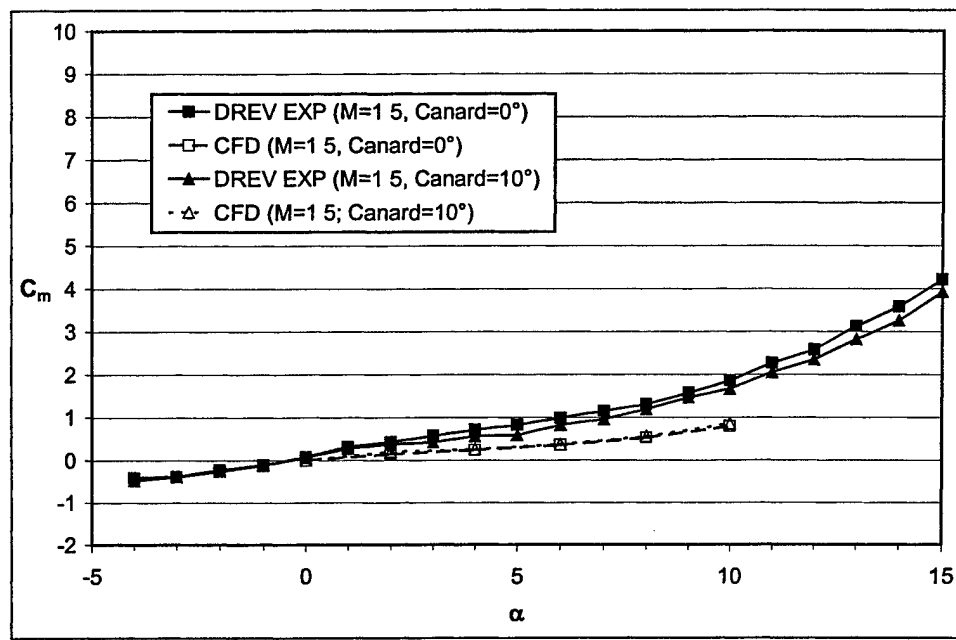


Figure A-9. Pitching moment about moment reference point (MRP) for planar fin case at Mach 1.5.

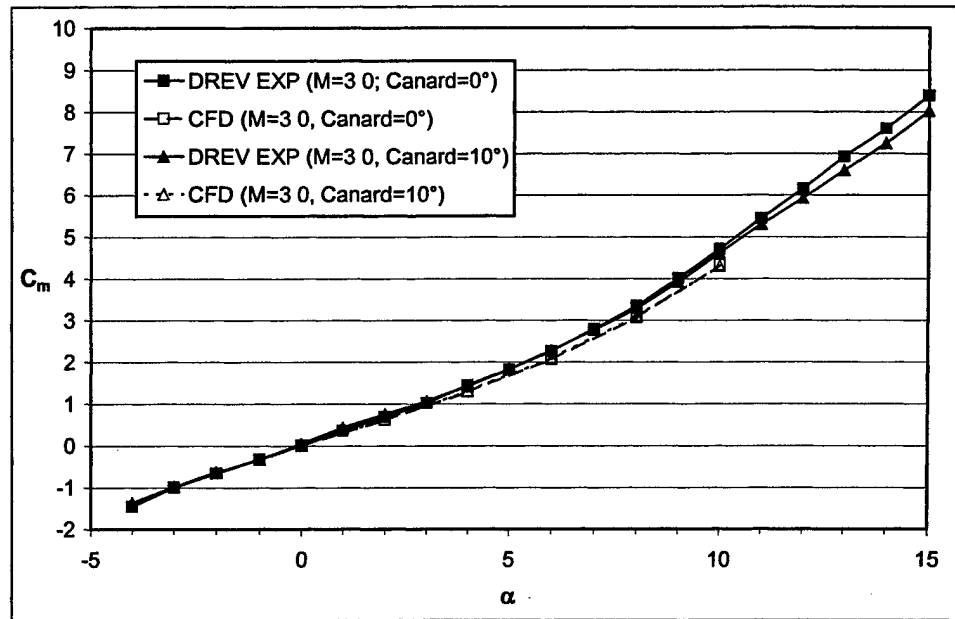


Figure A-10. Pitching moment about MRP for planar fin case at Mach 3.0.

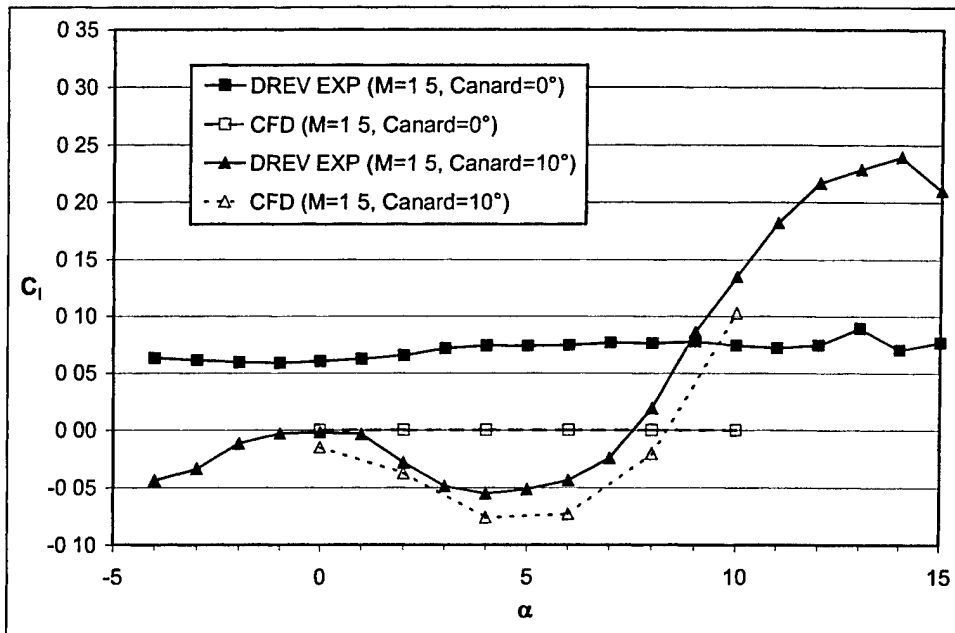


Figure A-11. Rolling moment for planar fin case at Mach 1.5.

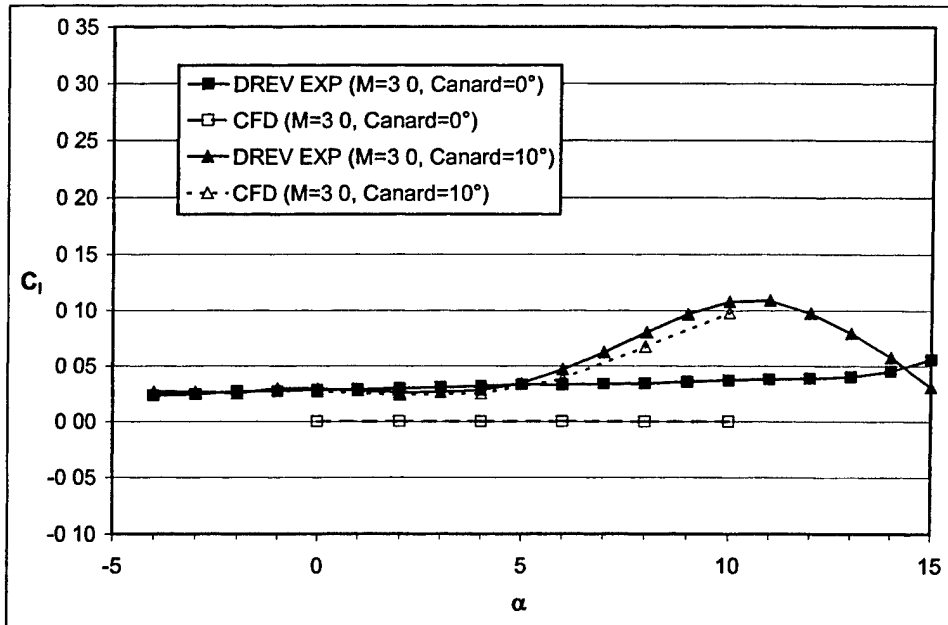


Figure A-12. Rolling moment for planar fin case at Mach 3.0.

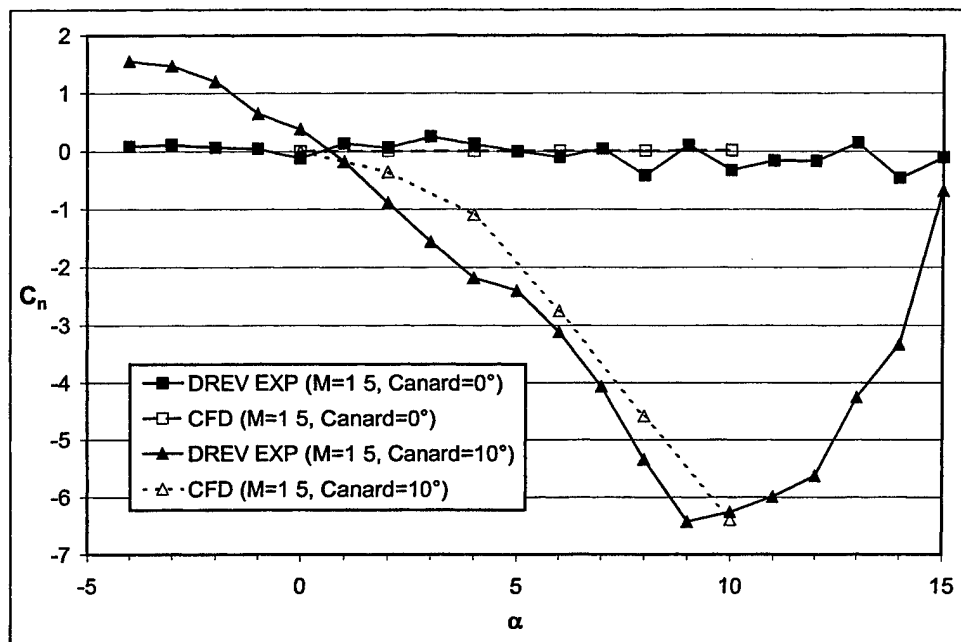


Figure A-13. Yawing moment for planar fin case at Mach 1.5.

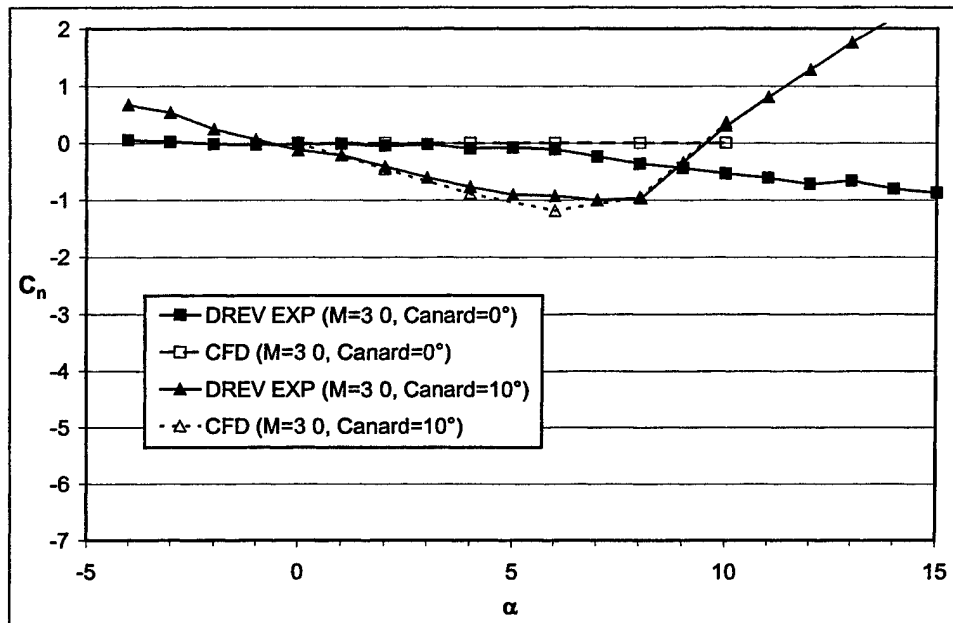


Figure A-14. Yawing moment for planar fin case at Mach 3.0.

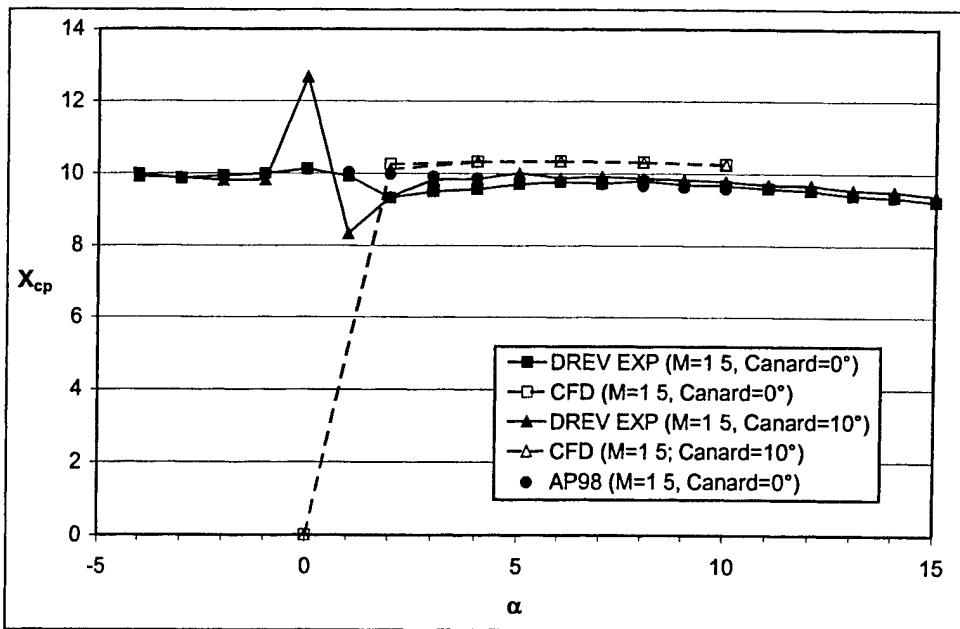


Figure A-15. Center of pressure location from nose for planar fin case at Mach 1.5.

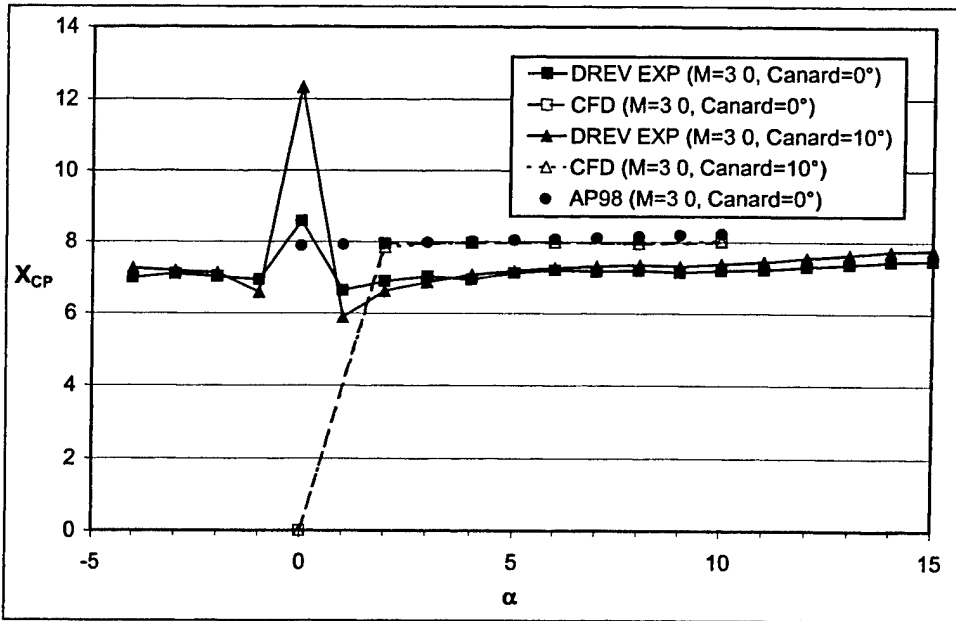


Figure A-16. Center of pressure location from nose for planar fin case at Mach 3.0.

Appendix B. Aerodynamic Coefficients for Grid Fin Case

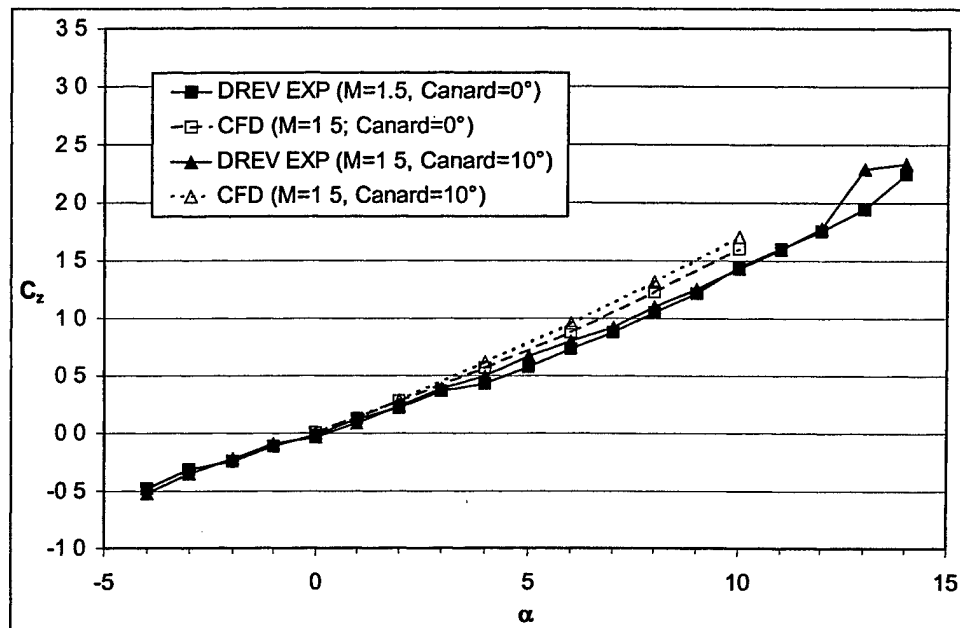


Figure B-1. Normal force for grid fin case at Mach 1.5.

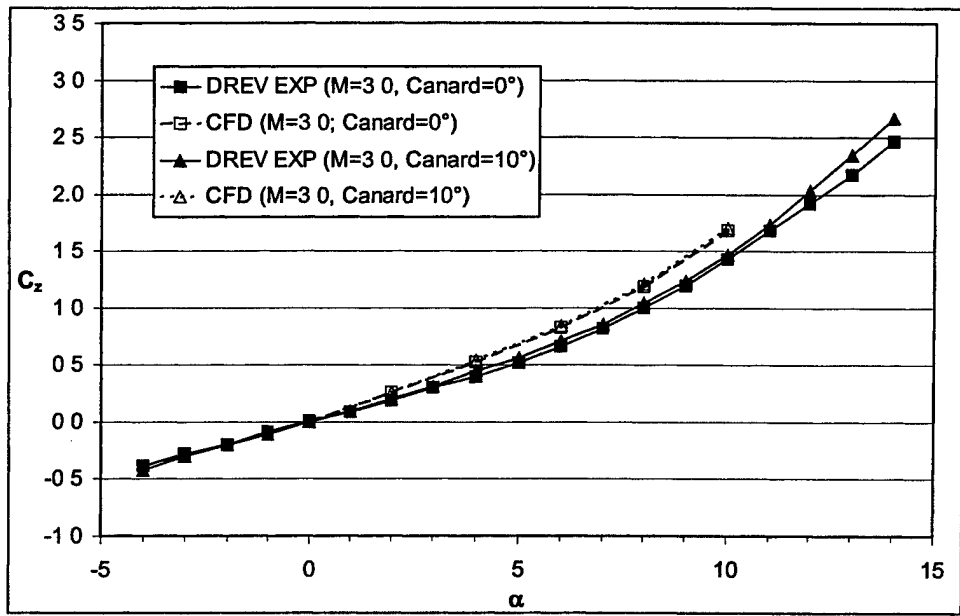


Figure B-2. Normal force for grid fin case at Mach 3.0.

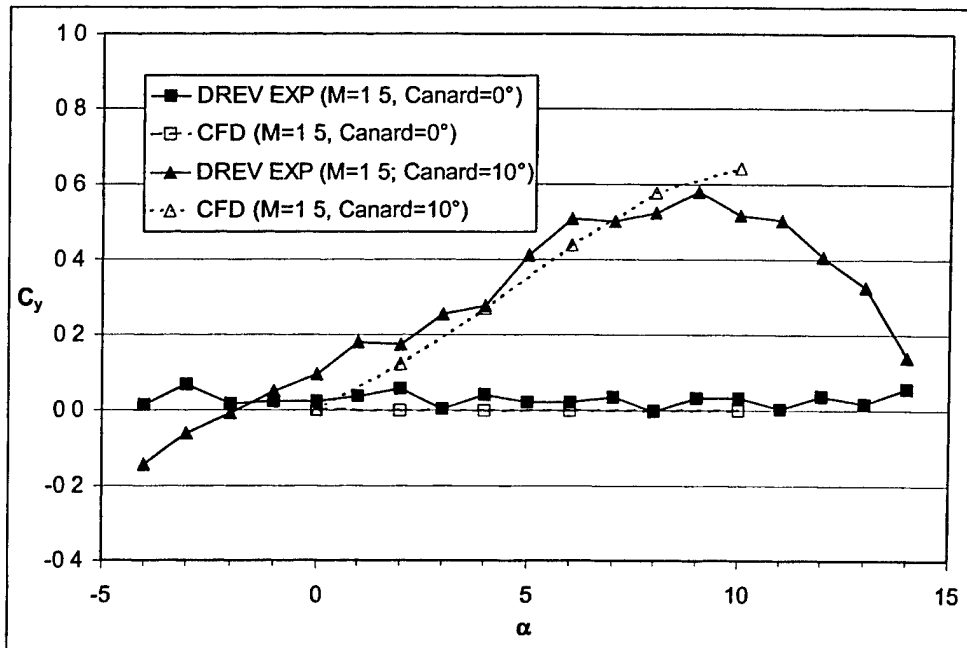


Figure B-3. Side force for grid fin case at Mach 1.5.

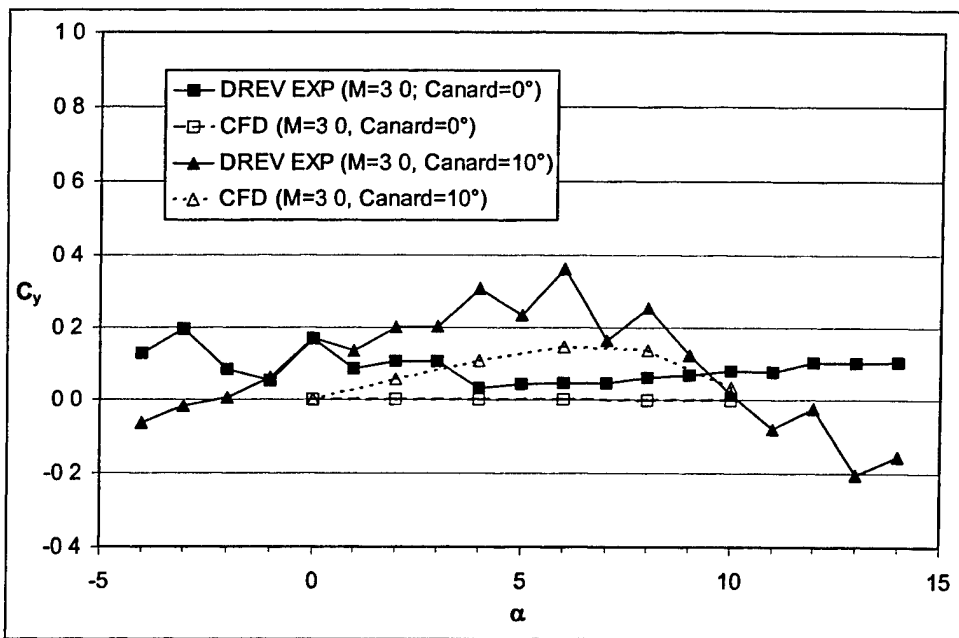


Figure B-4. Side force for grid fin case at Mach 3.0.

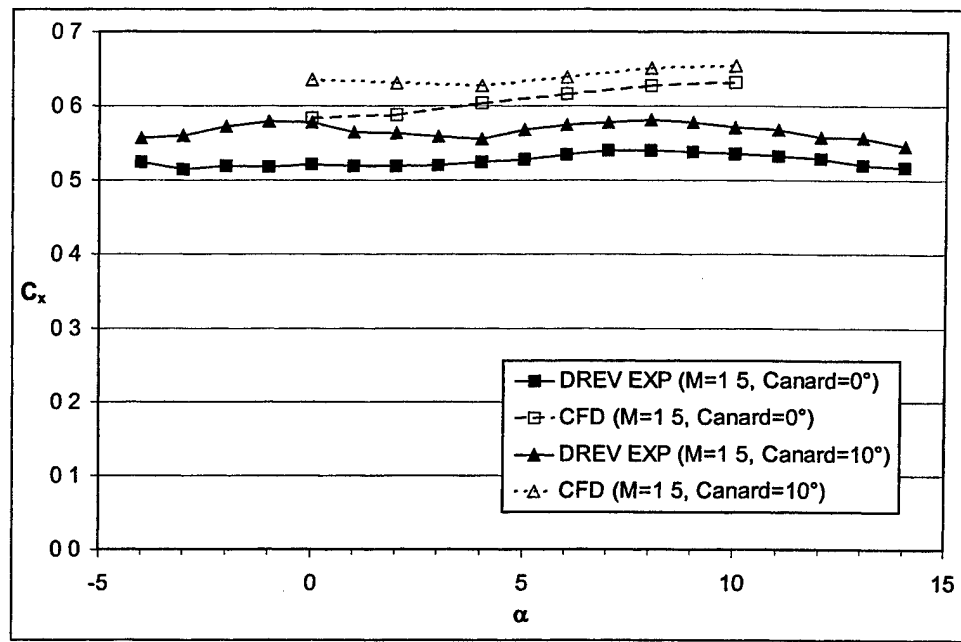


Figure B-5. Axial force for grid fin case at Mach 1.5.

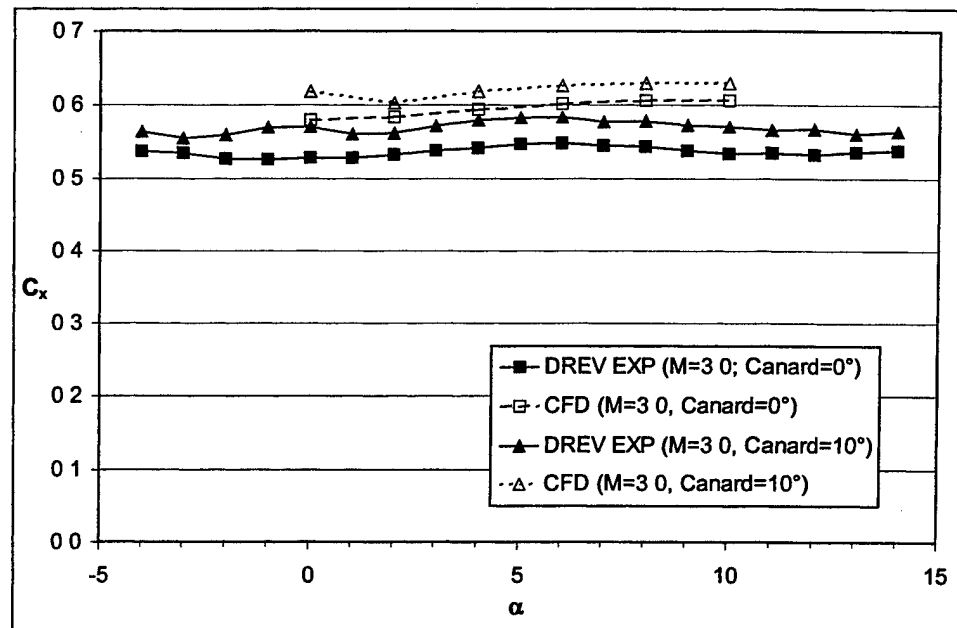


Figure B-6. Axial force for grid fin case at Mach 3.0.

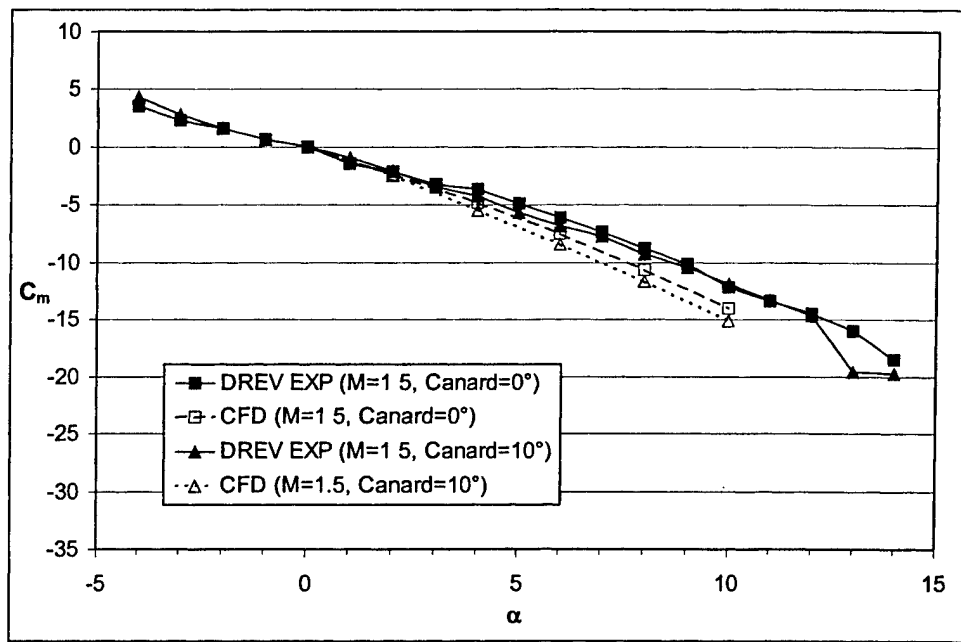


Figure B-7. Pitching moment about nose for grid fin case at Mach 1.5.

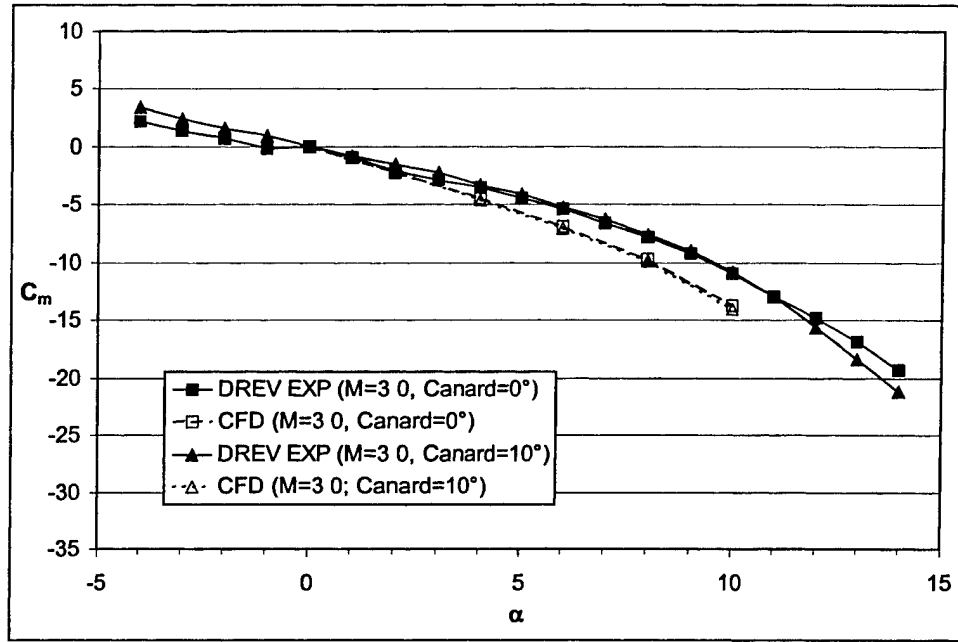


Figure B-8. Pitching moment about nose for grid fin case at Mach 3.0.

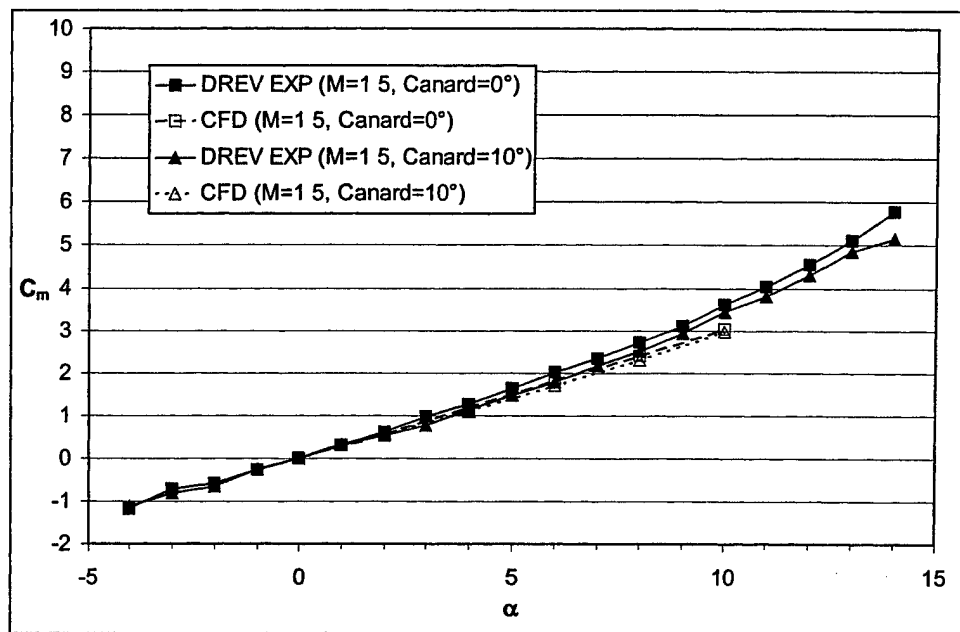


Figure B-9. Pitching moment about moment reference point (MRP) for grid fin case at Mach 1.5.

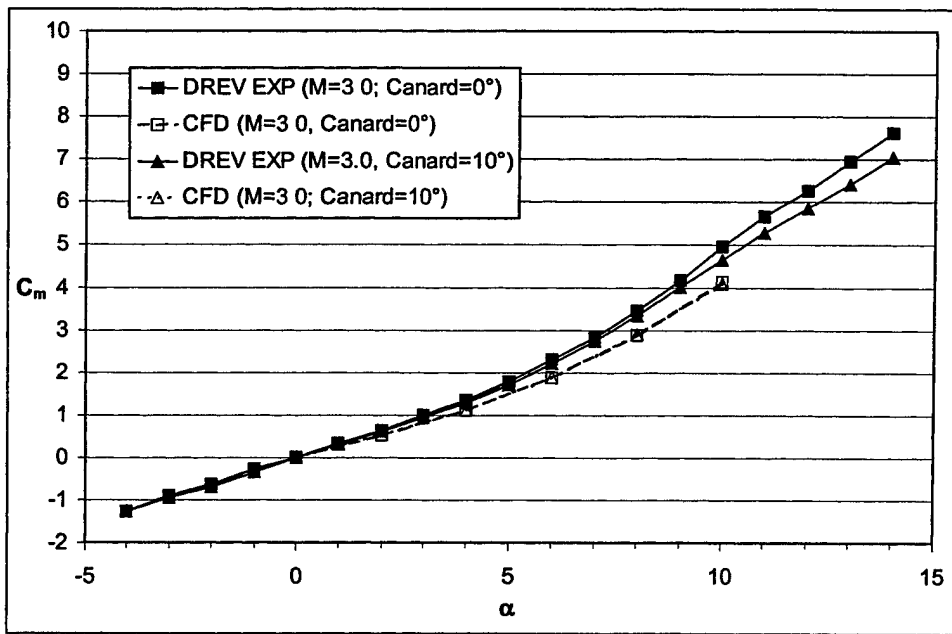


Figure B-10. Pitching moment about MRP for grid fin case at Mach 3.0.

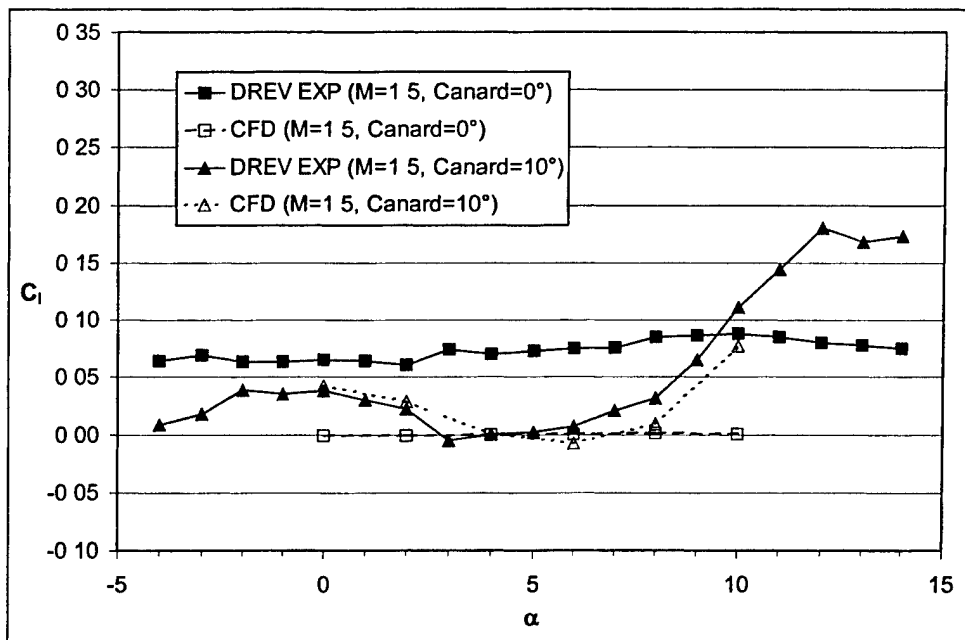


Figure B-11. Rolling moment for grid fin case at Mach 1.5.

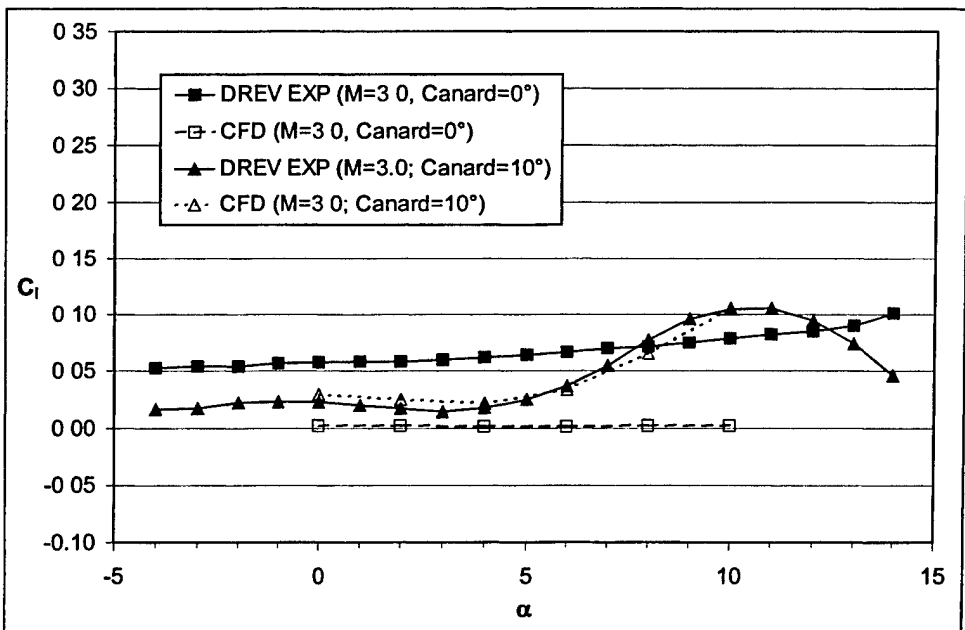


Figure B-12. Rolling moment for grid fin case at Mach 3.0.

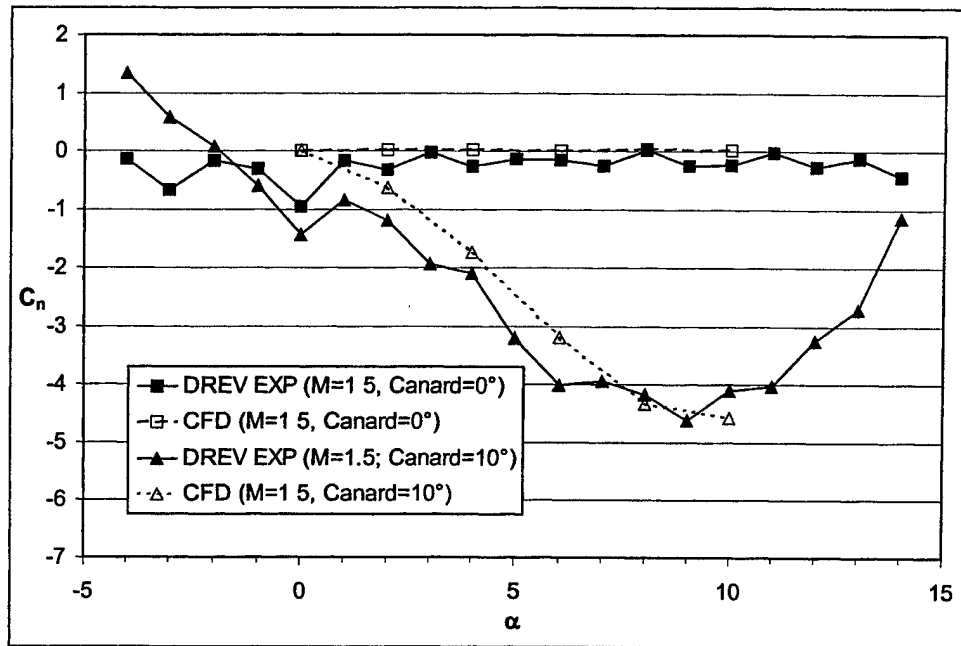


Figure B-13. Yawning moment for grid fin case at Mach 1.5.

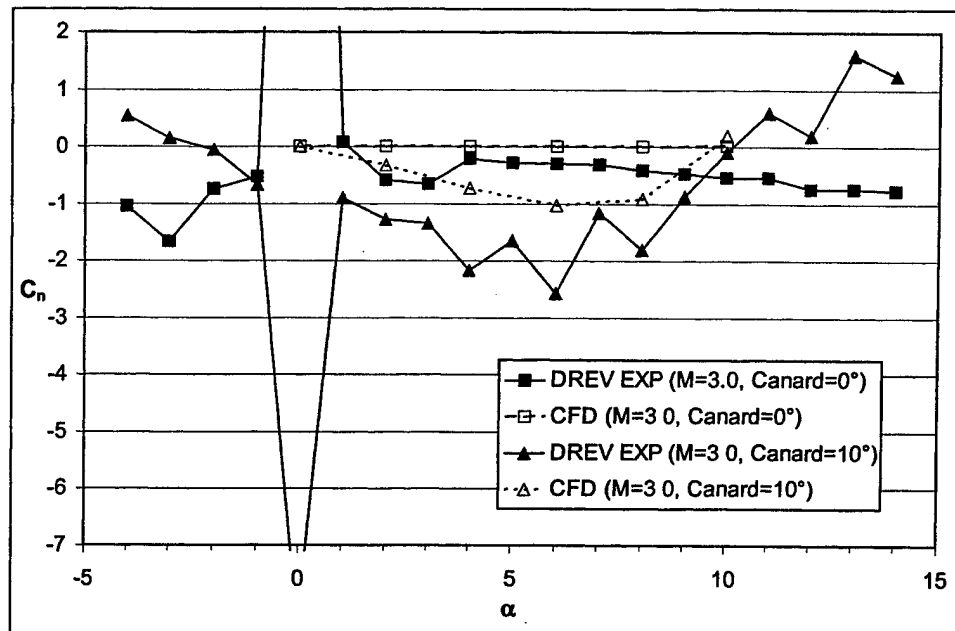


Figure B-14. Yawning moment for grid fin case at Mach 3.0.

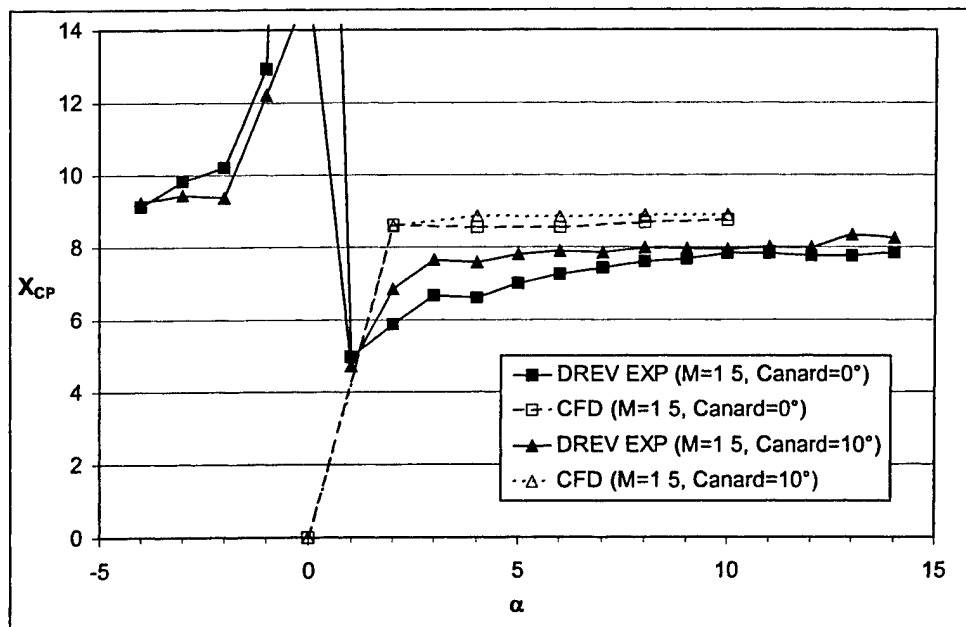


Figure B-15. Center of pressure location from nose for grid fin case at Mach 1.5.

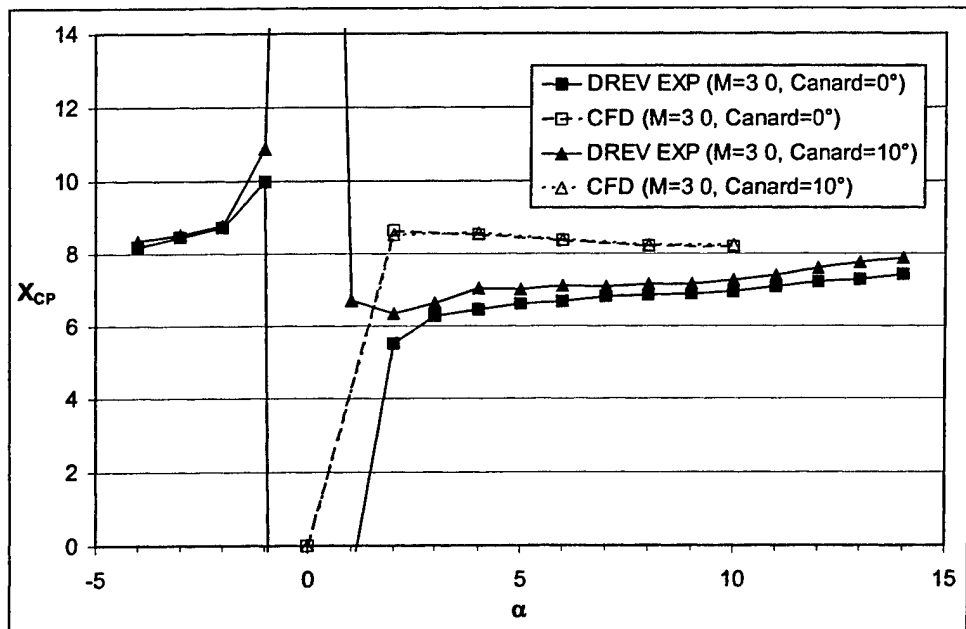


Figure B-16. Center of pressure location from nose for grid fin case at Mach 3.0.

Appendix C. Force Coefficients on Canards

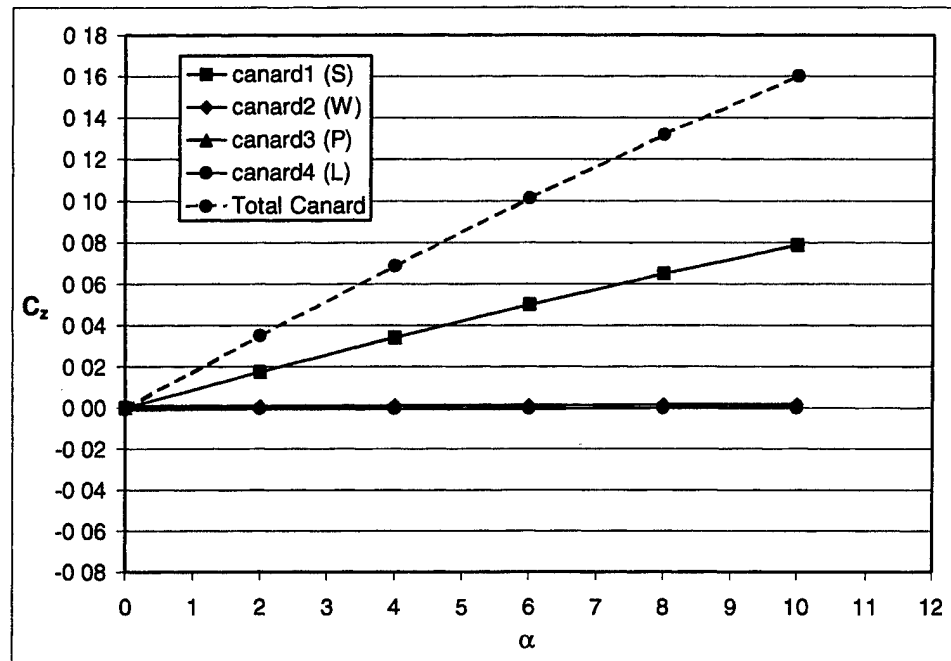


Figure C-1. Canard normal force, $\delta = 0^\circ$, Mach 1.5.

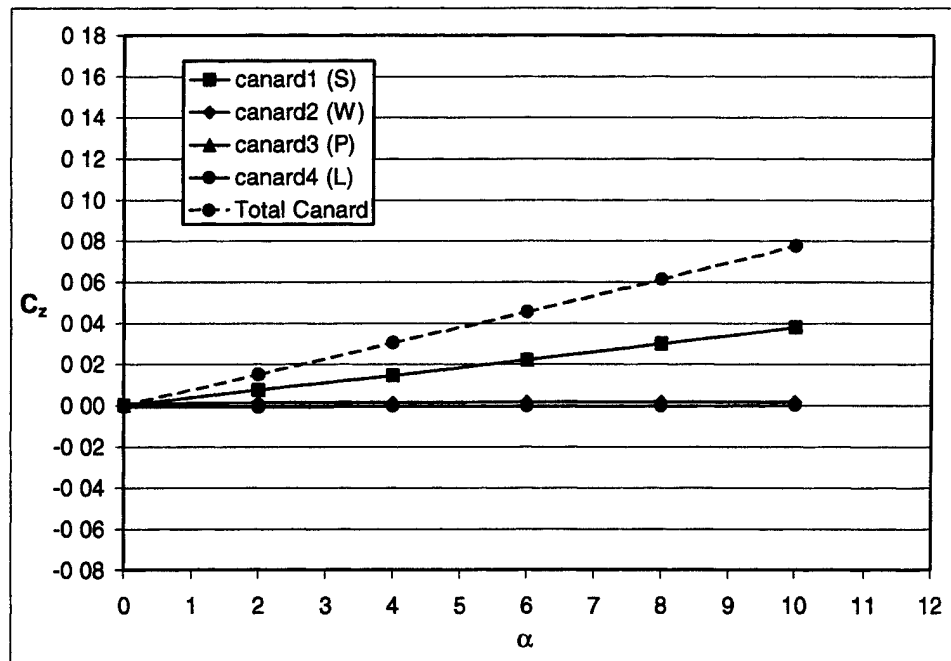


Figure C-2. Canard normal force, $\delta = 0^\circ$, Mach 3.0.

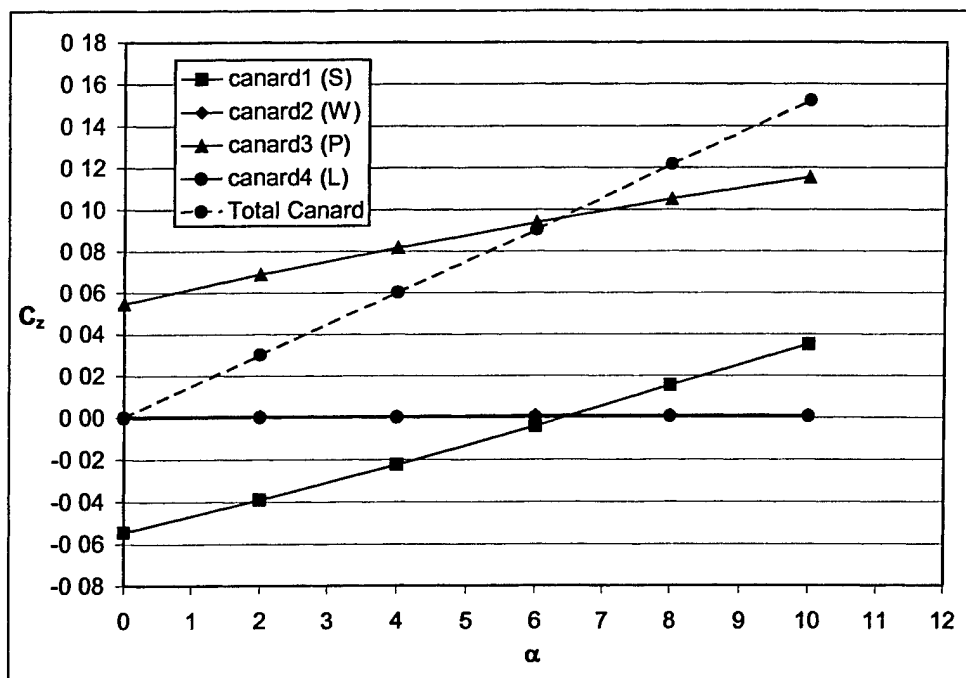


Figure C-3. Canard normal force, $\delta = 10^\circ$, Mach 1.5.

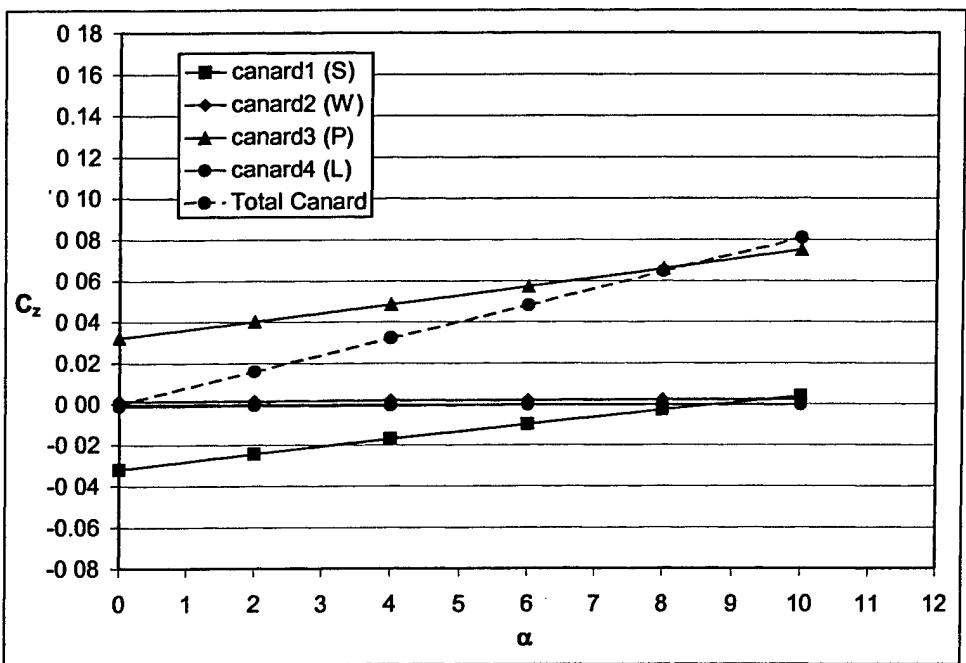


Figure C-4. Canard normal force, $\delta = 10^\circ$, Mach 3.0.

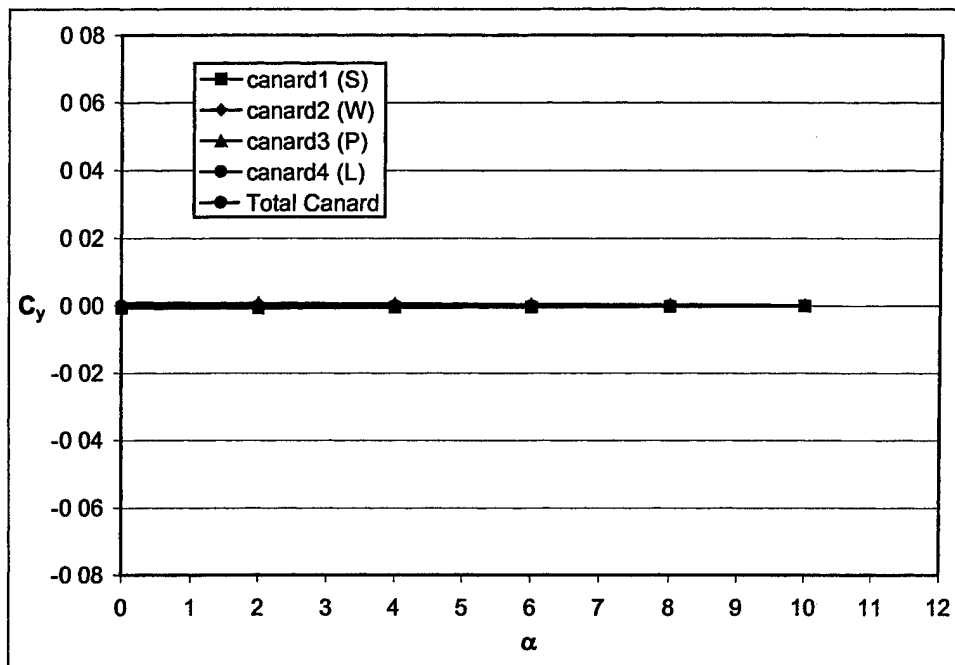


Figure C-5. Canard side force, $\delta = 0^\circ$, Mach 1.5.

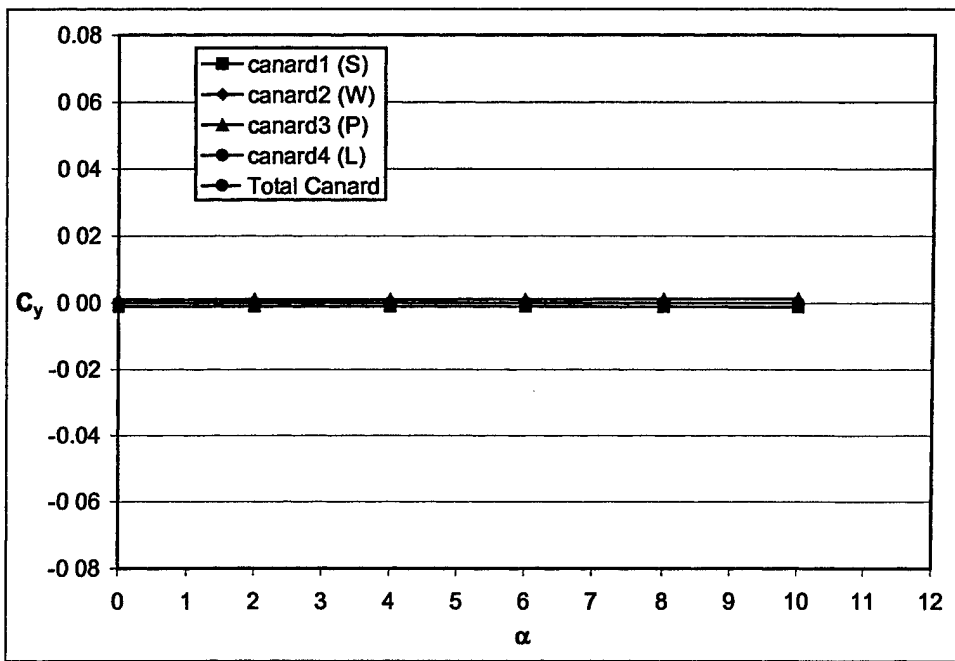


Figure C-6. Canard side force, $\delta = 0^\circ$, Mach 3.0.

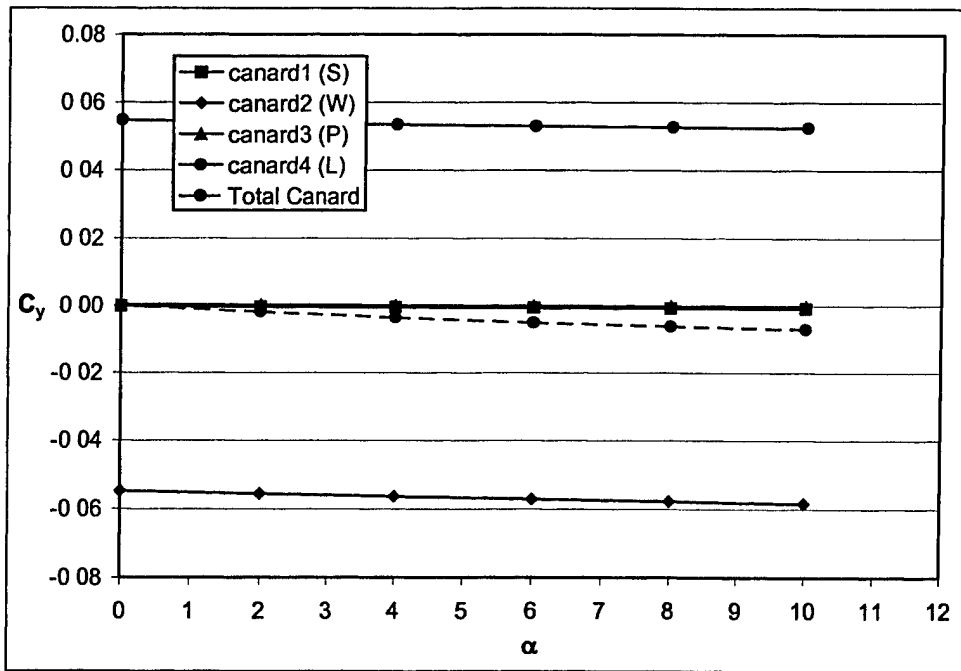


Figure C-7. Canard side force, $\delta = 10^\circ$, Mach 1.5.

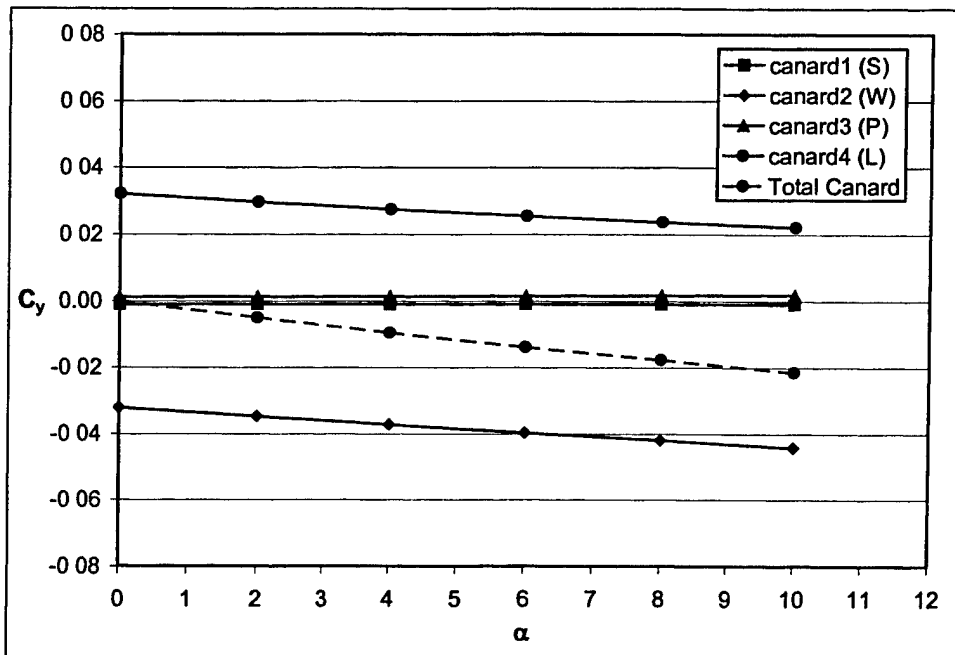


Figure C-8. Canard side force, $\delta = 10^\circ$, Mach 3.0.

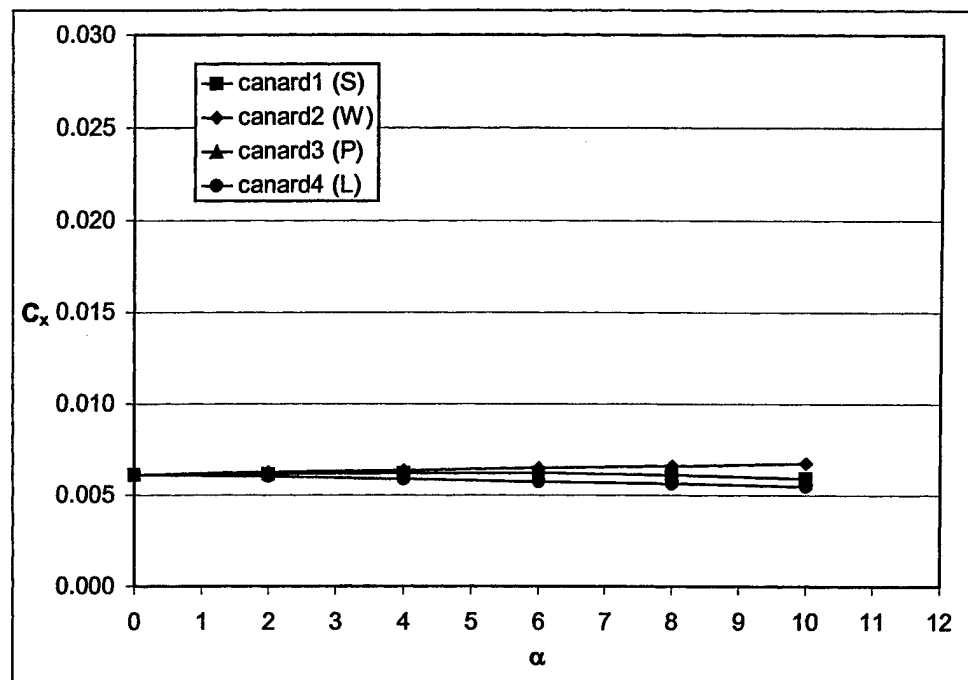


Figure C-9. Canard axial force, $\delta = 0^\circ$, Mach 1.5.

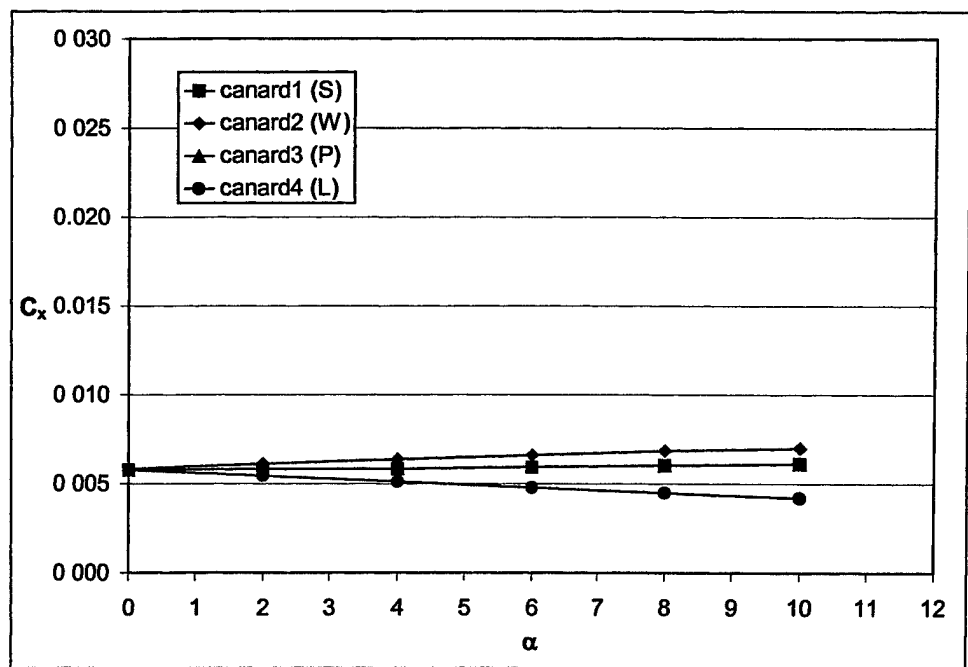


Figure C-10. Canard axial force, $\delta = 0^\circ$, Mach 3.0.

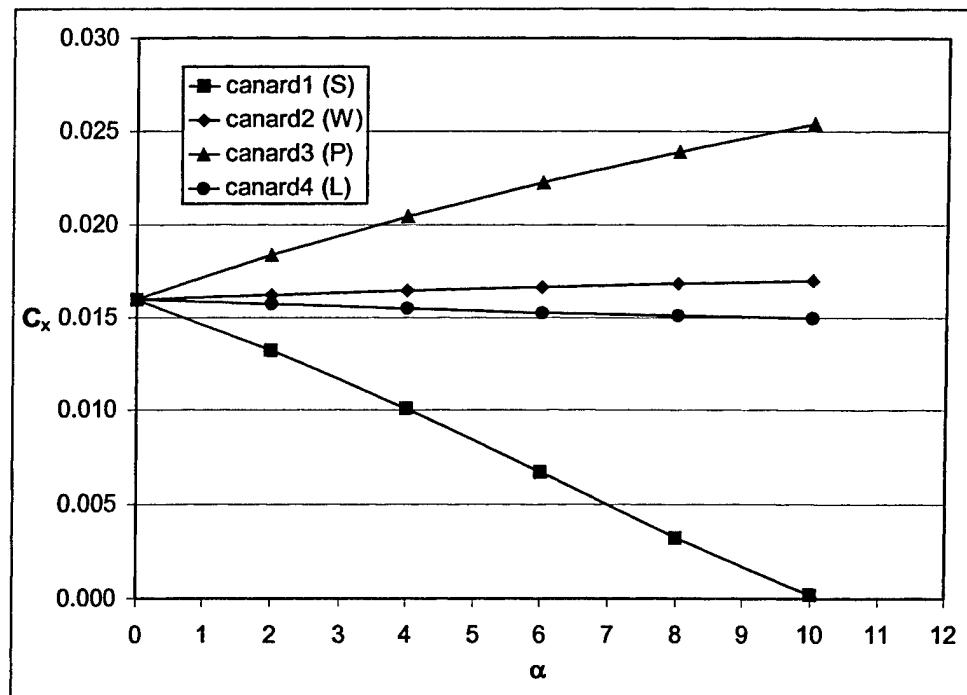


Figure C-11. Canard axial force, $\delta = 10^\circ$, Mach 1.5.

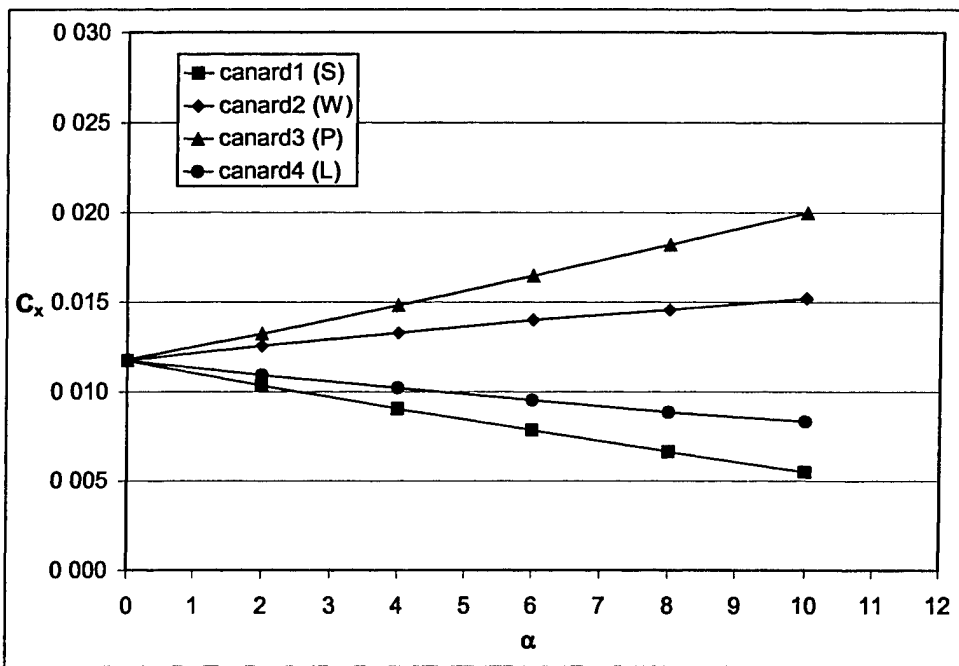


Figure C-12. Canard axial force, $\delta = 10^\circ$, Mach 3.0.

Table C-1. Aerodynamic coefficients on canards, planar fin case, $\delta = 0^\circ$, Mach 1.5.

α	0	2	4	6	8	10
Axial Force						
Canard1 (S)	0.0061	0.0062	0.0062	0.0062	0.0061	0.0059
Canard2 (W)	0.0061	0.0062	0.0064	0.0065	0.0066	0.0067
Canard3 (P)	0.0061	0.0062	0.0062	0.0062	0.0061	0.0059
Canard4 (L)	0.0061	0.0060	0.0059	0.0058	0.0056	0.0055
Total canard	0.0245	0.0246	0.0247	0.0246	0.0244	0.0241
Side Force						
Canard1 (S)	-0.0007	-0.0007	-0.0006	-0.0004	-0.0002	-0.0001
Canard2 (W)	0.0000	0.0000	0.0000	0.0000	0.0000	0.0000
Canard3 (P)	0.0007	0.0007	0.0006	0.0004	0.0002	0.0001
Canard4 (L)	0.0000	0.0000	0.0000	0.0000	0.0000	0.0000
Total canard	0.0000	0.0000	0.0000	0.0000	0.0000	0.0000
Normal Force						
Canard1 (S)	0.0000	0.0173	0.0341	0.0501	0.0650	0.0790
Canard2 (W)	0.0007	0.0009	0.0011	0.0014	0.0016	0.0019
Canard3 (P)	0.0000	0.0173	0.0341	0.0501	0.0650	0.0789
Canard4 (L)	-0.0007	-0.0006	-0.0004	-0.0002	-0.0001	0.0001
Total canard	0.0000	0.0350	0.0689	0.1013	0.1316	0.1598

S = starboard; W = windward; P = port; L = leeward.

Table C-2. Aerodynamic coefficients on canards, planar fin case, $\delta = 10^\circ$, Mach 1.5.

α	0	2	4	6	8	10
Axial Force						
Canard1 (S)	0.0159	0.0132	0.0101	0.0067	0.0032	0.0002
Canard2 (W)	0.0159	0.0162	0.0164	0.0166	0.0168	0.0169
Canard3 (P)	0.0159	0.0183	0.0204	0.0222	0.0239	0.0254
Canard4 (L)	0.0159	0.0157	0.0154	0.0152	0.0151	0.0149
Total canard	0.0637	0.0634	0.0623	0.0608	0.0590	0.0574
Side Force						
Canard1 (S)	-0.0002	-0.0004	-0.0006	-0.0007	-0.0009	-0.0009
Canard2 (W)	-0.0548	-0.0556	-0.0564	-0.0572	-0.0578	-0.0584
Canard3 (P)	0.0002	0.0001	-0.0001	-0.0002	-0.0002	-0.0003
Canard4 (L)	0.0548	0.0540	0.0534	0.0530	0.0527	0.0525
Total canard	0.0000	-0.0019	-0.0036	-0.0051	-0.0062	-0.0071
Normal Force						
Canard1 (S)	-0.0548	-0.0393	-0.0224	-0.0041	0.0155	0.0350
Canard2 (W)	0.0002	0.0004	0.0005	0.0007	0.0009	0.0010
Canard3 (P)	0.0548	0.0689	0.0818	0.0937	0.1049	0.1155
Canard4 (L)	-0.0002	-0.0001	0.0000	0.0001	0.0002	0.0003
Total canard	0.0000	0.0298	0.0599	0.0904	0.1215	0.1519

S = starboard; W = windward; P = port; L = leeward

Table C-3. Aerodynamic coefficients on canards, planar fin case, $\delta = 0^\circ$, Mach 3.0.

α	0	2	4	6	8	10
Axial Force						
Canard1 (S)	0.0058	0.0058	0.0058	0.0059	0.0060	0.0061
Canard2 (W)	0.0058	0.0061	0.0064	0.0066	0.0068	0.0070
Canard3 (P)	0.0058	0.0058	0.0058	0.0059	0.0060	0.0061
Canard4 (L)	0.0058	0.0054	0.0051	0.0048	0.0045	0.0042
Total canard	0.0232	0.0231	0.0231	0.0232	0.0233	0.0234
Side Force						
Canard1 (S)	-0.0010	-0.0010	-0.0010	-0.0011	-0.0011	-0.0012
Canard2 (W)	0.0000	0.0000	0.0000	0.0000	0.0000	0.0000
Canard3 (P)	0.0010	0.0010	0.0010	0.0011	0.0011	0.0012
Canard4 (L)	0.0000	0.0000	0.0000	0.0000	0.0000	0.0000
Total canard	0.0000	0.0000	0.0000	0.0000	0.0000	0.0000
Normal Force						
Canard1 (S)	0.0000	0.0074	0.0148	0.0222	0.0299	0.0378
Canard2 (W)	0.0010	0.0012	0.0013	0.0015	0.0017	0.0018
Canard3 (P)	0.0000	0.0074	0.0148	0.0222	0.0299	0.0378
Canard4 (L)	-0.0010	-0.0008	-0.0006	-0.0004	-0.0003	-0.0001
Total canard	0.0000	0.0151	0.0303	0.0455	0.0612	0.0773

S = starboard; W = windward; P = port; L = leeward.

Table C-4. Aerodynamic coefficients on canards, planar fin case, $\delta = 10^\circ$, Mach 3.0.

α	0	2	4	6	8	10
Axial Force						
Canard1 (S)	0.0117	0.0104	0.0091	0.0078	0.0066	0.0055
Canard2 (W)	0.0117	0.0126	0.0133	0.0140	0.0146	0.0152
Canard3 (P)	0.0118	0.0132	0.0148	0.0164	0.0182	0.0200
Canard4 (L)	0.0117	0.0109	0.0102	0.0095	0.0089	0.0083
Total canard	0.0470	0.0471	0.0473	0.0477	0.0483	0.0489
Side Force						
Canard1 (S)	-0.0011	-0.0011	-0.0010	-0.0010	-0.0010	-0.0010
Canard2 (W)	-0.0321	-0.0347	-0.0372	-0.0397	-0.0420	-0.0443
Canard3 (P)	0.0011	0.0012	0.0013	0.0014	0.0016	0.0017
Canard4 (L)	0.0321	0.0296	0.0274	0.0254	0.0236	0.0220
Total canard	0.0000	-0.0050	-0.0096	-0.0139	-0.0178	-0.0215
Normal Force						
Canard1 (S)	-0.0321	-0.0244	-0.0171	-0.0100	-0.0030	0.0039
Canard2 (W)	0.0011	0.0013	0.0015	0.0017	0.0019	0.0021
Canard3 (P)	0.0321	0.0400	0.0484	0.0569	0.0659	0.0750
Canard4 (L)	-0.0011	-0.0009	-0.0007	-0.0005	-0.0004	-0.0002
Total canard	0.0000	0.0160	0.0320	0.0481	0.0644	0.0807

S = starboard; W = windward; P = port; L = leeward.

Appendix D. Force Coefficients on Planar Fins

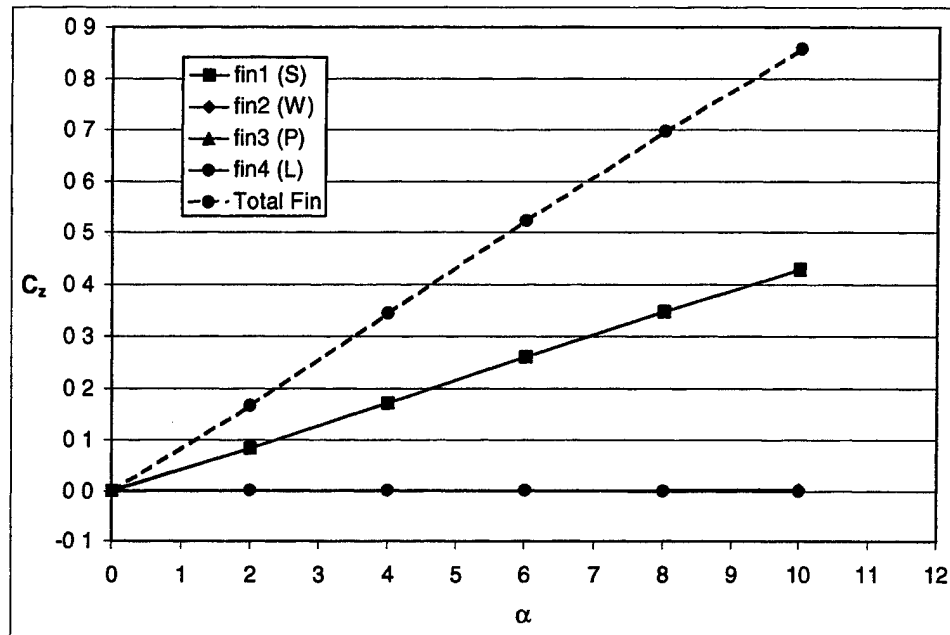


Figure D-1. Planar fin normal force, $\delta = 0^\circ$, Mach 1.5.

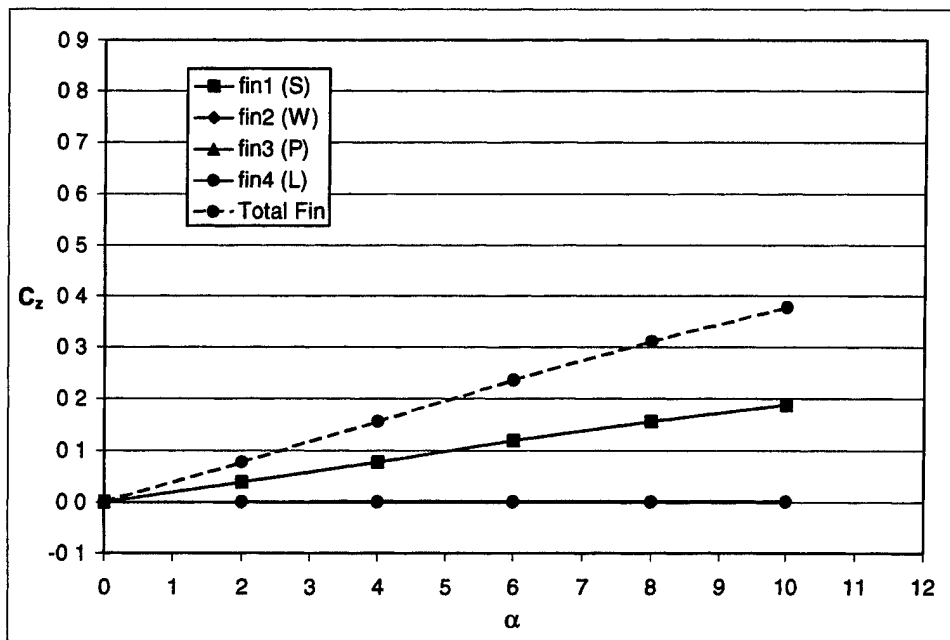


Figure D-2. Planar fin normal force, $\delta = 0^\circ$, Mach 3.0.

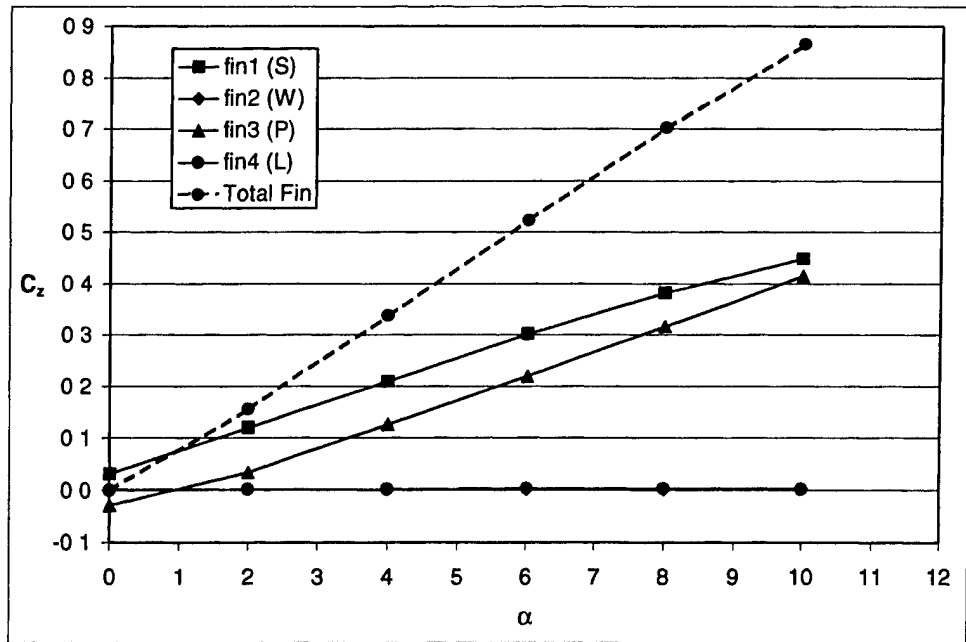


Figure D-3 Planar fin normal force, $\delta = 10^\circ$, Mach 1.5.

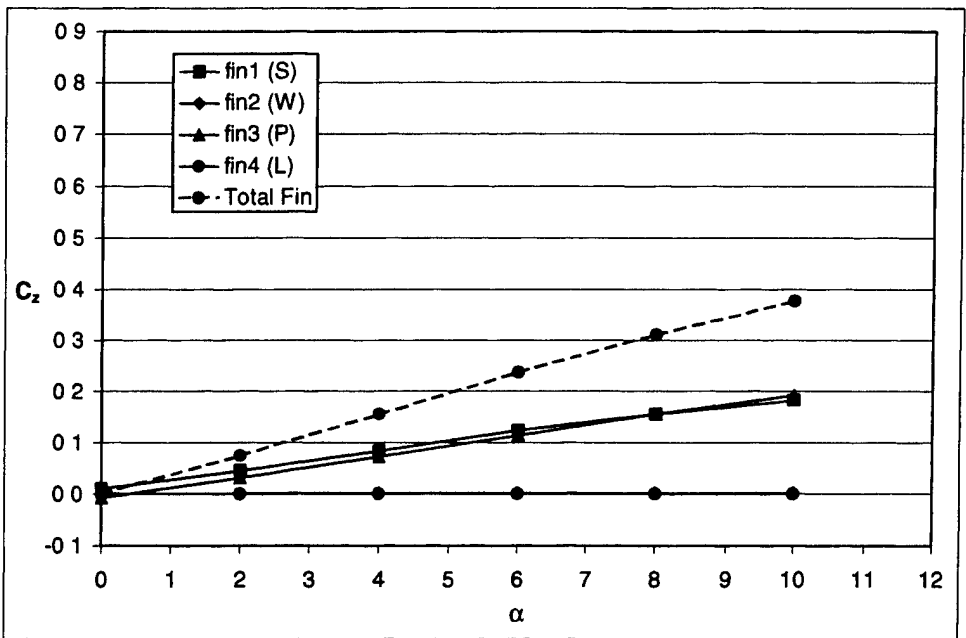


Figure D-4. Planar fin normal force, $\delta = 10^\circ$, Mach 3.0

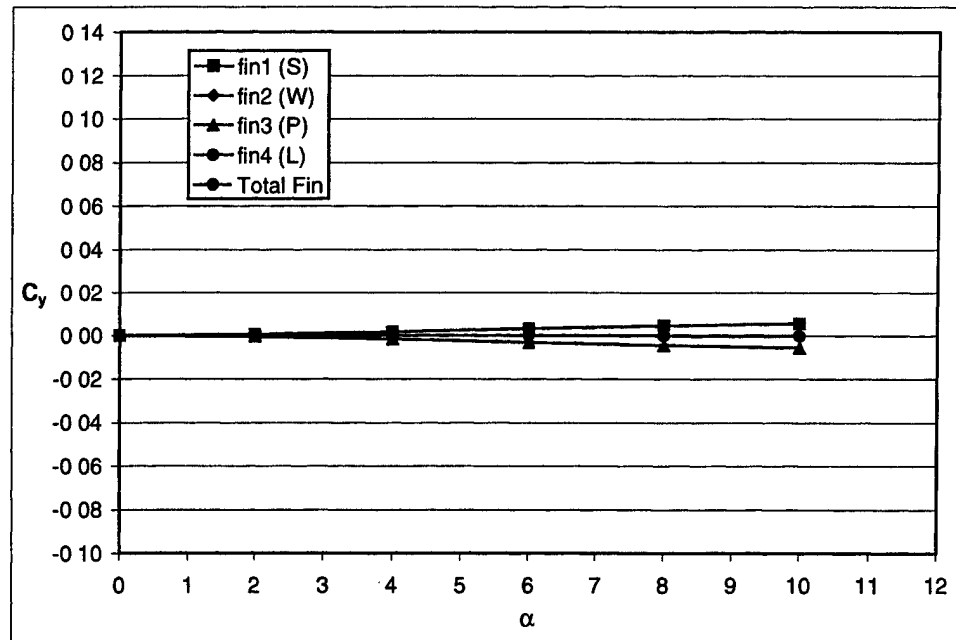


Figure D-5. Planar fin side force, $\delta = 0^\circ$, Mach 1.5.

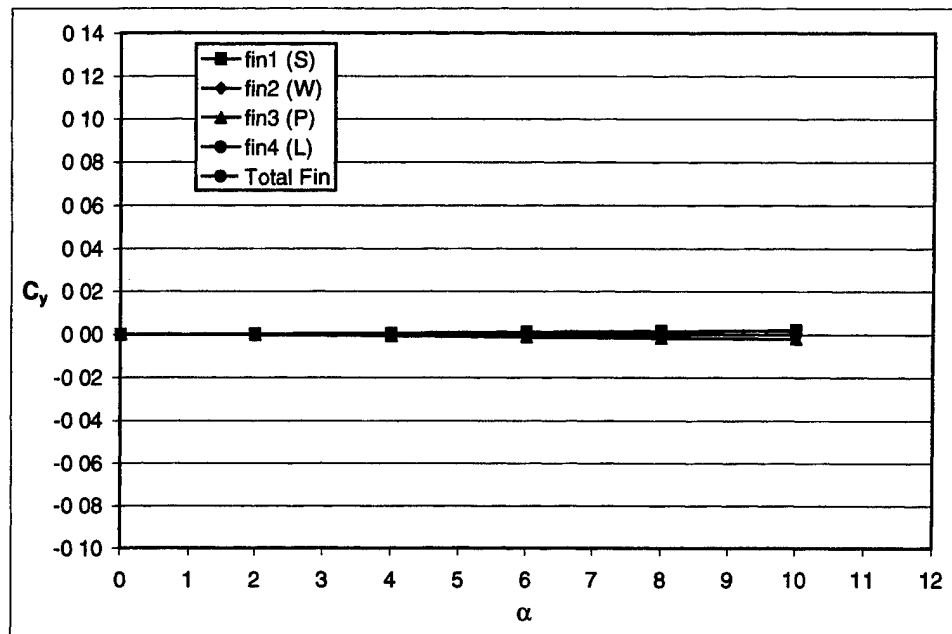


Figure D-6. Planar fin side force, $\delta = 0^\circ$, Mach 3.0.

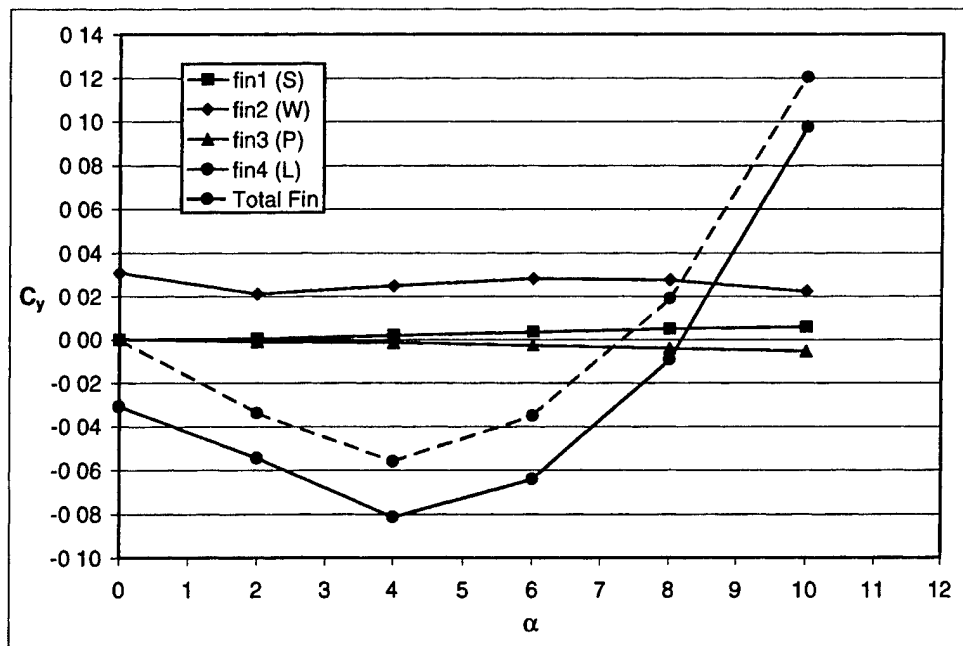


Figure D-7. Planar fin side force, $\delta = 10^\circ$, Mach 1.5.

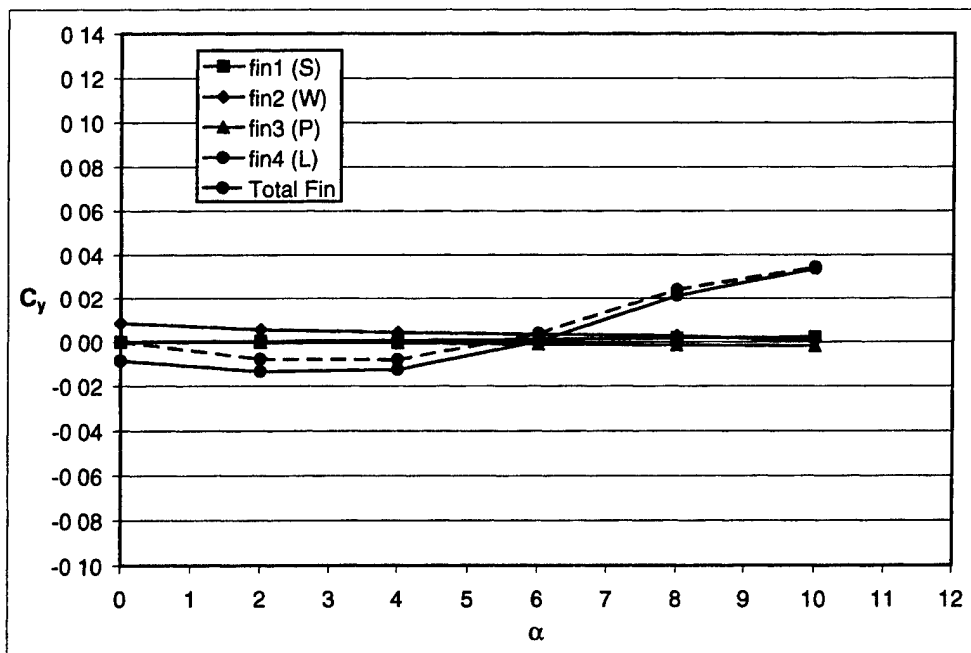


Figure D-8 Planar fin side force, $\delta = 10^\circ$, Mach 3.0

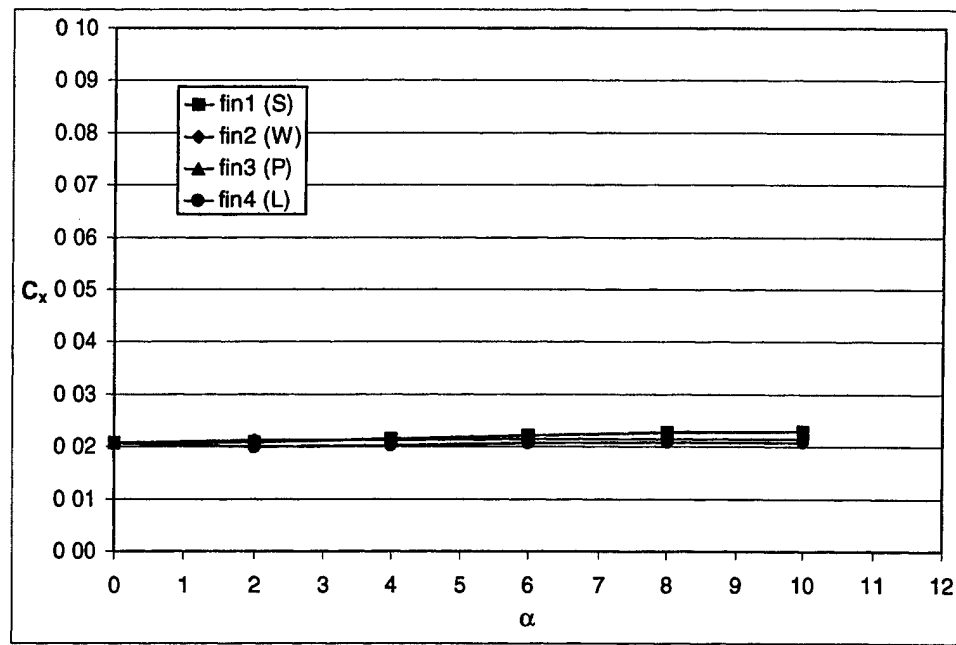


Figure D-9. Planar fin axial force, $\delta = 0^\circ$, Mach 1.5.

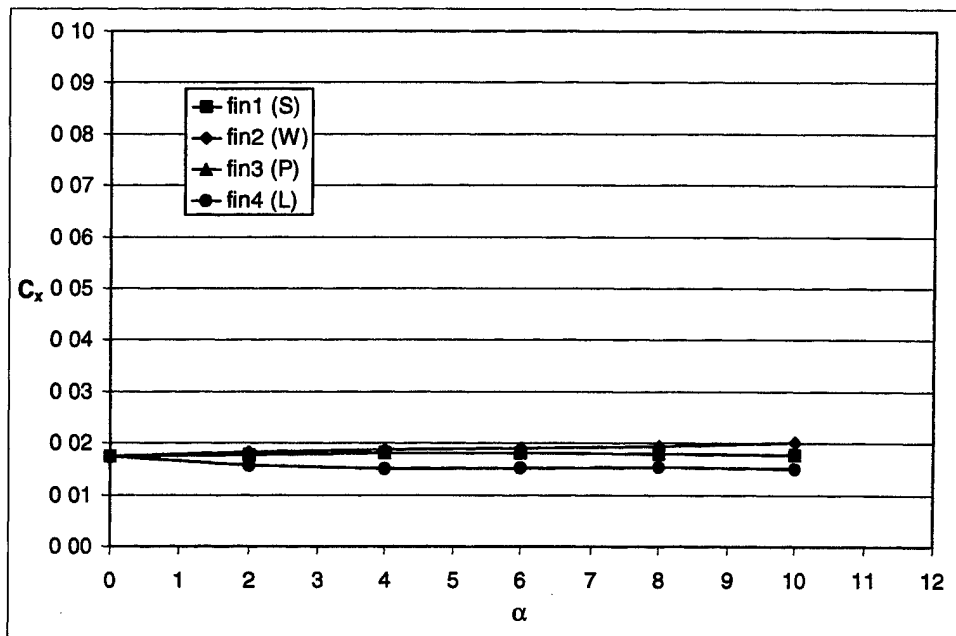


Figure D-10. Planar fin axial force, $\delta = 0^\circ$, Mach 3.0.

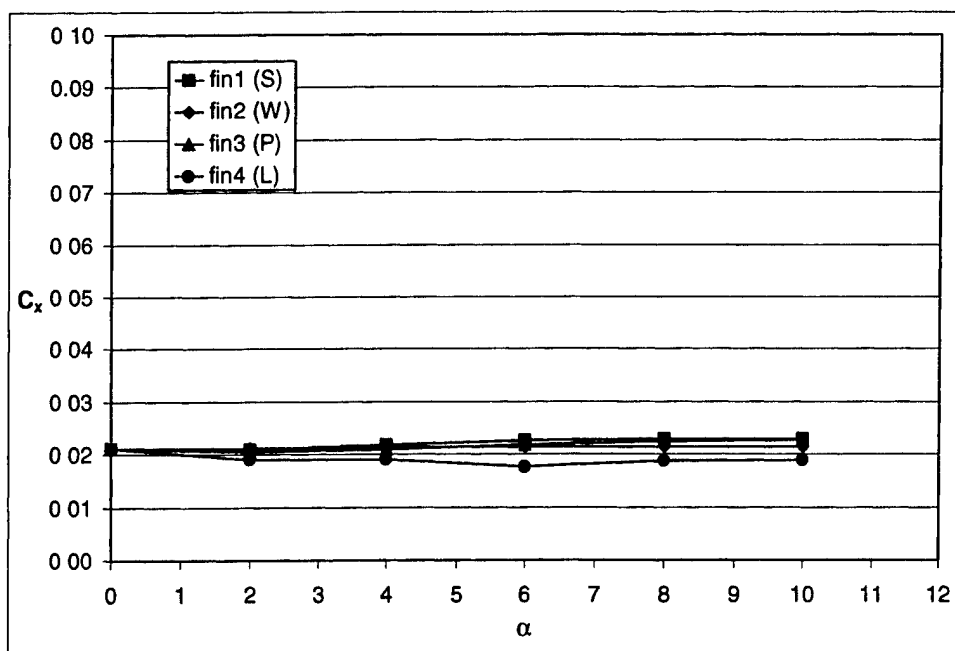


Figure D-11. Planar fin axial force, $\delta = 10^\circ$, Mach 1.5.

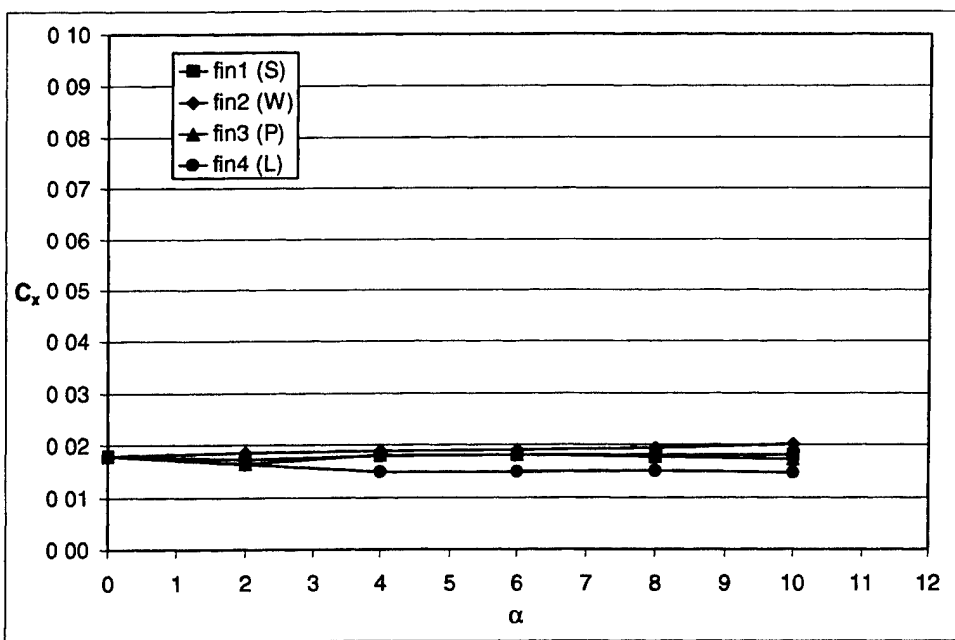


Figure D-12. Planar fin axial force, $\delta = 10^\circ$, Mach 3.0.

Table D-1. Aerodynamic coefficients on planar fins, $\delta = 0^\circ$, Mach 1.5.

α	0	2	4	6	8	10
Axial Force						
Fin1 (S)	0.0207	0.0208	0.0214	0.0221	0.0227	0.0229
Fin2 (W)	0.0207	0.0211	0.0213	0.0215	0.0215	0.0214
Fin3 (P)	0.0207	0.0208	0.0215	0.0221	0.0227	0.0229
Fin4 (L)	0.0207	0.0199	0.0202	0.0206	0.0208	0.0208
Total fin	0.0826	0.0828	0.0844	0.0864	0.0878	0.0880
Side Force						
Fin1 (S)	0.0000	0.0005	0.0017	0.0032	0.0046	0.0057
Fin2 (W)	0.0000	0.0000	0.0000	0.0000	0.0000	0.0000
Fin3 (P)	0.0000	-0.0005	-0.0017	-0.0032	-0.0046	-0.0057
Fin4 (L)	0.0000	0.0000	0.0000	-0.0001	-0.0001	-0.0002
Total fin	0.0000	0.0000	0.0000	-0.0001	-0.0001	-0.0002
Normal Force						
Fin1 (S)	0.0000	0.0832	0.1712	0.2608	0.3478	0.4279
Fin2 (W)	0.0000	0.0004	0.0007	0.0011	0.0015	0.0019
Fin3 (P)	0.0000	0.0832	0.1712	0.2608	0.3479	0.4281
Fin4 (L)	0.0000	0.0002	0.0002	0.0001	-0.0001	-0.0005
Total fin	0.0000	0.1670	0.3433	0.5228	0.6972	0.8575

S = starboard; W = windward; P = port; L = leeward.

Table D-2. Aerodynamic coefficients on planar fins, $\delta = 10^\circ$, Mach 1.5.

α	0	2	4	6	8	10
Axial Force						
Fin1 (S)	0.0212	0.0210	0.0218	0.0225	0.0230	0.0229
Fin2 (W)	0.0211	0.0212	0.0214	0.0215	0.0215	0.0214
Fin3 (P)	0.0211	0.0205	0.0210	0.0218	0.0224	0.0227
Fin4 (L)	0.0212	0.0191	0.0191	0.0176	0.0188	0.0189
Total fin	0.0846	0.0818	0.0833	0.0834	0.0857	0.0859
Side Force						
Fin1 (S)	-0.0001	0.0005	0.0019	0.0036	0.0049	0.0058
Fin2 (W)	0.0308	0.0211	0.0248	0.0282	0.0276	0.0224
Fin3 (P)	0.0001	-0.0009	-0.0014	-0.0027	-0.0041	-0.0054
Fin4 (L)	-0.0308	-0.0544	-0.0813	-0.0641	-0.0093	0.0975
Total fin	0.0000	-0.0338	-0.0560	-0.0351	0.0191	0.1203
Normal Force						
Fin1 (S)	0.0308	0.1203	0.2096	0.3017	0.3816	0.4475
Fin2 (W)	0.0001	0.0003	0.0007	0.0011	0.0015	0.0019
Fin3 (P)	-0.0308	0.0341	0.1258	0.2182	0.3158	0.4132
Fin4 (L)	-0.0001	0.0002	0.0007	0.0019	0.0025	0.0015
Total fin	0.0000	0.1550	0.3369	0.5230	0.7014	0.8641

S = starboard; W = windward; P = port; L = leeward

Table D-3. Aerodynamic coefficients on planar fins, $\delta = 0^\circ$, Mach 3.0.

α	0	2	4	6	8	10
Axial Force						
Fin1 (S)	0.0174	0.0177	0.0181	0.0181	0.0179	0.0177
Fin2 (W)	0.0174	0.0183	0.0187	0.0190	0.0194	0.0202
Fin3 (P)	0.0174	0.0177	0.0181	0.0181	0.0179	0.0177
Fin4 (L)	0.0174	0.0158	0.0150	0.0152	0.0154	0.0150
Total fin	0.0697	0.0695	0.0699	0.0706	0.0706	0.0706
Side Force						
Fin1 (S)	0.0000	0.0001	0.0006	0.0011	0.0016	0.0020
Fin2 (W)	0.0000	0.0000	0.0000	0.0000	0.0000	0.0000
Fin3 (P)	0.0000	-0.0001	-0.0006	-0.0011	-0.0016	-0.0020
Fin4 (L)	0.0000	0.0000	0.0000	0.0000	0.0000	-0.0001
Total fin	0.0000	0.0000	0.0000	0.0000	0.0000	0.0000
Normal Force						
Fin1 (S)	0.0000	0.0382	0.0776	0.1179	0.1551	0.1881
Fin2 (W)	0.0000	0.0003	0.0007	0.0010	0.0014	0.0018
Fin3 (P)	0.0000	0.0382	0.0776	0.1179	0.1551	0.1881
Fin4 (L)	0.0000	0.0002	0.0002	0.0000	-0.0004	-0.0009
Total fin	0.0000	0.0769	0.1560	0.2368	0.3111	0.3771

S = starboard; W = windward; P = port; L = leeward

Table D-4. Aerodynamic coefficients on planar fins, $\delta = 10^\circ$, Mach 3.0.

α	0	2	4	6	8	10
Axial Force						
Fin1 (S)	0.0180	0.0173	0.0179	0.0181	0.0181	0.0181
Fin2 (W)	0.0180	0.0186	0.0188	0.0191	0.0194	0.0202
Fin3 (P)	0.0180	0.0165	0.0181	0.0182	0.0178	0.0173
Fin4 (L)	0.0180	0.0163	0.0148	0.0150	0.0151	0.0148
Total fin	0.0720	0.0687	0.0696	0.0703	0.0704	0.0704
Side Force						
Fin1 (S)	-0.0001	0.0001	0.0006	0.0011	0.0016	0.0020
Fin2 (W)	0.0086	0.0056	0.0043	0.0035	0.0027	0.0005
Fin3 (P)	0.0001	-0.0002	-0.0006	-0.0010	-0.0015	-0.0019
Fin4 (L)	-0.0086	-0.0135	-0.0126	0.0002	0.0210	0.0336
Total fin	0.0000	-0.0080	-0.0082	0.0038	0.0239	0.0342
Normal Force						
Fin1 (S)	0.0086	0.0443	0.0838	0.1230	0.1556	0.1828
Fin2 (W)	0.0001	0.0004	0.0007	0.0010	0.0014	0.0018
Fin3 (P)	-0.0086	0.0294	0.0713	0.1141	0.1551	0.1930
Fin4 (L)	-0.0001	0.0001	0.0003	0.0003	-0.0002	-0.0006
Total fin	0.0000	0.0742	0.1561	0.2384	0.3119	0.3770

S = starboard; W = windward; P = port; L = leeward.

Appendix E. Force Coefficients on Grid Fins

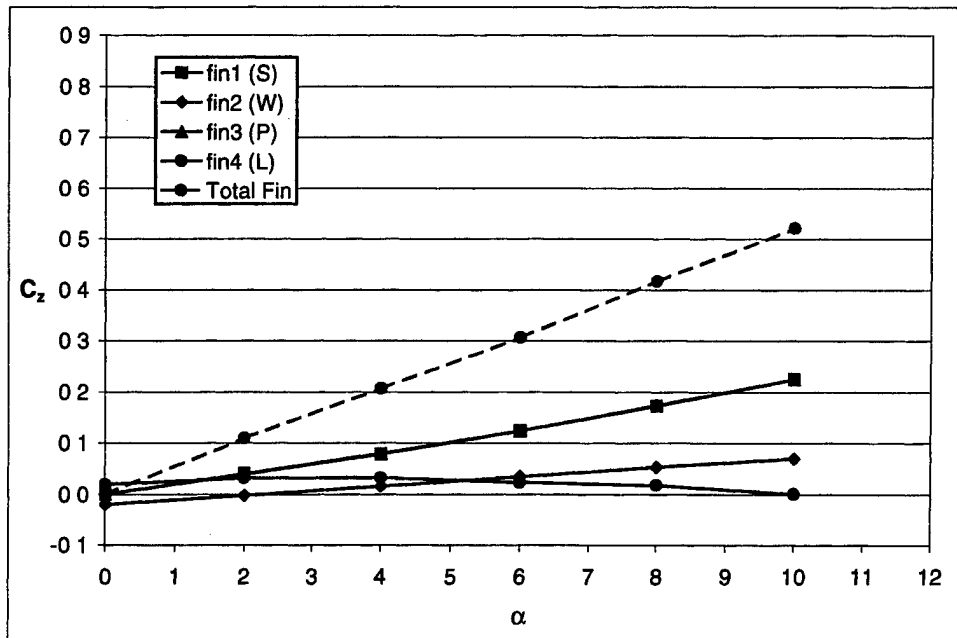


Figure E-1. Grid fin normal force, $\delta = 0^\circ$, Mach 1.5.

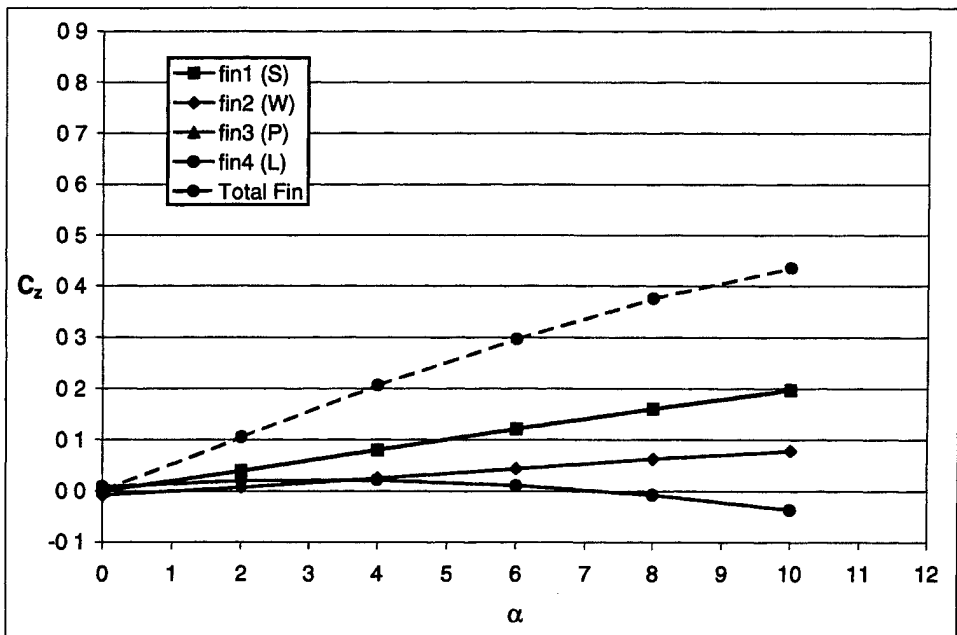


Figure E-2. Grid fin normal force, $\delta = 0^\circ$, Mach 3.0.

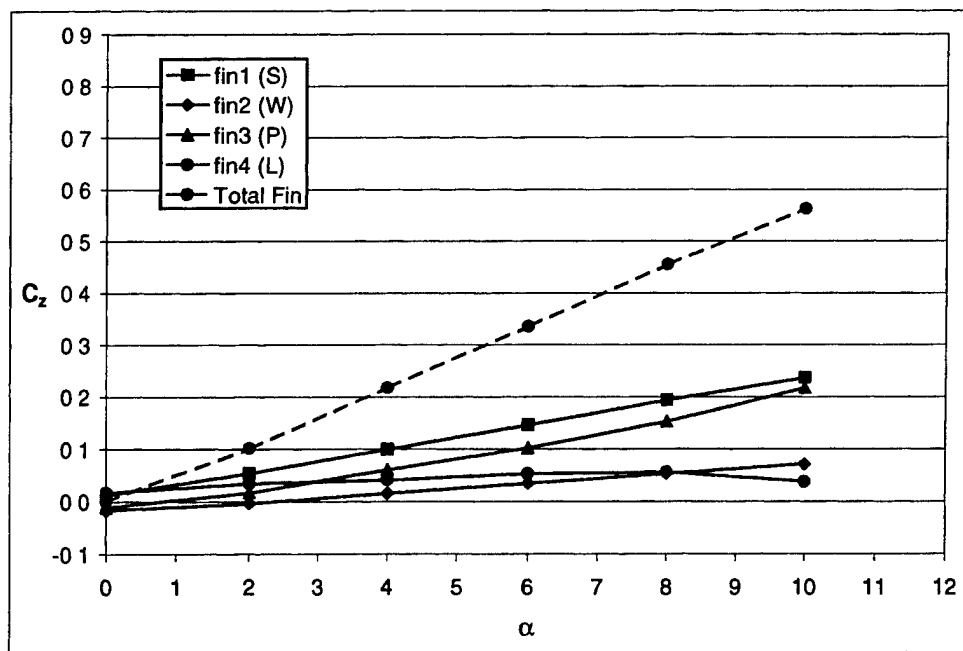


Figure E-3. Grid fin normal force, $\delta = 10^\circ$, Mach 1.5.

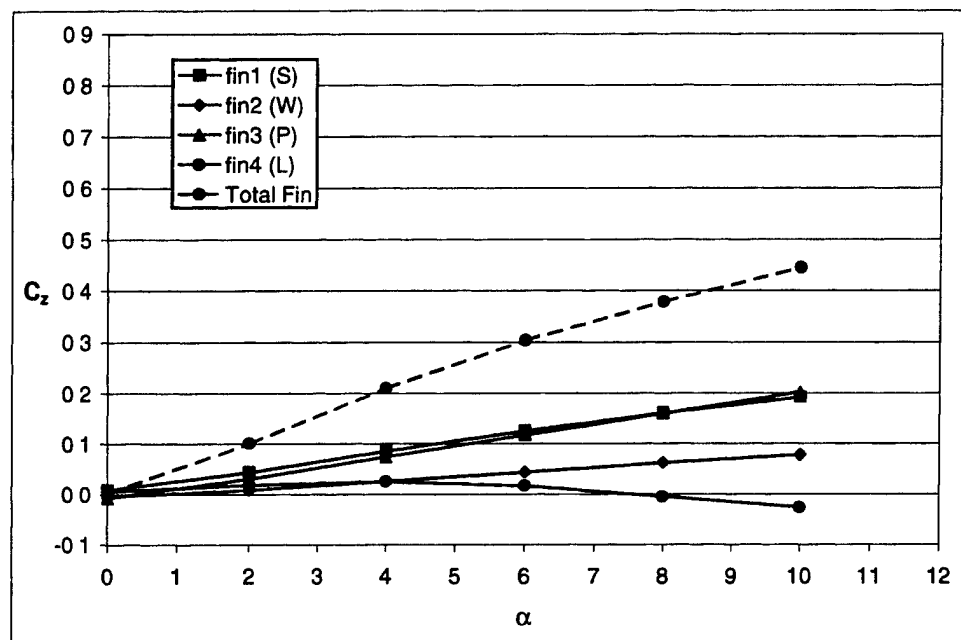


Figure E-4. Grid fin normal force, $\delta = 10^\circ$, Mach 3.0

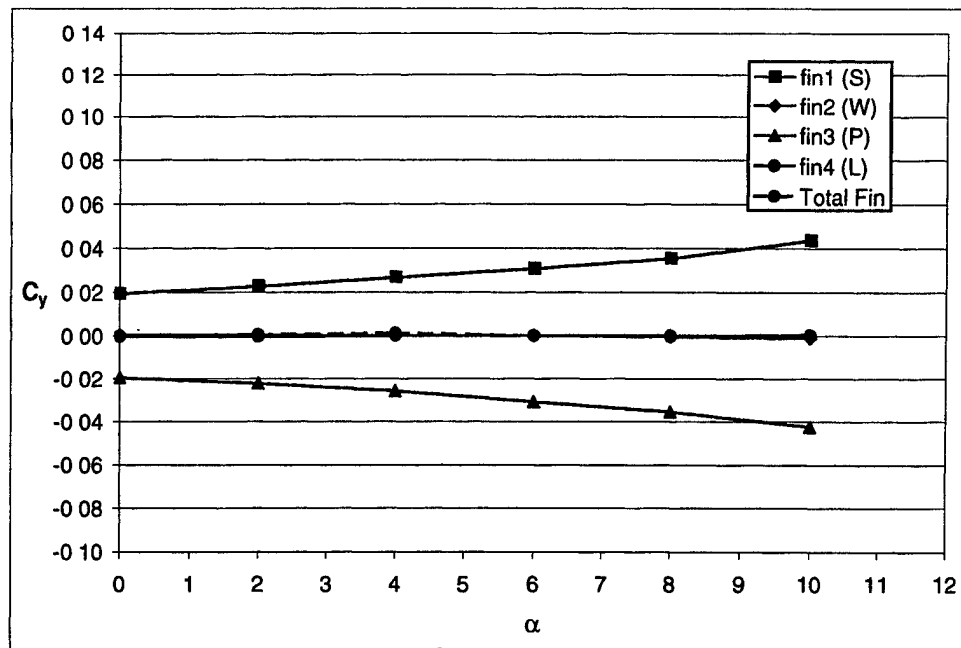


Figure E-5. Grid fin side force, $\delta = 0^\circ$, Mach 1.5.

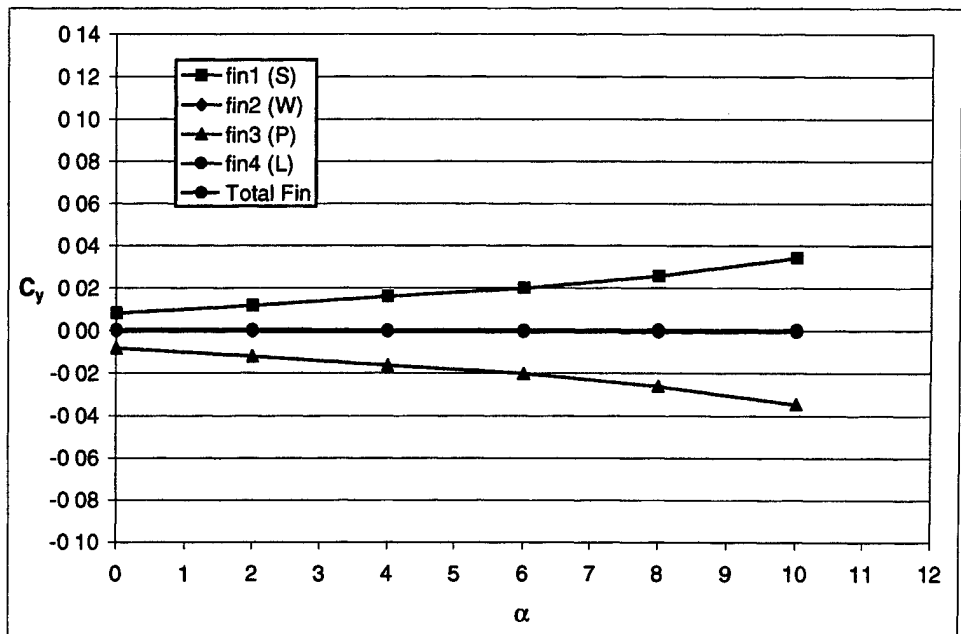


Figure E-6. Grid fin side force, $\delta = 0^\circ$, Mach 3.0

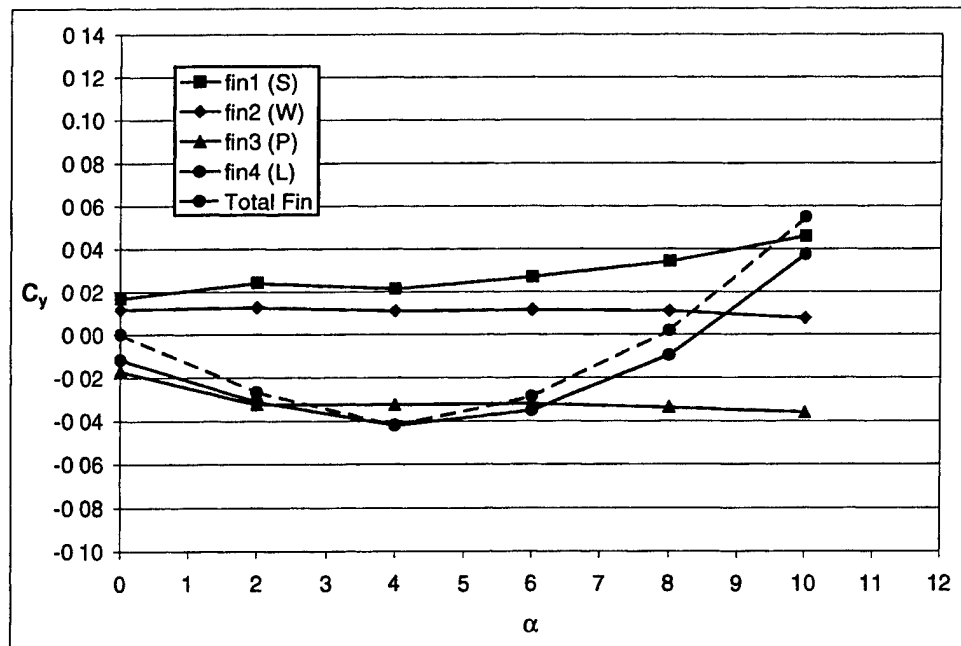


Figure E-7. Grid fin side force, $\delta = 10^\circ$, Mach 1.5

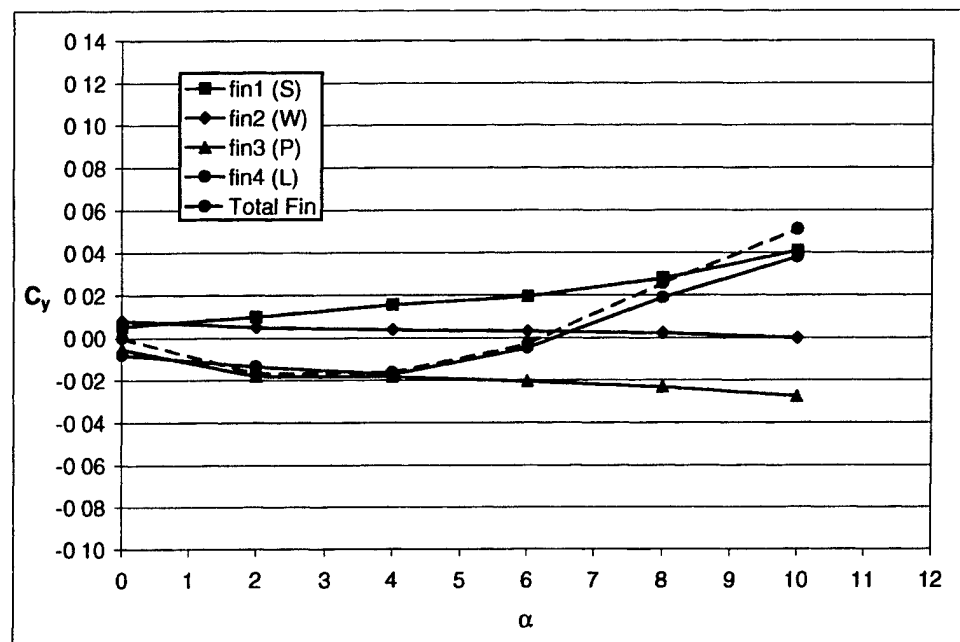


Figure E-8. Grid fin side force, $\delta = 10^\circ$, Mach 3.0.

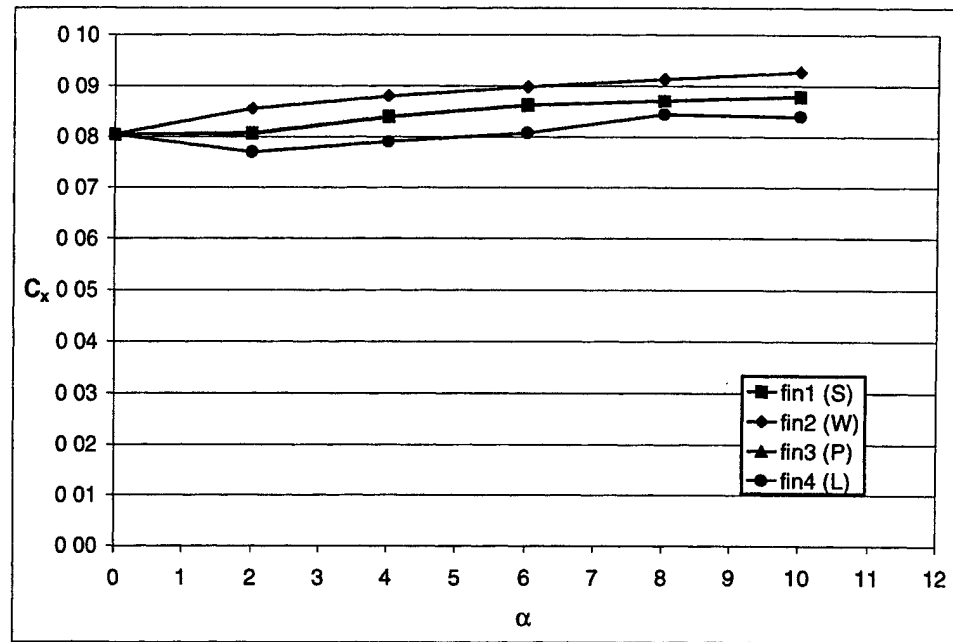


Figure E-9. Grid fin axial force, $\delta = 0^\circ$, Mach 1.5.

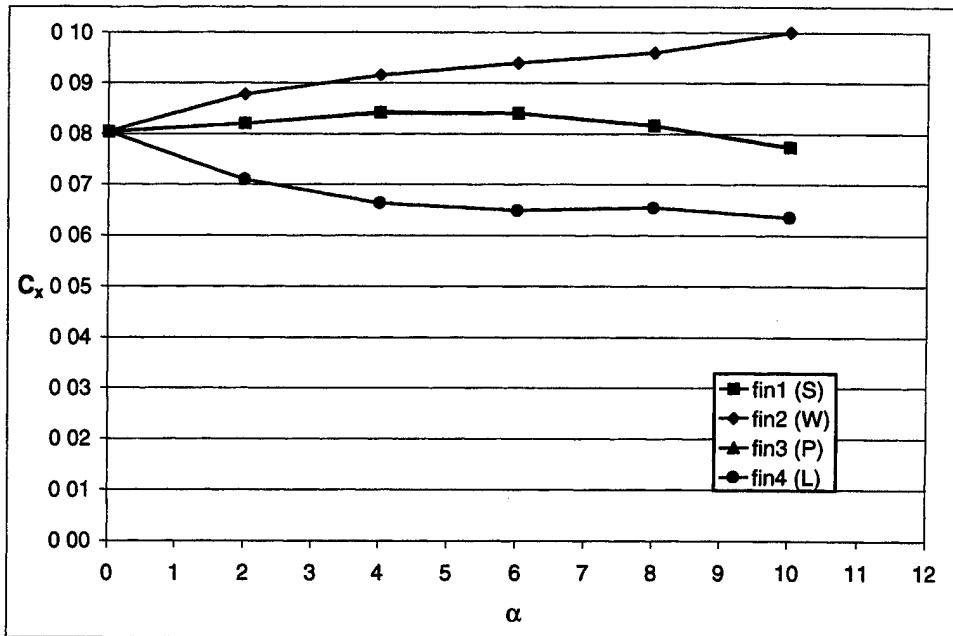


Figure E-10. Grid fin axial force, $\delta = 0^\circ$, Mach 3.0.

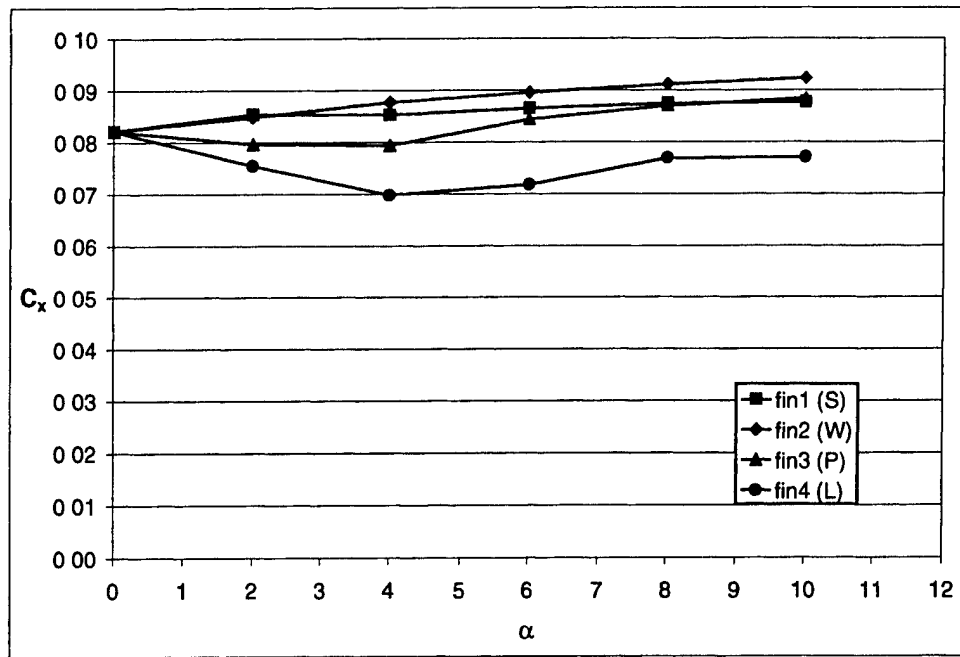


Figure E-11. Grid fin axial force, $\delta = 10^\circ$, Mach 1.5

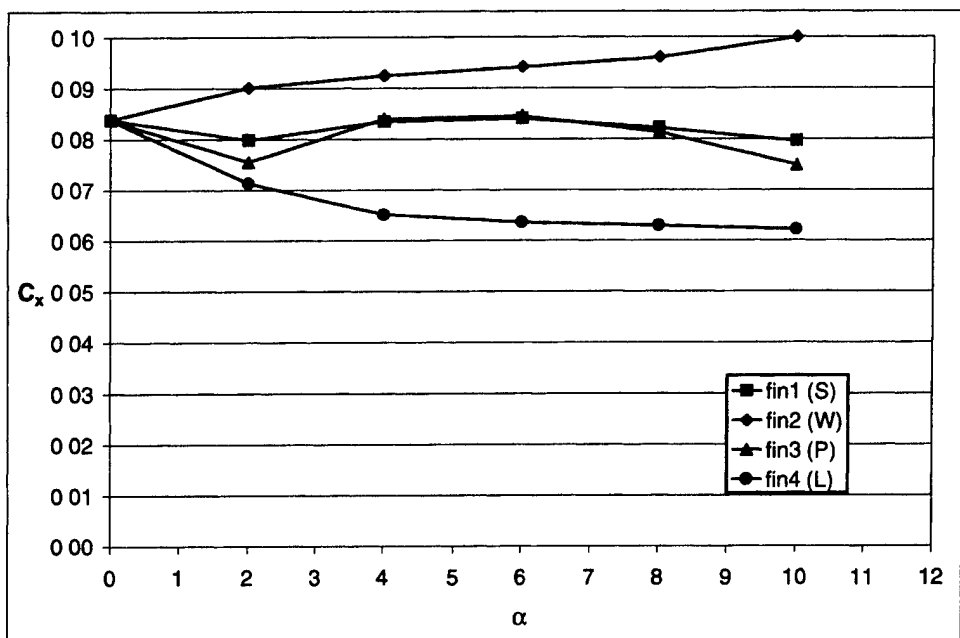


Figure E-12. Grid fin axial force, $\delta = 10^\circ$, Mach 3.0.

Table E-1. Aerodynamic coefficients on grid fins, $\delta = 0^\circ$, Mach 1.5.

α	0	2	4	6	8	10
Axial Force						
Fin1 (S)	0.0804	0.0807	0.0839	0.0863	0.0870	0.0879
Fin2 (W)	0.0804	0.0854	0.0880	0.0898	0.0913	0.0928
Fin3 (P)	0.0804	0.0805	0.0839	0.0862	0.0871	0.0878
Fin4 (L)	0.0804	0.0770	0.0790	0.0807	0.0844	0.0839
Total fin	0.3217	0.3237	0.3347	0.3430	0.3498	0.3524
Side Force						
Fin1 (S)	0.0195	0.0227	0.0268	0.0308	0.0355	0.0435
Fin2 (W)	0.0003	0.0004	0.0001	0.0000	-0.0004	-0.0011
Fin3 (P)	-0.0195	-0.0221	-0.0257	-0.0309	-0.0355	-0.0423
Fin4 (L)	-0.0004	-0.0004	0.0001	0.0002	0.0000	0.0003
Total fin	-0.0001	0.0005	0.0012	0.0001	-0.0003	0.0004
Normal Force						
Fin1 (S)	0.0003	0.0403	0.0794	0.1240	0.1728	0.2257
Fin2 (W)	-0.0195	-0.0021	0.0161	0.0349	0.0533	0.0702
Fin3 (P)	-0.0003	0.0396	0.0788	0.1239	0.1736	0.2251
Fin4 (L)	0.0194	0.0319	0.0326	0.0233	0.0177	0.0007
Total fin	-0.0001	0.1097	0.2069	0.3061	0.4174	0.5218

S = starboard; W = windward; P = port; L = leeward

Table E-2. Aerodynamic coefficients on grid fins, $\delta = 10^\circ$, Mach 1.5.

α	0	2	4	6	8	10
Axial Force						
Fin1 (S)	0.0821	0.0854	0.0853	0.0865	0.0875	0.0877
Fin2 (W)	0.0821	0.0848	0.0877	0.0896	0.0911	0.0923
Fin3 (P)	0.0821	0.0796	0.0794	0.0844	0.0870	0.0884
Fin4 (L)	0.0821	0.0754	0.0698	0.0717	0.0769	0.0770
Total fin	0.3284	0.3253	0.3221	0.3322	0.3425	0.3455
Side Force						
Fin1 (S)	0.0169	0.0242	0.0214	0.0270	0.0342	0.0458
Fin2 (W)	0.0117	0.0127	0.0110	0.0115	0.0110	0.0076
Fin3 (P)	-0.0169	-0.0324	-0.0326	-0.0321	-0.0338	-0.0361
Fin4 (L)	-0.0117	-0.0311	-0.0420	-0.0352	-0.0096	0.0374
Total fin	0.0001	-0.0267	-0.0422	-0.0288	0.0018	0.0547
Normal Force						
Fin1 (S)	0.0117	0.0539	0.0995	0.1459	0.1932	0.2364
Fin2 (W)	-0.0169	-0.0035	0.0157	0.0347	0.0534	0.0714
Fin3 (P)	-0.0116	0.0171	0.0606	0.1021	0.1529	0.2168
Fin4 (L)	0.0170	0.0340	0.0413	0.0531	0.0557	0.0378
Total fin	0.0001	0.1015	0.2171	0.3357	0.4550	0.5625

S = starboard; W = windward; P = port; L = leeward.

Table E-3. Aerodynamic coefficients on grid fins, $\delta = 0^\circ$, Mach 3.0.

α	0	2	4	6	8	10
Axial Force						
Fin1 (S)	0.0804	0.0820	0.0841	0.0840	0.0815	0.0773
Fin2 (W)	0.0804	0.0878	0.0916	0.0939	0.0960	0.1000
Fin3 (P)	0.0804	0.0821	0.0843	0.0841	0.0817	0.0774
Fin4 (L)	0.0805	0.0710	0.0663	0.0649	0.0654	0.0635
Total fin	0.3217	0.3228	0.3263	0.3269	0.3247	0.3183
Side Force						
Fin1 (S)	0.0082	0.0118	0.0160	0.0199	0.0257	0.0343
Fin2 (W)	-0.0005	-0.0005	-0.0005	-0.0005	-0.0006	-0.0006
Fin3 (P)	-0.0082	-0.0120	-0.0163	-0.0202	-0.0261	-0.0347
Fin4 (L)	0.0005	0.0005	0.0003	0.0002	0.0003	0.0003
Total fin	0.0000	-0.0002	-0.0005	-0.0006	-0.0007	-0.0006
Normal Force						
Fin1 (S)	-0.0005	0.0385	0.0795	0.1206	0.1598	0.1965
Fin2 (W)	-0.0082	0.0067	0.0247	0.0438	0.0628	0.0783
Fin3 (P)	0.0005	0.0395	0.0804	0.1214	0.1607	0.1976
Fin4 (L)	0.0082	0.0203	0.0214	0.0104	-0.0078	-0.0371
Total fin	0.0000	0.1049	0.2060	0.2962	0.3755	0.4353

S = starboard; W = windward; P = port; L = leeward.

Table E-4. Aerodynamic coefficients on grid fins, $\delta = 10^\circ$, Mach 3.0.

α	0	2	4	6	8	10
Axial Force						
Fin1 (S)	0.0838	0.0798	0.0834	0.0840	0.0821	0.0795
Fin2 (W)	0.0838	0.0900	0.0924	0.0942	0.0960	0.0999
Fin3 (P)	0.0838	0.0755	0.0839	0.0845	0.0813	0.0748
Fin4 (L)	0.0838	0.0713	0.0652	0.0636	0.0630	0.0622
Total fin	0.3351	0.3166	0.3249	0.3262	0.3224	0.3164
Side Force						
Fin1 (S)	0.0052	0.0097	0.0154	0.0192	0.0279	0.0409
Fin2 (W)	0.0079	0.0050	0.0038	0.0030	0.0022	-0.0001
Fin3 (P)	-0.0052	-0.0180	-0.0184	-0.0205	-0.0233	-0.0277
Fin4 (L)	-0.0079	-0.0136	-0.0173	-0.0048	0.0187	0.0380
Total fin	0.0000	-0.0169	-0.0165	-0.0031	0.0256	0.0511
Normal Force						
Fin1 (S)	0.0079	0.0437	0.0852	0.1253	0.1610	0.1920
Fin2 (W)	-0.0052	0.0084	0.0254	0.0437	0.0624	0.0781
Fin3 (P)	-0.0079	0.0301	0.0741	0.1174	0.1602	0.2017
Fin4 (L)	0.0052	0.0186	0.0252	0.0168	-0.0054	-0.0266
Total fin	0.0001	0.1008	0.2099	0.3033	0.3782	0.4452

S = starboard; W = windward; P = port; L = leeward.

Appendix F. Components of Aerodynamic Coefficients

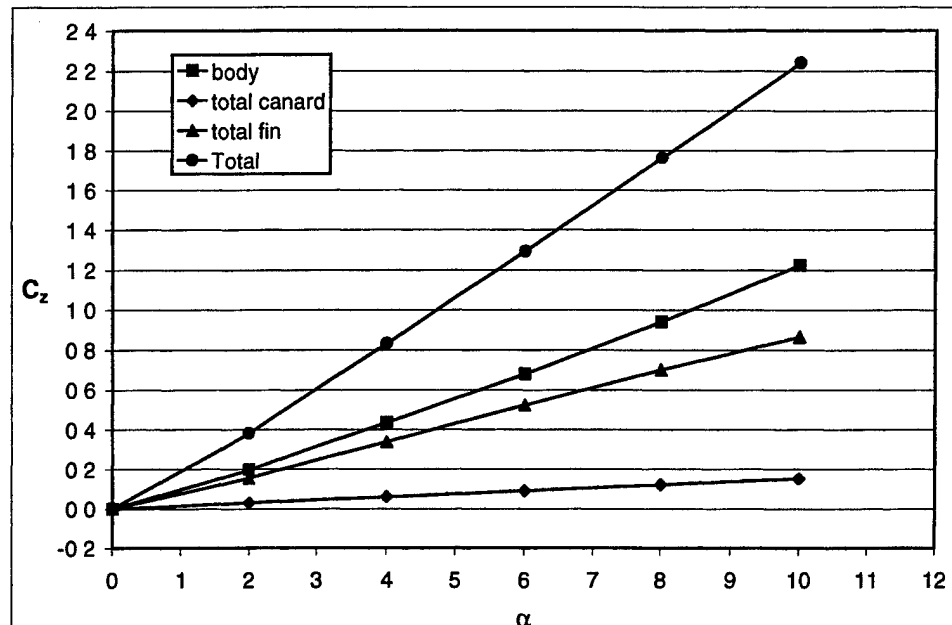


Figure F-1. Components of normal force for planar fin case, $\delta = 10^\circ$, Mach 1.5.

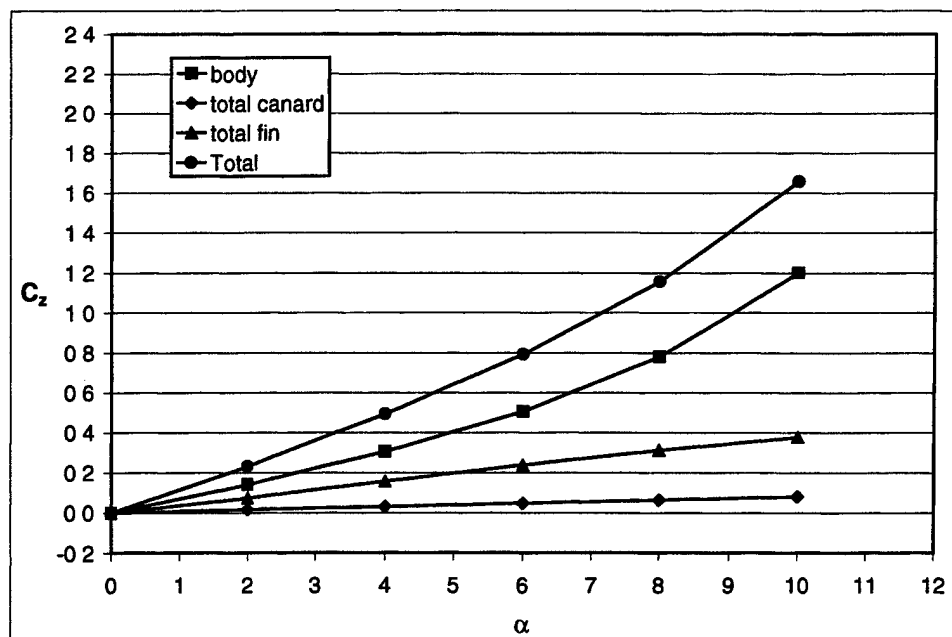


Figure F-2. Components of normal force for planar fin case, $\delta = 10^\circ$, Mach 3.0.

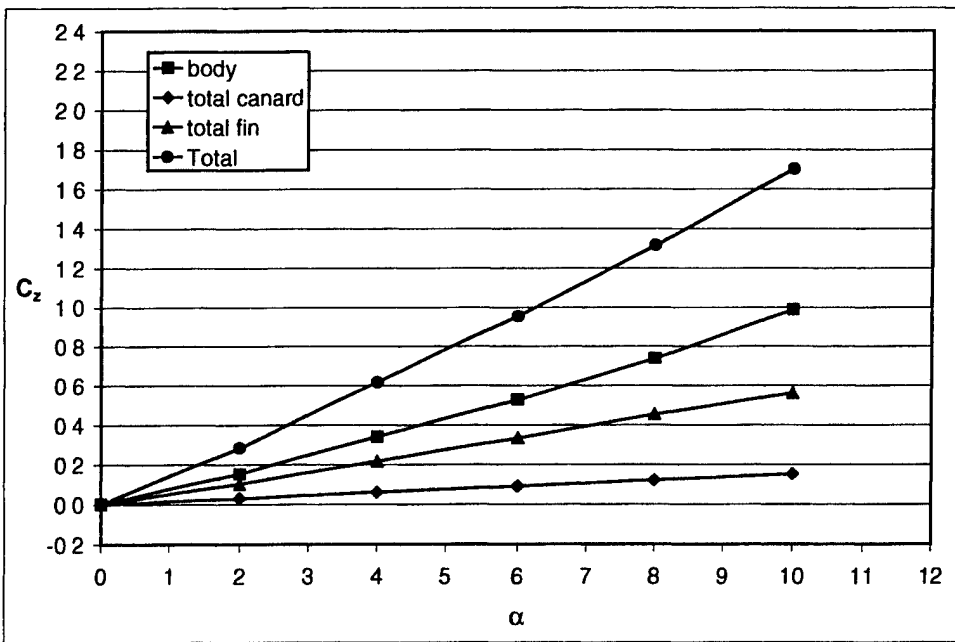


Figure F-3. Components of normal force for grid fin case, $\delta = 10^\circ$, Mach 1.5.

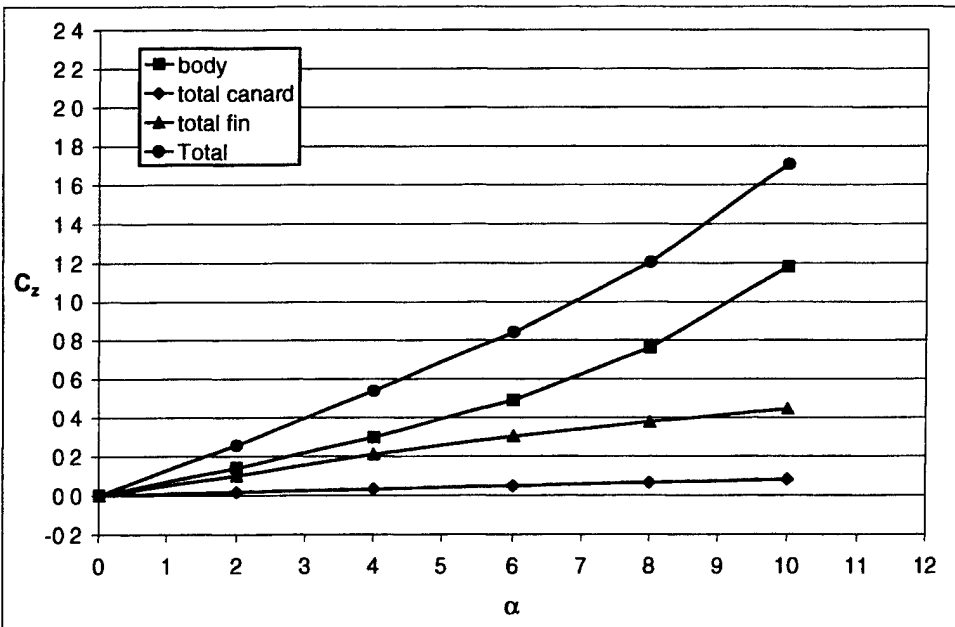


Figure F-4. Components of normal force for grid fin case, $\delta = 10^\circ$, Mach 3.0.

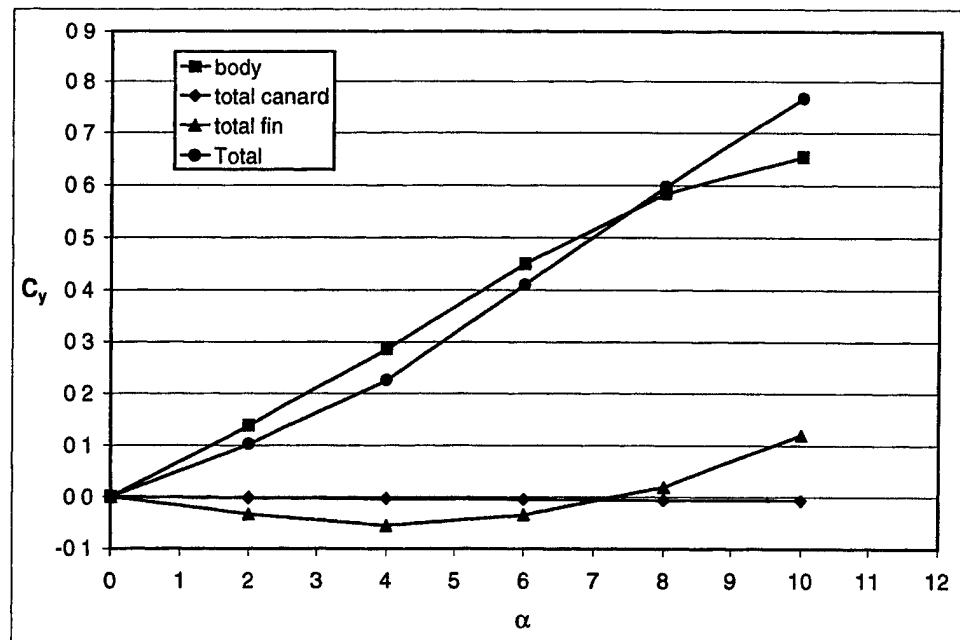


Figure F-5. Components of side force for planar fin case, $\delta = 10^\circ$, Mach 1.5.

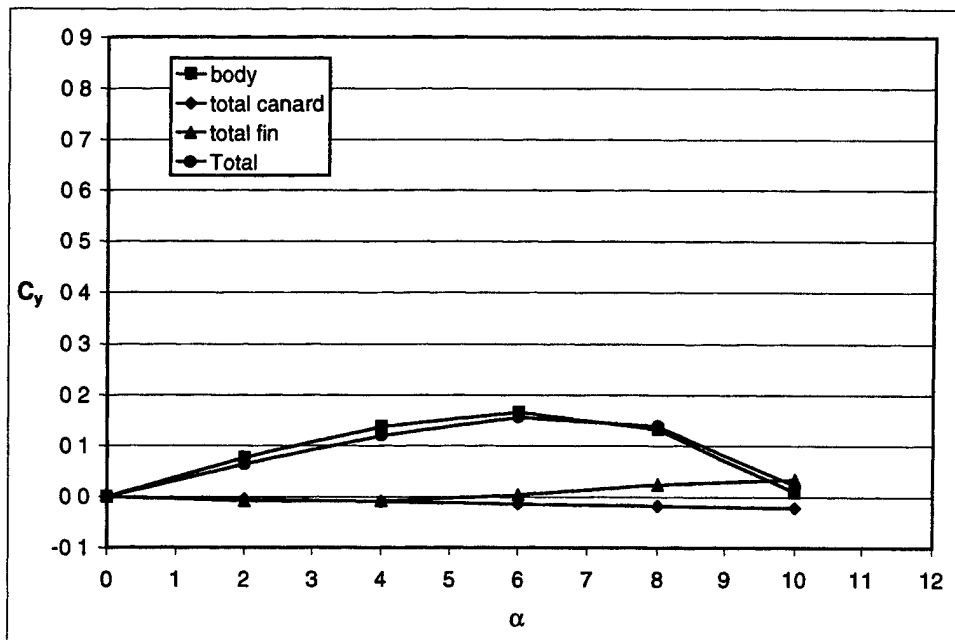


Figure F-6. Components of side force for planar fin case, $\delta = 10^\circ$, Mach 3.0.

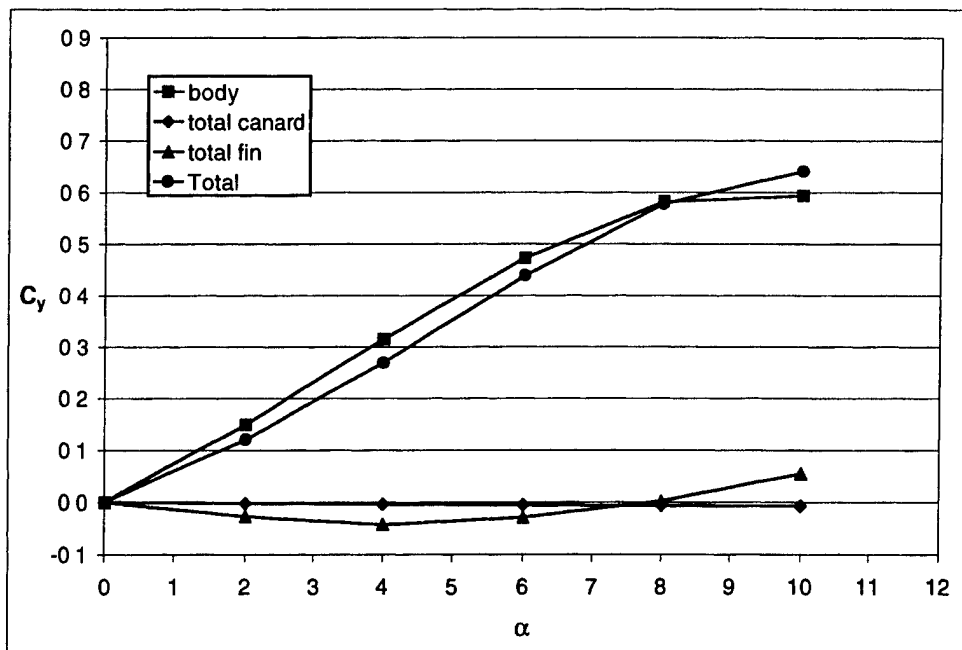


Figure F-7. Components of side force for grid fin case, $\delta = 10^\circ$, Mach 1.5.

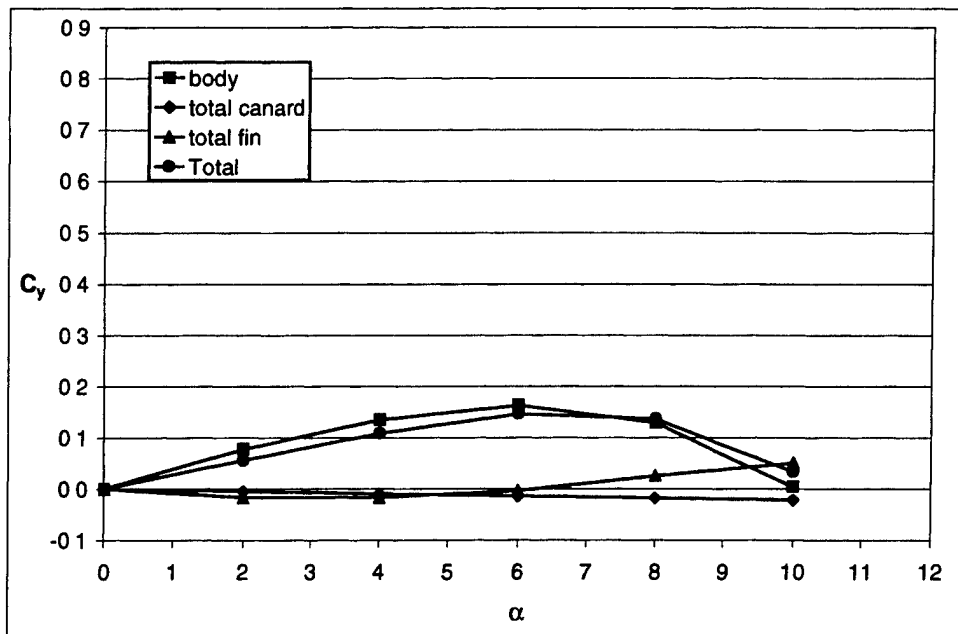


Figure F-8. Components of side force for grid fin case, $\delta = 10^\circ$, Mach 3.0.

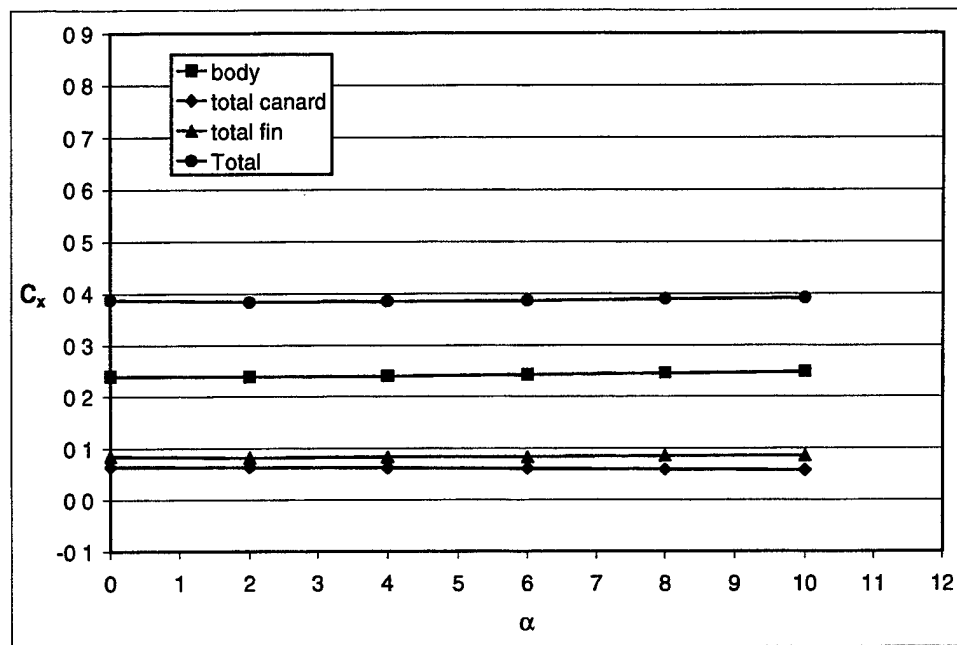


Figure F-9. Components of axial force for planar fin case, $\delta = 10^\circ$, Mach 1.5.

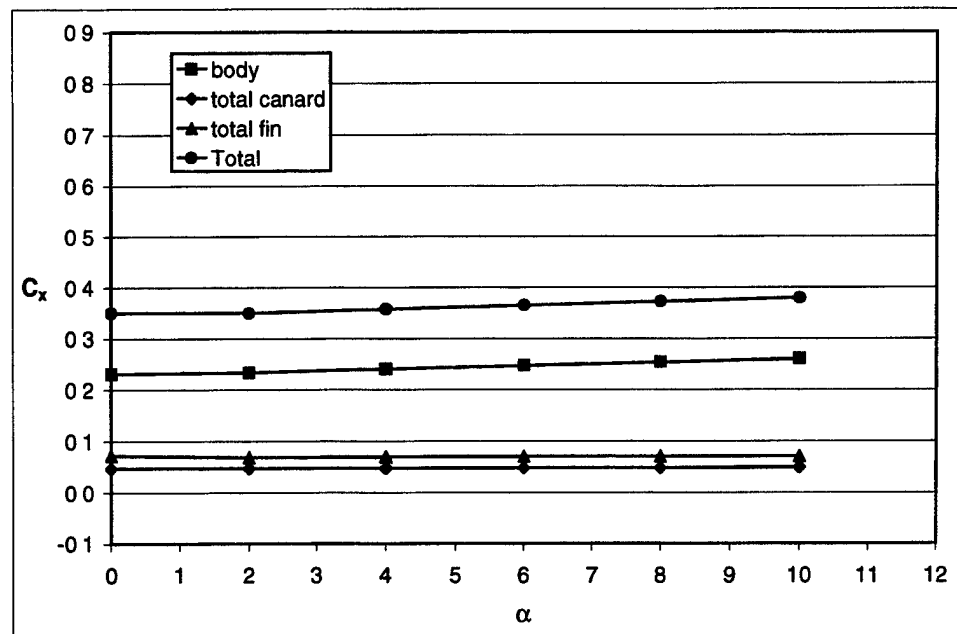


Figure F-10. Components of axial force for planar fin case, $\delta = 10^\circ$, Mach 3.0.

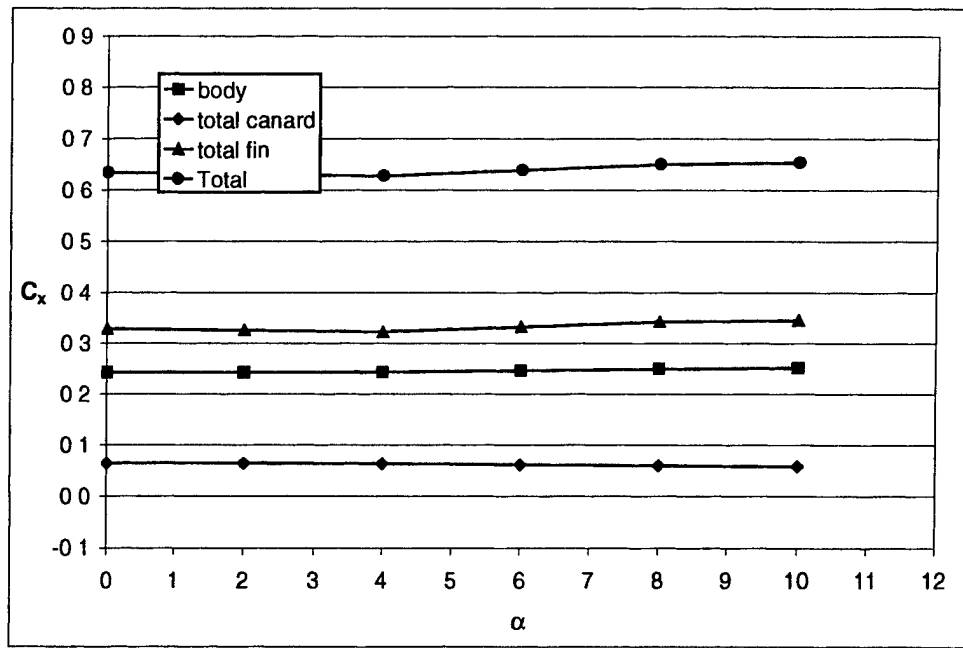


Figure F-11 Components of axial force for grid fin case, $\delta = 10^\circ$, Mach 1.5.

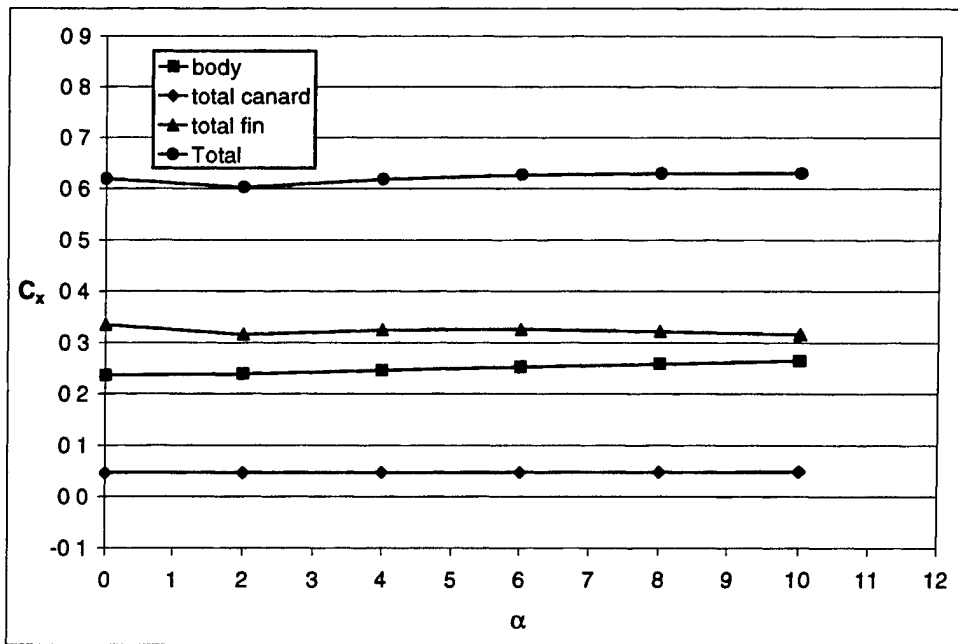


Figure F-12. Components of axial force for grid fin case, $\delta = 10^\circ$, Mach 3.0.

Table F-1. Components of aerodynamic coefficients, planar fin case, $\delta = 0^\circ$, Mach 1.5.

α	0	2	4	6	8	10
Axial Force						
Body	0.2332	0.2356	0.2401	0.2446	0.2491	0.2524
Total canard	0.0245	0.0246	0.0247	0.0246	0.0244	0.0241
Total fin	0.0826	0.0828	0.0844	0.0864	0.0878	0.0880
Total	0.3403	0.3429	0.3492	0.3556	0.3613	0.3644
Side Force						
Body	0.0000	-0.0001	-0.0002	-0.0003	-0.0005	-0.0006
Total canard	0.0000	0.0000	0.0000	0.0000	0.0000	0.0000
Total fin	0.0000	0.0000	0.0000	-0.0001	-0.0001	-0.0002
Total	0.0000	-0.0001	-0.0002	-0.0004	-0.0005	-0.0008
Normal Force						
Body	0.0000	0.1840	0.3926	0.6256	0.8788	1.1577
Total canard	0.0000	0.0350	0.0689	0.1013	0.1316	0.1598
Total fin	0.0000	0.1670	0.3433	0.5228	0.6972	0.8575
Total	0.0000	0.3860	0.8048	1.2497	1.7076	2.1750

Table F-2 Components of aerodynamic coefficients, planar fin case, $\delta = 10^\circ$, Mach 1.5

α	0	2	4	6	8	10
Axial Force						
Body	0.2392	0.2386	0.2395	0.2420	0.2452	0.2480
Total canard	0.0637	0.0634	0.0623	0.0608	0.0590	0.0574
Total fin	0.0846	0.0818	0.0833	0.0834	0.0857	0.0859
Total	0.3875	0.3837	0.3851	0.3862	0.3899	0.3914
Side Force						
Body	0.0000	0.1382	0.2855	0.4501	0.5842	0.6538
Total canard	0.0000	-0.0019	-0.0036	-0.0051	-0.0062	-0.0071
Total fin	0.0000	-0.0338	-0.0560	-0.0351	0.0191	0.1203
Total	0.0000	0.1025	0.2259	0.4099	0.5971	0.7670
Normal Force						
Body	0.0000	0.1967	0.4349	0.6794	0.9393	1.2234
Total canard	0.0000	0.0298	0.0599	0.0904	0.1215	0.1519
Total fin	0.0000	0.1550	0.3369	0.5230	0.7014	0.8641
Total	0.0000	0.3815	0.8316	1.2927	1.7622	2.2394

Table F-3. Components of aerodynamic coefficients, planar fin case, $\delta = 0^\circ$, Mach 3.0.

α	0	2	4	6	8	10
Axial Force						
Body	0.2287	0.2316	0.2388	0.2459	0.2530	0.2605
Total canard	0.0232	0.0231	0.0231	0.0232	0.0233	0.0234
Total fin	0.0697	0.0695	0.0699	0.0706	0.0706	0.0706
Total	0.3215	0.3243	0.3318	0.3396	0.3469	0.3545
Side Force						
Body	0.0000	0.0000	0.0000	0.0000	0.0000	-0.0001
Total canard	0.0000	0.0000	0.0000	0.0000	0.0000	0.0000
Total fin	0.0000	0.0000	0.0000	0.0000	0.0000	0.0000
Total	0.0000	0.0000	0.0000	0.0000	0.0000	-0.0001
Normal Force						
Body	0.0000	0.1380	0.2962	0.4979	0.7704	1.1857
Total canard	0.0000	0.0151	0.0303	0.0455	0.0612	0.0773
Total fin	0.0000	0.0769	0.1560	0.2368	0.3111	0.3771
Total	0.0000	0.2301	0.4825	0.7802	1.1427	1.6401

Table F-4. Components of aerodynamic coefficients, planar fin case, $\delta = 10^\circ$, Mach 3.0.

α	0	2	4	6	8	10
Axial Force						
Body	0.2309	0.2337	0.2404	0.2473	0.2538	0.2601
Total canard	0.0470	0.0471	0.0473	0.0477	0.0483	0.0489
Total fin	0.0720	0.0687	0.0696	0.0703	0.0704	0.0704
Total	0.3499	0.3495	0.3573	0.3654	0.3724	0.3794
Side Force						
Body	0.0000	0.0766	0.1377	0.1664	0.1322	0.0088
Total canard	0.0000	-0.0050	-0.0096	-0.0139	-0.0178	-0.0215
Total fin	0.0000	-0.0080	-0.0082	0.0038	0.0239	0.0342
Total	0.0000	0.0636	0.1200	0.1563	0.1383	0.0215
Normal Force						
Body	0.0000	0.1414	0.3054	0.5048	0.7798	1.1997
Total canard	0.0000	0.0160	0.0320	0.0481	0.0644	0.0807
Total fin	0.0000	0.0742	0.1561	0.2384	0.3119	0.3770
Total	0.0000	0.2316	0.4936	0.7912	1.1561	1.6574

Table F-5. Components of aerodynamic coefficients, grid fin case, $\delta = 0^\circ$, Mach 1.5

α	0	2	4	6	8	10
Axial Force						
Body	0.2372	0.2393	0.2440	0.2485	0.2525	0.2554
Total canard	0.0245	0.0246	0.0247	0.0246	0.0244	0.0241
Total fin	0.3217	0.3237	0.3347	0.3430	0.3498	0.3524
Total	0.5834	0.5875	0.6034	0.6161	0.6267	0.6319
Side Force						
Body	0.0000	-0.0012	-0.0018	-0.0009	-0.0012	-0.0017
Total canard	0.0000	0.0000	0.0000	0.0000	0.0000	0.0000
Total fin	-0.0001	0.0005	0.0012	0.0001	-0.0003	0.0004
Total	-0.0001	-0.0007	-0.0006	-0.0008	-0.0015	-0.0013
Normal Force						
Body	0.0000	0.1347	0.2896	0.4695	0.6773	0.9239
Total canard	0.0000	0.0350	0.0689	0.1013	0.1316	0.1598
Total fin	-0.0001	0.1097	0.2069	0.3061	0.4174	0.5218
Total	-0.0001	0.2794	0.5654	0.8769	1.2263	1.6055

Table F-6. Components of aerodynamic coefficients, grid fin case, $\delta = 10^\circ$, Mach 1.5.

α	0	2	4	6	8	10
Axial Force						
Body	0.2424	0.2422	0.2431	0.2458	0.2489	0.2513
Total canard	0.0637	0.0634	0.0623	0.0608	0.0590	0.0574
Total fin	0.3284	0.3253	0.3221	0.3322	0.3425	0.3455
Total	0.6345	0.6309	0.6275	0.6388	0.6504	0.6542
Side Force						
Body	0.0000	0.1497	0.3150	0.4728	0.5820	0.5937
Total canard	0.0000	-0.0019	-0.0036	-0.0051	-0.0062	-0.0071
Total fin	0.0001	-0.0267	-0.0422	-0.0288	0.0018	0.0547
Total	0.0001	0.1211	0.2692	0.4388	0.5775	0.6413
Normal Force						
Body	0.0000	0.1528	0.3406	0.5281	0.7390	0.9879
Total canard	0.0000	0.0298	0.0599	0.0904	0.1215	0.1519
Total fin	0.0002	0.1015	0.2171	0.3357	0.4550	0.5625
Total	0.0002	0.2841	0.6176	0.9542	1.3156	1.7023

Table F-7 Components of aerodynamic coefficients, grid fin case, $\delta = 0^\circ$, Mach 3.0.

α	0	2	4	6	8	10
Axial Force						
Body	0.2341	0.2371	0.2441	0.2514	0.2581	0.2647
Total canard	0.0232	0.0231	0.0231	0.0232	0.0233	0.0234
Total fin	0.3217	0.3228	0.3263	0.3269	0.3247	0.3183
Total	0.5789	0.5831	0.5936	0.6014	0.6060	0.6064
Side Force						
Body	0.0000	0.0004	0.0004	0.0005	0.0004	0.0000
Total canard	0.0000	0.0000	0.0000	0.0000	0.0000	0.0000
Total fin	0.0000	-0.0002	-0.0005	-0.0006	-0.0007	-0.0006
Total	0.0000	0.0002	-0.0001	-0.0001	-0.0003	-0.0006
Normal Force						
Body	0.0000	0.1356	0.2890	0.4846	0.7512	1.1702
Total canard	0.0000	0.0151	0.0303	0.0455	0.0612	0.0773
Total fin	0.0000	0.1049	0.2060	0.2962	0.3755	0.4353
Total	0.0000	0.2556	0.5253	0.8263	1.1880	1.6828

Table F-8. Components of aerodynamic coefficients, grid fin case, $\delta = 10^\circ$, Mach 3.0.

α	0	2	4	6	8	10
Axial Force						
Body	0.2367	0.2387	0.2458	0.2526	0.2586	0.2644
Total canard	0.0470	0.0471	0.0473	0.0477	0.0483	0.0489
Total fin	0.3351	0.3166	0.3249	0.3262	0.3224	0.3164
Total	0.6188	0.6024	0.6180	0.6266	0.6292	0.6297
Side Force						
Body	0.0000	0.0777	0.1348	0.1630	0.1288	0.0044
Total canard	0.0000	-0.0049	-0.0095	-0.0139	-0.0178	-0.0215
Total fin	0.0000	-0.0169	-0.0165	-0.0031	0.0256	0.0511
Total	0.0000	0.0559	0.1088	0.1460	0.1366	0.0339
Normal Force						
Body	0.0000	0.1392	0.2972	0.4901	0.7618	1.1798
Total canard	0.0000	0.0160	0.0321	0.0481	0.0644	0.0807
Total fin	0.0001	0.1008	0.2099	0.3033	0.3782	0.4452
Total	0.0001	0.2560	0.5391	0.8414	1.2044	1.7056

List of Abbreviations and Symbols

A	cell face area, m^2
cal.	caliber (1 caliber = D)
C_l	rolling moment coefficient
C_m	pitching moment coefficient
C_n	yawing moment coefficient
C_p	pressure coefficient
C_x	axial force coefficient
C_y	side force coefficient
C_z	normal force coefficient
D	missile base diameter, m
E	total energy, J
\mathbf{F}	inviscid flux vector
\mathbf{G}	viscous flux vector
\mathbf{H}	vector of source terms
$\mathbf{i}, \mathbf{j}, \mathbf{k}$	Cartesian unit vectors
M	Mach number
MRP	moment reference point
p	pressure, N/m^2
\mathbf{q}	heat flux vector
u, v, w	velocity components in x, y, z directions, m/s
V	cell volume, m^3
\mathbf{v}	velocity vector ($= ui + vj + wk$)
\mathbf{x}_{cp}	location of center of pressure
\mathbf{W}	vector of conservative variables
x, y, z	axial, horizontal, and vertical body axes
α	angle of attack, degree
δ	canard deflection angle, degree
ν	kinematic viscosity, m^2/s
ρ	density, kg/m^3
τ	viscous stress tensor

REPORT DOCUMENTATION PAGE			Form Approved OMB No. 0704-0188
<p>Public reporting burden for this collection of information is estimated to average 1 hour per response, including the time for reviewing instructions, searching existing data sources, gathering and maintaining the data needed, and completing and reviewing the collection of information. Send comments regarding this burden estimate or any other aspect of this collection of information, including suggestions for reducing this burden, to Washington Headquarters Services, Directorate for Information Operations and Reports, 1215 Jefferson Davis Highway, Suite 1204, Arlington, VA 22202-4302, and to the Office of Management and Budget, Paperwork Reduction Project(0704-0188), Washington, DC 20503.</p>			
1. AGENCY USE ONLY (Leave blank)	2. REPORT DATE	3. REPORT TYPE AND DATES COVERED	
	September 2002	Final, October 2001–June 2002	
4. TITLE AND SUBTITLE Numerical Investigation of Aerodynamics of Canard-Controlled Missile Using Planar and Grid Tail Fins, Part I: Supersonic Flow			5. FUNDING NUMBERS 1L1626I8AH80
6. AUTHOR(S) James DeSpirito, Milton E. Vaughn, Jr., * and W. David Washington *			
7. PERFORMING ORGANIZATION NAME(S) AND ADDRESS(ES) U.S. Army Research Laboratory ATTN: AMSRL-WM-BC Aberdeen Proving Ground, MD 21005-5066			8. PERFORMING ORGANIZATION REPORT NUMBER ARL-TR-2848
9. SPONSORING/MONITORING AGENCY NAMES(S) AND ADDRESS(ES)			10 SPONSORING/MONITORING AGENCY REPORT NUMBER
11. SUPPLEMENTARY NOTES * U.S. Army Aviation and Missile Command, ATTN: AMSAM-RD-SS-AT, Redstone Arsenal, AL 35898			
12a. DISTRIBUTION/AVAILABILITY STATEMENT Approved for public release; distribution is unlimited.		12b. DISTRIBUTION CODE	
13. ABSTRACT (Maximum 200 words) Viscous computational fluid dynamic simulations were used to predict the aerodynamic coefficients and flowfield around a generic canard-controlled missile configuration in supersonic flow. Computations were performed for Mach 1.5 and 3.0, at six angles of attack between 0° and 10°, with 0° and 10° canard deflection, and with planar and grid tail fins, for a total of 48 cases. Validation of the computed results was demonstrated by the very good agreement between the computed aerodynamic coefficients and those obtained from wind tunnel measurements. Visualizations of the flowfield showed that the canard trailing vortices and downwash produced a low-pressure region on the starboard side of the missile that in turn produced an adverse side force. The pressure differential on the leeward fin produced by the interaction with the canard trailing vortices is primarily responsible for the adverse roll effect observed when planar fins are used. Grid tail fins improved the roll effectiveness of the canards at low supersonic speed. No adverse rolling moment was observed with no canard deflection, or at the higher supersonic speed for either tail fin type due to the lower intensity of the canard trailing vortices in these cases. Flow visualizations from the simulations performed in this study help in the understanding of the flow physics and can lead to improved canard and tail fin designs for missiles and rockets.			
14. SUBJECT TERMS computational fluid dynamics, canard, lattice fins, grid fins, roll-reversal, missile aerodynamics			15 NUMBER OF PAGES 89
			16. PRICE CODE
17. SECURITY CLASSIFICATION OF REPORT UNCLASSIFIED	18. SECURITY CLASSIFICATION OF THIS PAGE UNCLASSIFIED	19. SECURITY CLASSIFICATION OF ABSTRACT UNCLASSIFIED	20. LIMITATION OF ABSTRACT UL